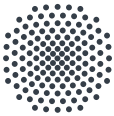

Universität Stuttgart

Ultrafast Laser Sources

Tunable, ultrafast laser sources for near- and mid-IR spectroscopy

Von der Fakultät Mathematik und Physik
der Universität Stuttgart zur Erlangung der Würde
eines Doktors der Naturwissenschaften (Dr. rer. nat.)
genehmigte Abhandlung

vorgelegt von

Florian Mörz
aus Schwäbisch Hall

Hauptberichter:	Prof. Dr. Harald Giessen
1. Mitberichter:	Prof. Dr. Peter Michler
Prüfungsvorsitzende:	Prof. Dr. Christian Holm

Tag der mündlichen Prüfung: 21. September 2020

4. Physikalisches Institut der Universität Stuttgart
2020

Florian Mörz: *Ultrafast Laser Sources – Tunable, ultrafast laser sources for near- and mid-IR spectroscopy*, 2020

ABSTRACT

Spectroscopy in the mid-infrared (MIR) spectral region allows for the exact chemical analysis in consequence of material-specific molecular vibrations. This enables a variety of important applications in both research and industry, such as in material science, life sciences, remote sensing, drug testing or quality control. However, the accessible sensitivity, wavelength range or bandwidth is often limited in many commercial systems in consequence of the applied MIR light sources. State-of-the-art light sources in commercial spectroscopy devices are thermal light sources, i.e. so-called Globars, and quantum cascade lasers (QCL). Globars are mainly used in so-called fourier transform infrared spectrometers, which allow for a high spectral resolution and fast measurements, compared to dispersive spectrometers. They work well for samples that allow for minimum µm spatial resolution and that exhibit vibrational signals on the few % level. However, applications that go beyond these limits require unacceptable long measurement times in consequence of the low brilliance of Globars, as well as their low beam quality and incoherent light. MIR lasers can overcome these limits due to an orders of magnitude higher brilliance, excellent beam quality and extremely low noise. Their application has the potential to extend the current limits of IR spectroscopy, which is urgently needed in many fields to allow for faster measurements, higher spatial resolution and the detection of weaker signals. But their utilization just set in and practical broadband laser systems need to be developed.
The goal of this thesis is the introduction of a MIR laser system for fourier-transform infrared spectroscopy. In contrast to quantum cascade lasers it is designed to exhibit a sufficient bandwidth that

avoids spectral sweeping and stitching to detect molecular vibrations. The system is based on parametric frequency conversion, which allows for a maximum wavelength tuning range from 1 to 20 µm in general and 1 to 8 µm for the prototype system presented in this thesis. The most significant advantages of our design are the small footprint, extremely low noise and the passive and intrinsic long-term stability. Thus, its implementation into commercial spectrometers remains at a very low complexity.
During this thesis, I introduce the laser setup and its significant advantages for FTIR spectroscopy. By conducting chemical mapping at ultralow sample concentrations and spatial resolution a so-far inaccessible application is presented. Next, the laser system is applied for the detection and characterization of protein structures at attomolar concentration and nm-scale, which is not accessible with a Globar at all. Using the laser setup this can be done within a few minutes. Finally, the current limits of the setup are discussed and its optimization to reach longer MIR wavelengths, as well as an alternative pump oscillator are presented.
This laser setup is not limited to FTIR spectroscopy but exhibits great potential for many other techniques. With few further advances it could be used in industry and medical research, where it could allow, for example, for the investigation of protein folding processes on a daily basis, which can be important to understand the mechanisms behind diseases such as Parkinsons, Alzheimers or Huntingtons disease.

ZUSAMMENFASSUNG

Spektroskopie im mittelinfraroten Spektralbereich ermöglicht genauste chemische Analysen infolge von materialspezifischen Molekülschwingungen. Dies findet Anwendung in zum Beispiel Arzneimittel- und Qualitätsprüfungen, in den Material- und Biowissenschaften oder in der Fernerkundung, d.h. die Detektion von chemischen Bestandteilen in der Luft oder der Atmosphäre. Jedoch sind kommerzielle Systeme oft in ihrer spektralen Bandbreite und dem abgedeckten Wellenlängenbereich und ihrer Sensitivität begrenzt. Dies ist häufig auf die verwendete MIR Lichtquelle zurückzuführen. Modernste kommerzielle Lichtquellen sind thermische Strahler, sogenannte Globars, und Quantenkaskadenlaser (QCL). Die spektral sehr breitbandigen Globars werden häufig in der Fourier-Transformations Infrarot FTIR Spektroskopie eingesetzt. Diese Spektrometer ermöglichen eine hohe spektrale Auflösung, schnelle Messungen und einen hohen optischen Durchsatz im Vergleich zu dispersiven Spektrometern und werden häufig für Materialanalysen in der Wissenschaft und der Industrie verwendet. Während gute Ergebnisse für Proben erreicht werden, die Absorptionsbanden von mehreren Prozent zeigen und eine räumliche Ausdehnung von einigen zehn Mikrometern aufweisen, sind Anwendungen, die über diese Grenzen hinausgehen, mit extrem langen Messzeiten und starkem Rauschen verbunden. Dies liegt vor allem an der niedrigen Brillanz, sowie der geringen Strahlqualität und Inkohärenz von thermischen Strahlern. Bei Verwendung von MIR-Laser in FTIRs können diese Grenzen überwunden werden, da Laser eine um Größenordnungen höhere Brillanz, eine exzellente Strahlqualität und sehr geringengs Rauschen aufweisen. Ihre Anwendung besitzt großes Potential die Grenzen der Spektroskopie zu erweitern. Dies ist erforderlich, um schwächere Signale und

kleinere Proben mit einer räumlichen Ausdehnung im nm-Bereich zu untersuchen. Ihre Anwendung in der FTIR-Spektroskopie steht jedoch erst am Anfang und einfacher nutzbare Systeme werden benötigt.
Das Ziel dieser Thesis ist die Eingliederung eines MIR Lasers in ein kommerzielles FTIR. Im Gegensatz zu Quantenkaskadenlaser ist dieses System auf eine ausreichende Bandbreite optimiert, wodurch das Abrastern von Vibrationsbanden und die anschließende Nachbearbeitung vermieden wird. Der vorgestellte Laser basiert auf der parametrischen Frequenzkonversion, mit welcher ein großer Spektralbereich abgedeckt werden kann. Der hier gezeigte Prototyp ermöglicht die Untersuchung von Vibrationsbanden zwischen 1250 und 7500 cm^{-1} (1.33-8 µm), wobei wir an anderer Stelle bereits Spektralbereiche von 500 bis 10 000 cm^{-1} vorgestellt haben. Die bedeutensten Vorteile dieses Lasers sind die sehr kleine Grundfläche, das geringe Rauschen und die passive, immanente Langzeitstabilität, die die Handhabung des Lasers und die Eingliederung in Messsysteme deutlich vereinfacht.
Die Anwendung und Vorteile des Lasersystems für die FTIR Spektroskopie werden im Laufe dieser Thesis anhand von verschiedenen Anwendungen vorgestellt. Mit der chemischen Abbildung einer 150×150 $µm^2$ großen Probe bei einer Auflösung von 10 µm wird eine bisher nicht realisierbare Anwendung gezeigt. Verschiedene Molekülschichten niedrigster Konzentration mit Absorptionen <1 % können eindeutig identifiziert werden. Darauffolgend werden Proteinstrukturen in-vitro erkannt. Trotz attomolarer Konzentration und nm-Größenordnung können Strukturen innerhalb von wenigen Minuten unterschieden werden. Abschließend werden die momentanen Grenzen des Systems und mögliche Optimierungen, um längere Wellenlängen bei höherer erzeugter Leistung zu erreichen, vorgestellt. Auch ein alternatives Pumplaserkonzept wird abschließend gezeigt.
Das vorgestellte Lasersystem ist nicht auf die FTIR Spektroskopie begrenzt. Es zeigt großes Potential für viele andere Techniken und kann mit wenigen Anpassungen in der Industrie oder Wissenschaft

eingesetzt werden. So könnte es beispielsweise die Untersuchung von Proteinfaltungen ermöglichen, die von besonderer Bedeutung zum Verständnis von neurodegenerativen Krankheiten sind und mit momentanen Spektroskopietechniken nur bei großen Konzentration möglich ist.

CONTENTS

1

INTRODUCTION

One of the most significant changes in the modern world is the growing digitization in our everyday life. Consumer products, industrial applications, or medical diagnostics, they all demand for faster and more efficient devices, smaller footprints, or more power to execute tasks simultaneously.
This development relies on extensive research to investigate new material properties and ongoing dynamic processes. In brief, sensitive and fast spectroscopy setups are required.
Already in the 1970s lasers have been applied to study molecular hyperfine structures. Roy J. Glauber, John L. Hall, and Theodor W. Hänsch paved the way of laser-based precision spectroscopy with their work from the 1960s to the 1990s. They got finally awarded with the *Nobel Prize in Physics* in 2005. Roy Glaubers research allows the explanation of quantum optical effects, the behavior of coherent or incoherent light, whereas the work of J. Hall and T. Hänsch led to the development of frequency comb spectroscopy using ultrastable mode-locked lasers [1–3].

This thesis focuses on the application of a laser source for Fourier-Transform Infrared (FTIR) spectroscopy. FTIR spectrometers provide an high sensitivity and SNR (Fellgett advantage [4]), a high optical throughput (Jacquinot advantage [5]), and a high spectral accuracy and resolution (Connes advantage [6]). Typically, this technique is used for material analysis and characterization based on IR absorption. Commercial systems are equipped with an incoherent, broadband thermal light source, a Globar, which covers

the IR-range up to 20 µm. However, it exhibits a low brilliance, which limits the measurement sensitivity to a few percent signal amplitude and spatial resolution to several tens of microns. In consequence of the weak absorption cross-section of molecular resonances, this results in high sample concentrations and eventually day-long integration times to reach a sufficient SNR.

Mid-IR lasers can overcome these limits, due to their high coherence, excellent beam quality, high power, and orders of magnitude higher brilliance. Several different laser systems have been applied for IR spectroscopy, including frequency combs [7, 8], broadband supercontinua [9], or commercially available quantum cascade laser systems (QCLs) [10, 11]. However, their complexity, limited wavelength range, or bandwidth hamper their widespread utilization. Here, a laser setup is applied for FTIR spectroscopy that allows for a broadband output of up to 125 cm^{-1} ($1/e^2$-width) and wavelength tuning from 1.3 to 20 µm (500 to 7519 cm^{-1}) at mW power. Excellent stability, low noise and a small footprint are achieved, by cascaded parametric frequency downconversion of a femtosecond solid-state oscillator, as we demonstrated in [12].
In this thesis, I present its implementation for FTIR spectroscopy, enabling significantly higher sensitivity, µm spatial resolution, and shorter measurement times compared to the commonly used Globars and synchrotrons. For the first time, chemical mapping using FTIR spectroscopy is presented, exhibiting the exact distribution of chemicals on a 150×150 $µm^2$ sample. A detection limit of 0.47 % relative absorption is reached with a single measurement.
By combining FTIR and surface-enhanced infrared absorption, measurements below the detection limit become feasible. Thus, the structure of polypeptides at attomolar concentrations is analyzed in-vitro. These results show an order of magnitude increased sensitivity, measurement speed and signal-to-noise ratio in a direct comparison to a Globar and a synchrotron source. Instead of hour-long integration, results are obtained in only a few minutes.

These results are obtained by further advances of the original design from [12], starting with research for a pump laser providing larger bandwidth, i.e. shorter pulses. At last, intense work on the final MIR conversion stage is presented, in order to achieve higher efficiency in the 10 to 20 µm region and intrinsically stabilize beam-pointing issues, resulting from wavelength tuning in the original system.

1.1 OUTLINE

This thesis investigates the application and optimization of a tunable, mid-IR parametric laser for IR spectroscopy. The presented approach is based on a femtosecond solid-state laser with 1 µm central wavelength, which pumps a cascaded frequency conversion scheme, as depicted in Fig. 1.1. This allows for a broad parametric tuning range, high power and brilliance, excellent stability and a compact footprint. The light source is characterized with respect to the well-established thermal and synchrotron light sources. The benefits and different applications are discussed and an outlook on future developments is given.

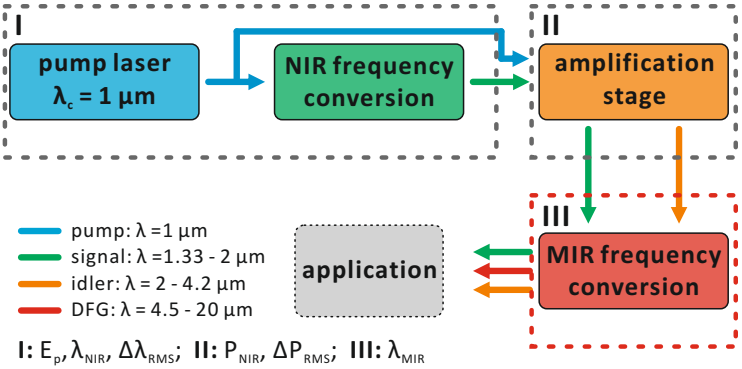

FIGURE 1.1. Scheme of a cascaded parametric mid-IR laser. It is divided into three parts. The first part (I) denotes the pump laser and the initial frequency conversion to the 1.3 to 2 µm range. Here, the achievable pulse energy E_p, NIR wavelength range λ_{NIR} and the wavelength stability $\Delta\lambda_{RMS}$ are pre-set. In the second part (II), the *signal beam* is amplified and the wavelength range is extended up to 4.2 µm by generating the *idler beam* due to energy conservation. The amplification stage is used to achieve high output power P_{NIR} and good power stability ΔP_{RMS}. In a DFG stage (III), the signal and idler beams are mixed and radiation between 4.5 and up to 20 µm is generated. Thus the overall setup can be wavelength tuned from 1.33 to 20 µm.

The thesis is structured into the following parts.

Chapter 3 gives an introduction to light and matter interactions, laser physics, parametric frequency conversion, and FTIR spectroscopy.

In **Chapter** 4 the implementation of a pump laser providing a larger bandwidth and shorter pulses compared to the laser used in [12] is presented. For IR spectroscopy a spectral bandwidth of

several tens of wavenumbers needs to be achieved. This can be accomplished by using a novel laser gain medium, Yb:CaF_2. Although CaF_2 has been discovered in the 1960s as a laser host material, it remained almost unnoticed until the discovery of the promising properties of Yb-doped CaF_2. Here, an oscillator is implemented with the goal to achieve several W output power at pulse durations on the order of 200 fs, which is ideal for subsequent parametric frequency conversion.

Chapter 5 presents further advances on the parametric frequency conversion setup and its application for micro-FTIR spectroscopy. For the first time, chemical mapping is conducted. A 150×150 µm² sample containing 100 nm-thin molecular layers is analyzed, giving a detailed distribution of the different molecules. A comparison to the standard FTIR light source is given.

In **Chapter 6** the laser is applied for the analysis of polypeptide structures. To detect samples on the nm-range, surface-enhanced infrared absorption is exploited, thus further extending the setup from the previous chapter. To quantify the laser performance, reference measurements are conducted using a Globar and synchrotron.

Chapter 7 advances on the mid-IR frequency conversion are discussed, based on the experiences of the previous chapters. A DFG setup is presented, which circumvents active beam-pointing stabilization during wavelength tuning and which allows for an increased efficiency in the 11 to 20 µm range compared to the standard setup.

Chapter 8 summarizes the presented results and gives an outlook on future work.

2

THEORETICAL BACKGROUND

2.1 LASER PHYSICS AND NONLINEAR FREQUENCY CONVERSION

In this chapter a brief introduction into light and matter interaction, laser physics and nonlinear optics is given. Hereby, I focus on optical parametric oscillation (OPO) amplification (OPA), and difference frequency generation (DFG). To a large extend, the discussion is based on [13]. At the end of this chapter a short discussion on Fourier-transform infrared (FTIR) spectroscopy and surface enhanced infrared absorption (SEIRA) is presented.

2.2 PRINCIPLES OF LIGHT AND MATTER INTERACTION

The interaction of light and matter can be discussed classically or quantum mechanically, accounting for the dual character of light. In the classical picture light is treated as electromagnetic waves. This allows for a description of basic effects, such as diffraction or propagation through media, based on Maxwell's equations. In contrast, absorption and emission are discussed from a quantum-mechanical view, accounting for the particle-like, i.e. photonic behavior. The propagation of electromagnetic waves in matter is described by the macroscopic Maxwell equations, given in Eq. (2.1).

Here, $\boldsymbol{D} = \varepsilon_0 \boldsymbol{E} + \boldsymbol{P}$ gives the electric displacement field. The macroscopic polarization $\boldsymbol{P}$ results from the induced electric dipole moments in the material. ε_0 is the vacuum permittivity. The magnetic field strength $\boldsymbol{H} = \frac{1}{\mu_0}\boldsymbol{B} - \boldsymbol{M}$ is the magnetic analogy to the electric displacement field. μ_0 is the vacuum permeability. In Eq. (2.1) ρ and $\boldsymbol{j}$ depict the charge and current densities, respectively.

$$\nabla \cdot \boldsymbol{D} = \rho \tag{2.1a}$$

$$\nabla \cdot \boldsymbol{B} = 0 \tag{2.1b}$$

$$\nabla \times \boldsymbol{E} = -\frac{\partial}{\partial t}\boldsymbol{B} \tag{2.1c}$$

$$\nabla \times \boldsymbol{H} = \boldsymbol{j} + \frac{\partial}{\partial t}\boldsymbol{D} \tag{2.1d}$$

The macroscopic polarization $\boldsymbol{P}$ arises from induced dipole moments in the medium, which are of linear and nonlinear nature. Therefore, it is expanded to

$$\boldsymbol{P} = \varepsilon_0 \left(\chi^{(1)} \boldsymbol{E} + \chi^{(2)} \boldsymbol{E}^2 + \chi^{(3)} \boldsymbol{E}^3 + \ldots \right) \tag{2.2a}$$

$$= \varepsilon_0 \chi^{(1)} \boldsymbol{E} + \boldsymbol{P}_{NL}. \tag{2.2b}$$

Intrinsic material characteristics are depicted by the susceptibility tensor $\chi^{(i)}$. The nonlinear terms are summarized in $\boldsymbol{P}_{NL}$.

To describe the propagation of electromagnetic waves in a dielectric, an uncharged ($\rho = 0$) and non-magnetic ($\boldsymbol{M} = 0$) medium is considered. Typically, magnetic moments can be neglected at optical frequencies in general. Maxwell's equations are decoupled

by means of the identity $\nabla \times \nabla \times \boldsymbol{E} = \nabla \left(\nabla \cdot \boldsymbol{E}\right) - \nabla^2 \boldsymbol{E}$ to derive the equation of motion for the electric and magnetic fields.

$$\nabla^2 \boldsymbol{E} - \frac{\partial^2}{\partial t^2} \left(\mu_0 \varepsilon_0 \boldsymbol{E} + \boldsymbol{P}\right) = 0 \tag{2.3a}$$

$$\nabla^2 \boldsymbol{B} - \frac{\partial^2}{\partial t^2} \left(\mu_0 \varepsilon_0 \boldsymbol{B}\right) + \mu_0 \frac{\partial}{\partial t} \left(\nabla \times \boldsymbol{P}\right) = 0 \tag{2.3b}$$

To get a basic insight into light and matter interactions, a linear response of the medium is assumed and the nonlinear source terms P_{NL} are neglected. The most simple solution of Eq. (2.3a) is given by *plane waves* with

$$\boldsymbol{E}\left(\boldsymbol{r}, t\right) = \boldsymbol{E}_0\left(\boldsymbol{r}, t\right) e^{i\left(\boldsymbol{k}\cdot\boldsymbol{r} - \omega t\right)}. \tag{2.4}$$

The wave vector $\boldsymbol{k}$ depicts the direction of propagation. It is related to the optical frequency $\nu = \frac{\omega}{2\pi}$ by $|k| = \frac{n\nu 2\pi}{c}$. In spectroscopy, it is usualy expressed as the wavenumber $\tilde{\nu} = \frac{k}{2\pi}$ in units of cm^{-1}. Plane waves are characterized by constant phases $\Phi = \boldsymbol{k} \cdot \boldsymbol{r} - \omega \cdot t$ in transverse planes perpendicular to the propagation direction. These planes are also known as wave fronts. They propagate through the medium at the *phase velocity*

$$v_{ph} = \frac{\omega}{k} = \frac{c}{n}. \tag{2.5}$$

The wave vector $\boldsymbol{k}$ is complex in general. This accounts for gain and attenuation of the propagating wave's amplitude. At the transition between two media, a fraction of the incoming light is reflected, whereas another fraction is transmitted. Assuming an angle of incidence (AOI) θ_1, the incident light is reflected at the identical angle at the media's interface. The angle θ_2 at which the transmitted light propagates is given by Eq. (2.6), which is known as *Snell's law*.

$$n_1 \cdot \sin\left(\theta_1\right) = n_2 \cdot \sin\left(\theta_2\right) \tag{2.6}$$

The phase of transmitted and reflected light, as well as the reflectivity and transmittance can be described well using plane waves. However, plane waves are not suited to describe e.g. laser light, which exhibits a rapidly decreasing field amplitude in the transverse plane. A solution that is able to describe laser beams is a Gaussian-shaped electric field amplitude $A(\boldsymbol{r})$, exhibiting cylindrical symmetry. The corresponding solution of Eq. (2.3a) is denoted as a *Gaussian beam*.
To give an intuitive insight, monochromatic light and propagation in the z direction is assumed. In the *paraxial* and *slowly varying envelope approximation* the equation of motion is solved by

$$E(\boldsymbol{r}, t) = A(\boldsymbol{r})\, e^{ikz} \cdot e^{-i\omega t} \tag{2.7a}$$

$$= A \frac{w_0}{w(z)} e^{-\frac{r^2}{w(z)^2}} e^{ik\left(z + \frac{r^2}{2R(z)}\right)} e^{-i\Phi(z)} e^{-i\omega t}. \tag{2.7b}$$

The resulting light beam exhibits a waist of $w(z)$, with the minimum beam waist $w_0 = w(z = 0)$. In contrast to plane waves, the wave fronts exhibit a radius of curvature $R(z)$. The *Gouy-Phase* $\Phi(z)$ describes a phase change around the focal region. This model also allows for focused and divergent beams, which is depicted by the half-angle of divergence Θ. A sketch of a Gaussian beam along the propagation axis is depicted in Fig. 2.1.

$$R(z) = z + \frac{z_R^2}{z} \tag{2.8a}$$

$$w(z)^2 = w_0^2 \left(1 + \frac{z^2}{z_R^2}\right) \tag{2.8b}$$

$$\Phi(z) = \arctan\left(\frac{z}{z_R}\right) \tag{2.8c}$$

$$\Theta = \frac{\lambda}{\pi n w_0} \tag{2.8d}$$

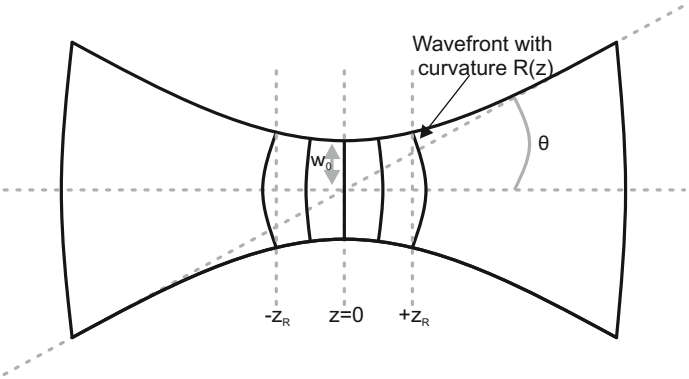

FIGURE 2.1. Sketch of Gaussian beam along the propagation axis z. The beam exhibits a minimum beam waist w_0 at $z = 0$. It is expanded to $\sqrt{2}w_0$, i.e. twice the beam area, at the Rayleigh range z_R. Here, the radius of curvature of the wavefronts is minimum, whereas it is maximum, i.e. infinite, at $z = 0$. The divergence is depicted by the half angle of divergence Θ.

The *Rayleigh Range* z_R depicts the distance at which the beam waist reaches $\sqrt{2}w_0$, i.e at which the beam area is doubled. Furthermore, the wave front curvature becomes maximum (i.e. minimum radius of curvature (ROC)) at $z = z_R$, whereas it is minimum, i.e. similar to plane waves, at $z = 0$. The distance from $-z_R$ to z_R is also known as the confocal parameter $b = 2|z_R|$.

$$b = 2|z_R| = 2\frac{\pi w_0^2 n}{M^2 \lambda} \tag{2.9}$$

Here, the parameter M^2 describes the beam quality of a real laser beam with respect to a perfect Gaussian beam ($M^2 = 1$). It depicts the ability to focus a beam to w_0. Solid-state lasers allow for a beam quality as good as 1.1.

Diffraction limit

In optical imaging devices, such as microscopes, the accessible spatial resolution d is ultimately limited at the *diffraction limit*

$$d = \frac{\lambda}{2n \sin(\Theta)} = \frac{\lambda}{2 \cdot NA}. \tag{2.10}$$

The numerical aperture (NA) describes the cone, i.e. acceptance angle, at which light can be collected. Modern microscope objectives reach NAs of 1.2 to 1.4. Eq. (2.10) depicts that the minimum spatial resolution that can be achieved is proportional to half the light wavelength. Please note that a lower beam quality $M^2 > 1$ impairs the accessible resolution. Chemical selective material resonances are located in the mid-infrared (MIR) spectral region. However, assuming a MIR laser beam at $\lambda = 7\,\mu m$, the diffraction limit is on the order of 3.5 µm. This impedes the imaging of samples, which require nm-spatial resolution, such as a single protein or molecule. For that reason techniques have been developed to measure at or overcome the diffraction limit, such as surface enhanced infrared absorption (SEIRA)-spectroscopy, scattering-type scanning near-field optical microscopy (s-SNOM) or stimulated emission depletion (STED)-microscopy, which has been awarded with the nobel prize in 2014.

2.3 LASER PHYSICS

In the 1960s significant developments have been achieved in the field of laser physics. In consequence of the high light intensity and excellent beam quality, lasers have paved the way for a variety of significant research since then and are indispensable in the modern world. A laser is based on a gain medium, which is incorporated into an oscillator. The gain medium is atomically excited and emits

radiation during the relaxation to the ground state. This process starts spontaneously but soon becomes stimulated as the radiated light oscillates inside the cavity, providing feedback for the light emission. The intracavity power increases until an equilibrium between gain and losses is achieved. A fraction of the oscillating light beam is coupled out for subsequent applications.

A required condition for lasing is *population inversion*, which means that the associated upper atomic energy level needs to be more populated than the lower energy state, into which the laser transition takes place. In general, one distinguishes three-level, four-level and quasi-three-level laser systems, indicating the associated energy structure. The quasi-three-level laser is typically closer to the experimental observations, as the energy structure might be more complex due to energetic sub-levels, or the associated states can be very close together such that thermal excitation becomes possible [14].
In a three-level laser population is pumped at pump rate W_p from the ground state $|1\rangle$ to a higher energy level $|3\rangle$. This level exhibits a very short lifetime τ_{32} (10^{-8} to 10^{-11} s [14]) and the population relaxes non-radiatively to the metastable energy level $|2\rangle$. Its lifetime (10^{-3} to 10^{-6} s) is denoted as the excited state lifetime τ_L. Due to $\tau_L \gg \tau_{32}$ the population density N_3 remains approximately zero. During the transition from $|2\rangle$ to $|1\rangle$ photons of energy $h\nu_L$ are emitted spontaneously. Due to $\nu_p > \nu_L$ light emission back into the pump beam is avoided. Nevertheless, a small quantum defect $\Delta E = E_p - E_L$ is desired for efficient lasing, but can also lead to re-emission into the pump light. A basic scheme is given in Fig. 2.2a). Assuming a total population density $N = N_1 + N_2$ minimum 50 % of the total population must be in $|2\rangle$ to achieve population inversion, which results in a high pump threshold.
In contrast, four-level lasers allow for a very low threshold, as population inversion is easily achieved. Similar to a three-level system, population is pumped to a state ($|4\rangle$) with a fast decay time, from which it relaxes to the upper laser level $|3\rangle$. Light is emitted during the transition $|3\rangle \mapsto |2\rangle$, whereby the energy state $|2\rangle$ also exhibits

a short lifetime, such that relaxation to the ground state takes place immediately. In general, one assumes $N_4 \approx 0$ and $N_2 \approx 0$. Thus, population inversion $N_3 > N_2$ is achieved efficiently.
During the relaxation process light is emitted spontaneously. By inserting the gain medium into a cavity the emitted light is collected and fed back to the gain medium, where it stimulates the emission process. Stimulated emission is a coherent process, i.e. the phase of the emitted light is equal to the phase of the stimulating light. As it is spatially limited to a certain (mode) volume an oscillating light beam is formed.

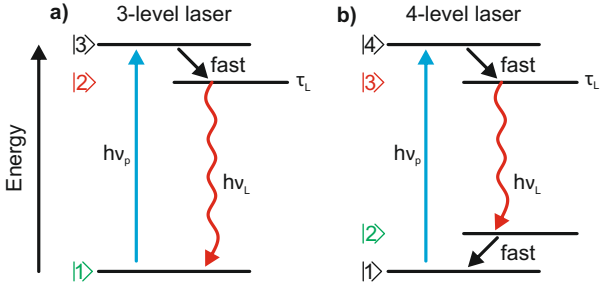

FIGURE 2.2. Energy level structure of a three-level (a) and four-level (b) laser. The upper laser level is marked in red, the lower level in green. Pump photons are absorbed and the gain medium is atomically excited. The upper laser level is reached after fast relaxation from an intermediate state, with a short lifetime (10^{-8} to 10^{-11} s [14]). The laser transition takes place either to the ground state (3-level laser) or to another intermediate state (4-level laser) exhibiting a fast decay time. The excited state lifetime τ_L is on the order of µs to ms. Emission sets in spontaneously but soon becomes stimulated in a laser cavity due to the feedback of the oscillating light. A required condition for lasing is that the upper laser level is higher populated than the lower level. In a 3-level laser this requires at least 50 % of the population to be in the upper state, as the lower state is the ground state. This results in a high laser threshold. In a 4-level laser this is achieved easily, as the lower energy state population is approximately 0 due to its short lifetime.

Laser operation

The following discussion is based on [15]. For simplicity, a two-mirror cavity is assumed, including a gain medium of length L and gain coefficient g. Intrinsic losses ($\propto L$) in the gain medium are denoted as α, whereas reflection losses at mirror 1, gain medium front and rear facets are depicted in δ. The loss factor $\Lambda = 2\alpha \cdot L + \delta$ summarizes these round trip losses. The second mirror is used to couple a fraction of the oscillating light out. Its reflection is denoted as R_{OC}.
The second required condition for lasing is the *cancellation of gain and losses per round trip*. This *threshold condition* is expressed as

$$2 \cdot g \cdot L = \Lambda - \ln R_{OC}. \tag{2.11}$$

As long as the round trip net gain is larger than unity (i.e. g exceeds the losses), the oscillating radiation is amplified and the intensity increases exponentially ($I \propto e^{g \cdot L}$) with every passage through the gain medium. However, this also increases the rate at which the stimulated light emission is driven and depletion of the upper laser level sets in. In consequence, the gain factor g is decreased until an equilibrium of gain and losses is reached. This is known as *gain saturation*. For the following discussion, I consider a four-level laser system. The gain resulting from a pump rate W_p above threshold, but without lasing (i.e. no feedback) is denoted as the single-pass gain g_0. It is

$$g_0 = \frac{\sigma_{em} \tau_L \eta}{h \nu_L V} \cdot P_p, \tag{2.12}$$

with the emission cross-section σ_{em}, the pumping efficiency η and the mode-volume V. The gain coefficient during lasing at intensity I is given by

$$g(I) = \frac{g_0}{1 + \frac{I}{I_s}}. \tag{2.13}$$

Gain saturation sets in at the saturation intensity I_s, which is given in Eq. (2.14) for a four-level laser.

$$I_s = \frac{h\nu_L}{\sigma_{em}\tau_L} \tag{2.14}$$

At the saturation intensity the round trip gain is reduced to $g_0/2$ and the output power becomes linearly dependent on the applied pump power P_p. The laser output power is expressed by

$$P_{out} = A\frac{1-R_{OC}}{1+R_{OC}} I_s \left(\frac{2g_0 L}{\Lambda - ln\left(R_{OC}\right)} - 1 \right) \tag{2.15a}$$

$$\approx \frac{T_{OC}}{T_{OC}+\Lambda} \cdot \eta \cdot \left(P_p - \frac{T_{OC}+\Lambda}{2} \frac{A \cdot h\nu_L}{\eta\sigma_{em}\tau_L} \right) \tag{2.15b}$$

$$= \frac{T_{OC}}{T_{OC}+\Lambda} \cdot \eta \cdot \left(P_p - P_{th} \right). \tag{2.15c}$$

In Eq. (2.15c) I introduced the threshold pump power P_{th} (depending on the effective mode-area A) and approximated R_{OC} by the outcoupling rate T_{OC} for $R_{OC} \approx 1$. I assumed $1 - R_{OC} \approx -ln\left(R_{OC}\right) \approx T_{OC}$ and $1 + R_{OC} \approx 2$. As the loss R_{OC} significantly affects the laser steady-state operation, the output power is optimized by adapting the outcoupling rate. Optimum power is achieved at

$$T_{opt} = \left(\sqrt{\frac{2g_0 L}{\Lambda}} - 1 \right) \Lambda. \tag{2.16}$$

Eq. (2.15b) depicts that the threshold pump power P_{th} is proportional to $\frac{1}{\sigma_{em}\tau_L}$. Therefore a gain medium with a large product of emission cross-section and excited state lifetime exhibits a low threshold.

Relaxation oscillations

Relaxation oscillations depict oscillations of the laser energy around its steady-state, which is reached after the decay time τ_R in consequence of damping. Relaxation oscillations occur in a transient state before the steady-state operation is reached. They occur as the upper laser level population initially exceeds the steady-state population. Thus, the intracavity laser intensity grows exponentially, until depletion of the upper laser level sets in. In consequence the upper level is depleted below the steady-state population, i.e. $g < \Lambda + R_{OC}$. Thus, the intracavity intensity is decreased and the population of the upper laser level starts to increase again. This process occurs in a damped manner until the steady-state is reached. In consequence, damped intensity oscillations are observed. In a real laser setup, small perturbations, such as mechanical vibrations, also induce relaxation oscillations during steady-state operation. However, they are typically negligible in soliton mode-locked solid-state lasers. For a four-level laser the oscillation frequency ν_r and decay time τ_r are given by [15]

$$\nu_r = \sqrt{\frac{I}{I_s \tau_L \tau_c}}, \tag{2.17a}$$

$$\tau_r = 2\tau_L \frac{I_s}{I}. \tag{2.17b}$$

In Eq. (2.17a) $\tau_c = \frac{T_{rep}}{\epsilon} = \frac{2L_{cav}/c}{R_{OC}+\Lambda}$ gives the photon lifetime in the resonator, i.e. the round-trip time (optical cavity length L_{cav}) divided by the fractional loss ϵ. ν_r is in the kHz-range for solid-state lasers with MHz pulse repetition rate.

LIGHT PULSES

In the previous section continuous light was assumed. Lasers that are operated in this regime are known as continuous wave (CW) lasers. In contrast, lasers can also emit intense pulses, providing significantly higher peak intensities. To achieve pulsed operation the phase of the longitudinal cavity modes is locked and, due to interference, pulses are formed. This is indicated in Fig. 2.3. Pulsed lasers allow for broad spectra, as multiple modes within the gain bandwidth are locked. The pulse duration and spectral bandwidth are directly connected, which is expressed by the time-bandwidth product (TBP) given in Eq. (2.18a). It is a measure for the spectral phase of the pulses and minimum if the phase is linear or constant over the spectral bandwidth. Pulses that satisfy this condition are known as Fourier-limited. They exhibit minimum pulse duration for a given bandwidth. Assuming a Gaussian-shaped pulse the Fourier-limited TBP is 0.44, for $sech^2$ pulses it is 0.315. Ideally, the TBP is close to its Fourier-limit, which allows for efficient nonlinear processes, but in consequence of dispersion or chirp it can differ significantly.

$$\tau_p \cdot \Delta\nu_L \geq \begin{cases} 0.44 & \text{for Gaussian-shaped pulses} \\ 0.315 & \text{for } sech^2\text{-shaped pulses} \end{cases} \tag{2.18a}$$

The lasers used in this thesis are continuously pumped with laser diodes, whereas the excited population is extracted only at certain time intervals, i.e. when the oscillating pulse passes the medium. As the saturation intensity depends on the pump rate and gain medium, gain saturation is identical in both pulsed and CW operation. Thus, the achieved average output power is similar as well.

Mode-locking can be achieved actively or passively. Here, I focus on two different passive techniques, known as *Q-switching* and

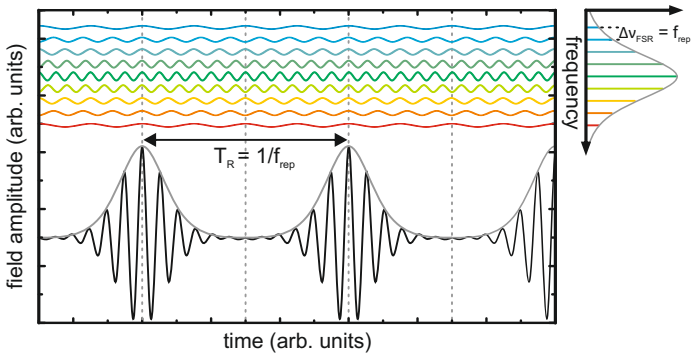

FIGURE 2.3. Instead of continuous laser operation (cw), pulsed operation can be achieved by locking the phases of the longitudinal cavity modes, which are separated by the free-spectral range $\Delta\nu = \frac{c}{2L} = f_{rep}$. For a stable phase relation pulses are formed in consequence of constructive and destructive interference. The temporal separation of the pulses is the cavity round-trip time $T_R = \frac{1}{f_{rep}}$. For soliton mode-locking the spectral pulse shape is given by a $sech^2$-intensity distribution.

soliton mode-locking. Both make use of a semiconductor saturable absorber mirror (SESAM) to achieve laser pulses. As depicted in Fig. 2.4, the mirror's reflectance depends on the incident pulse fluence (energy per area). Thus the cavity losses are modulated, which significantly affects the laser dynamics. Q-switching and soliton mode-locking are two different physical phenomena, which however might interfere as a large Q-switching tendency is frequently observed in soliton mode-locked lasers. In this case Q-switching is an unwanted effect that needs to be suppressed.

A SESAM is built of a Bragg mirror and a quantum well absorber on top, all made of a semiconductor material[16]. Incident photons are absorbed and excite electrons from the valence to the conduction band via *interband transitions* in the quantum well absorber, as depicted in the inset of Fig. 2.4. At high incident intensity, i.e. large number of incident photons, the absorption is saturated (*Pauli blocking*), as electrons accumulate in the conduction band and the valence band is depleted. Thus, the reflectivity of the mirror is

increased, as absorption is decreased. After the incident light pulse, relaxation occurs initially via intraband thermal relaxation (fast) and later via recombination from the conduction to the valence band (slow, several pico- to nanoseconds)[16]. The relaxation time is given by τ_R. Important design parameters are the modulation depth ΔR, which describes the reflectivity change from the unsaturated to the saturated state, the required saturation energy $E_{s,a}$, and the excitation wavelength. In solid-state lasers, the SESAM is typically operated in a highly saturated regime, which means it is operated more than three times above $E_{s,a}$, i.e. $S = \frac{E_p}{E_{s,a}} > 3$[17].

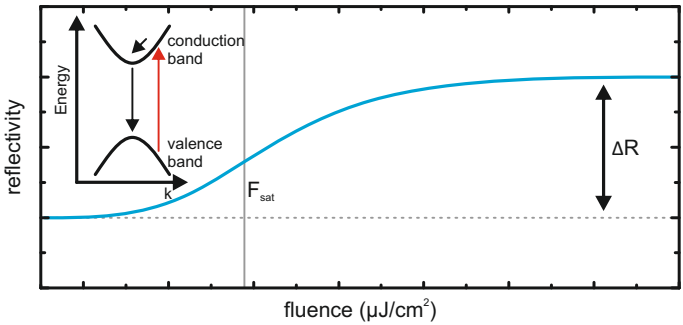

FIGURE 2.4. SESAM reflectivity as a function of the incident laser fluence (energy per area). For increasing fluence (i.e. number of incident photons) the reflectivity increases until saturation sets in if the incident pulse energy exceeds the saturation fluence. This is due to the significant excitation of electrons from the valence to the conduction band of the semiconductor material, as indicated in the inset. The maximum reflectivity change ΔR is reached, if the valence band is depleted and the conduction band occupied (Pauli blocking).

Soliton mode-locking

Soliton mode-locking allows for stable femtosecond laser pulses at a high pulse repetition rate f_{rep}. The pulse repetition rate is inversely proportional to the optical cavity length. The term *soliton* mode-locking refers to the generated soliton-like pulses, which result from a balance between negative group delay dispersion (GDD) and self-phase modulation (SPM). Pulse shaping is solely due to soliton formation, which finally locks the longitudinal cavity modes. However, a saturable absorber mirror (SAM) is used to stabilize the laser pulses against the growth of background radiation/noise. In contrast to kerr-lens mode-locking (KLM) a SESAM with a recovery time τ_R much longer than the finally achieved pulse duration τ_p is used. This is also known as the utilization of a slow SAM.
In case of a negative GDD per round-trip the equation of motion of a light pulse in a laser cavity is solved by a soliton solution ($sech^2$-pulse shape). However, perturbations lead to growing background radiation (continuum), which destabilizes the soliton-like pulse if it is not suppressed. In consequence of the response of a slow SAM, as shown in Fig. 2.5, the soliton pulse and the background radiation are shifted in time with every SAM passage [18]. After several round trips the soliton propagates behind the noise. Thus, the leading background radiation is absorbed by the yet unsaturated SAM, whereas the soliton's pulse energy saturates the mirror and experiences low losses.

A general expression for the duration of soliton-like pulses is given by [17]

$$\tau_p \approx 1.76 \cdot \frac{2|D_2|}{|\gamma_{SPM}|E_p}, \tag{2.19}$$

with D_2 being the GDD per round-trip, $\gamma_{SPM} = \frac{4n_2L}{\lambda_c w^2}$ the SPM coefficient, n_2 the nonlinear refractive index, L the crystal length, and w depicts the beam waist. From Eq. (2.19) it becomes clear that a high pulse energy and low dispersion allow for shorter pulses, being

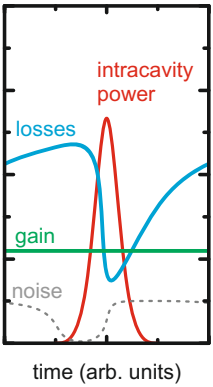

FIGURE 2.5. Using soliton mode-locking, pulse shaping is solely due to the formation of solitons but it is stabilized by a SESAM with a relaxation time exceeding the pulse duration. To soliton pulse is accompanied by a noise background, which significantly destabilizes the soliton. However, due to the energy dependent SAM reflectivity, the background noise and soliton are temporally shifted with every SAM passage, and the leading background noise is absorbed at the unsaturated mirror, thus stabilizing the soliton pulse. This mechanism is explained by the slow response ($\tau_R > \tau_p$) of the absorber. It is fully saturated at the soliton peak and exhibits low losses for some time afterwards, i.e. the leading pulse edge experiences higher losses than the trailing edge. Effectively, the pulse maximum is temporally shifted. Figure based on [18].

limited by the balance with SPM. The minimum pulse duration that can be achieved is given by [17]

$$\tau_{p,min} \approx 0.2 \cdot \left(\frac{1}{\Delta\nu_g}\right)^{3/4} \cdot \left(\frac{\tau_R}{\Delta R}\right)^{1/4} \cdot \frac{g^{3/8}}{\Phi_0^{1/8}}. \tag{2.20}$$

τ_p significantly depends on the gain bandwidth $\Delta\nu_g$ of the laser medium and SESAM characteristics. Φ_0 denotes the soliton phase-shift. The pulse energy and peak power are depicted by

$$E_p = \frac{P_{avg}}{f_{rep}}, \tag{2.21a}$$

$$P_{peak} \approx 0.88 \cdot \frac{E_p}{\tau_p}. \tag{2.21b}$$

Q-switching

Q-switched lasers exhibit intense bunches of pulses. It is based on tailoring the cavity losses with either an active device, such as an acousto-optic modulator (AOM) or a passive element, such as a SAM. Thus, *active* and *passive* Q-switching needs to be distinguished. In this thesis passive Q-switching instabilities are observed.

Passive Q-switching is induced by undamped or weakly damped relaxation oscillations, which cause a significant modulation of the intracavity energy [19]. In consequence of the energy dependent SAM reflectance this translates to intense bunches of (mode-locked) light pulses [20] at kHz repetition rate. Stable Q-switching is achieved if the intracavity intensity remains high enough to maintain stimulated emission between the intense bunches. Experimentally, stable passive Q-switching was achieved with the invention of SESAMs [21–23]. In contrast, if the intracavity losses become too high and stimulated emission ceases between the bunches, lasing restarts from spontaneous emission with each new bunch. Thus no stable steady-state is achieved, leading to significant instabilities in repetition rate and pulse energy. This is also know as *Q-switching instabilities*.

Q-switching is an unwanted but frequently observed effect in soliton mode-locked lasers. It becomes pronounced if the gain medium

exhibits low absorption or emission cross-sections, which, according to Eq. (2.14), define when gain saturation sets in. To avoid Q-switching (instabilities) the intracavity pulse energy needs to exceed a critical value, given by the saturation energies of the gain medium and SAM $E_{s,g}$, $E_{s,a}$ respectively, and the SAM modulation depth ΔR. A basic expression, which is valid for $\tau_p \geq$ ps is given by [20]

$$E_p^2 > E_{s,g} \cdot E_{s,a} \cdot \Delta R. \tag{2.22}$$

For a soliton mode-locked laser with femtosecond pulse duration Eq. (2.22) is refined to Eq. (2.23a) by introducing an interplay between soliton effects and gain filtering, which effectively reduces the required pulse energy [20].

$$E_{s,g} \cdot g \cdot K^2 \cdot E_p^3 + E_p^2 > E_{s,g} \cdot E_{s,a} \cdot \Delta R \quad \text{, with} \tag{2.23a}$$

$$K = \frac{4\pi \cdot n_2 \cdot 2 \cdot L}{D_2 \cdot A_{eff,g} \cdot \lambda_c \cdot \Delta\nu_g} \cdot \frac{0.315}{1.76}. \tag{2.23b}$$

In Eq. (2.23b) n_2 is the nonlinear refractive index of the gain medium, L is the gain medium length, D_2 depicts the GDD per round-trip, λ_c is the laser center wavelength and $\Delta\nu_g$ is the gain bandwidth (FWHM). Due to $E_{s,g} \propto I_s \propto \frac{1}{\sigma_{em}}$, Eq. (2.22) and Eq. (2.23a) underline that a low emission cross-section leads to a large critical energy and stable mode-locking is difficult to achieve with a conventional solid-state laser design. However, it can be achieved by passing the gain medium m-times per roundtrip, as the saturation energy $E_{s,g}$ is proportional to $\frac{1}{m}$. This is used in thin-disk lasers.

Pulse propagation

The velocity of the pulses' wave fronts (planes of equal phase) is given by the *phase velocity* depicted in Eq. (2.5). However, this is in general not identical to the propagation velocity of the laser pulse,

as the phase fronts of the pulses' individual frequency components might travel at different phase velocities due to chromatic dispersion. Therefore the *group velocity* is introduced, which depicts the propagation velocity of the pulse envelope. It is

$$v_g\left(\omega_0\right) = \left(\frac{d\omega}{dk}\right)_{\omega=\omega_0} = \frac{c}{n + \omega\frac{dn}{d\omega}} = \frac{c}{n_g\left(\omega\right)}, \tag{2.24}$$

with the angular central frequency $\omega_0 = 2\pi\frac{c}{\lambda_0}$. A synonymously utilized parameter for the group velocity is the *group index* n_g. If the pulse propagates through a dispersive medium, the different phase velocities of the individual frequency components lead to a temporal stretching of the pulse, i.e. after some time a spatial separation of the frequency components. This is expressed by the group velocity dispersion (GVD) given in Eq. (2.25).

$$GVD = \left(\frac{d^2k}{d\omega^2}\right)_{\omega_0} = \frac{d}{d\omega}\left(\frac{1}{v_g}\right)_{\omega_0} = \left(-\frac{1}{v_g^2}\cdot\frac{\partial v_g}{\partial\omega}\right)_{\omega_0} \tag{2.25}$$

The GVD is given in units of $\frac{\mathrm{fs}^2}{\mathrm{mm}}$, describing the accumulated temporal stretching per unit length. It is expressed as a function of wavelength via the dispersion parameter D.

$$D\left(\lambda\right) = \frac{d}{d\lambda}\frac{1}{v_g} = -\frac{2\pi c}{\lambda^2}\cdot\frac{d^2k}{d\omega^2} = -\frac{2\pi c}{\lambda^2}\cdot GVD \tag{2.26}$$

This parameter is given in units of $\frac{\mathrm{ps}}{\mathrm{nm}\cdot\mathrm{km}}$, describing the accumulated temporal stretching in picoseconds per nanometer wavelength change and kilometer propagation distance. It is typically used to depict the dispersion in optical fibers. Depending on the sign of the dispersion parameter, i.e. GVD, pulses can experience temporal stretching or compression. One refers to *normal* or *positive dispersion*, if v_g decreases for increasing optical frequency, i.e. positive GVD, whereas the opposite is known as *anomalous* or *negative dispersion*. The wavelength of zero GVD, i.e. at which the dispersion changes sign, is known as the *zero-dispersion wavelength*.

After propagation over a distance z the accumulated dispersion is expressed by the GDD, given in units of fs². The GDD is also denoted as the second-order dispersion. It is

$$D_2\left(\omega_0, z\right) = GVD \cdot z. \tag{2.27}$$

2.4 NONLINEAR OPTICS

So far, the higher-order terms in Eq. (2.2a) have been neglected. However, the nonlinear polarization can act as a source for new electric field components at different frequencies. The following discussion is based on [13] to a large extent. In this thesis, I focus on second-order effects, such as optical parametric frequency conversion. Therefore, the nonlinear polarization is given by

$$P_{NL} = \varepsilon_0 \chi^{(2)} \boldsymbol{E}^2. \tag{2.28}$$

In analogy to Eq. (2.3a), the nonlinear wave equation can be calculated to describe the nonlinear interaction of light and matter. With the speed of light $c = \left(\mu_0 \varepsilon_0\right)^{-1/2}$ and the refractive index $n\left(\omega\right) = \sqrt{\chi^{(1)}\left(\omega\right) + 1}$ it is

$$\nabla^2 = \frac{n^2}{c^2}\frac{\partial^2}{\partial t^2}\boldsymbol{E} + \frac{1}{\varepsilon_0 c^2}\frac{\partial^2}{\partial t^2}\boldsymbol{P}_{NL}. \tag{2.29}$$

For an electric field $E\left(t, \omega\right) = E_0 \cdot e^{-i\omega t} + c.c.$, the nonlinear polarization can be written as

$$P\left(\omega, t\right) = \varepsilon_0 \chi^{(2)} \cdot \left(E^2 e^{-i2\omega t} + \left(E^*\right)^2 e^{i2\omega t} + EE^*\right). \tag{2.30}$$

From this equation, it can be seen that the solution of the nonlinear wave equation contains an additional component at frequency 2ω and a constant EE^*. These processes are known as second harmonic

generation (SHG) and *optical rectification*.
By applying an electric field $E\left(\omega_1, \omega_2, t\right) = E_1 e^{-i\omega_1 t} + E_2 e^{-i\omega_2 t} + c.c.$ containing two different frequencies ω_1, ω_2 additional field components at frequencies $2\omega_1$, $2\omega_2$, $\omega_1 + \omega_2$ and $\omega_1 - \omega_2$ occur. The last two terms are known as sum frequency generation (SFG) and difference frequency generation (DFG).
The physical origin of these frequency components is explained by phase-matched collective oscillations of atomic dipoles $p_n\left(\omega_i, t\right)$ in response to the exciting electromagnetic field. The nonlinear response is assumed to result from the restoring force, exerted on the displaced electrons. This behavior is described by the *classical anharmonic oscillator model*. Depending on the phases of the individual dipoles, one effect (DFG, SFG,...) is favored and the radiated electromagnetic fields of each dipole add constructively, leading to a light beam in forward direction. The collective phases depend on the phases of the incident fields [13].
The nonlinear response takes place without transferring energy to the medium and both energy and momentum are conserved. Such processes are depicted as *parametric frequency conversion*.

Phase-matching

In order to achieve efficient frequency conversion the phase-matching condition $\Delta k = k_p - k_s - k_i = 0$ needs to be satisfied. It can be rewritten as

$$n_p \omega_p = n_s \omega_s + n_i \omega_i, \tag{2.31}$$

which basically denotes momentum conservation. In consequence of dispersion it is $n_p\left(\omega_p\right) \neq n_s\left(\omega_s\right) \neq n_i\left(\omega_i\right)$, thus making energy momentum conservation difficult to achieve simultaneously. However, by using birefringent crystals and differently polarized incident frequencies the interacting waves can be phase-matched. Assuming the typical case of a negative uniaxial crystal, the crystal

is set up at a specific angle θ, such that the refractive index of the extraordinary wave is adapted such that it is $n_o > n_e(\theta) > n_e$. The refractive index, or the phase-matching angle, is calculated according to

$$\frac{1}{n_e(\theta)^2} = \frac{\sin^2(\theta)}{n_e^2} + \frac{\cos^2(\theta)}{n_o^2}, \tag{2.32}$$

such that Eq. (2.31) is satisfied. Note that the polar angle θ is defined in an internal, crystallographic frame, but translates to the AOI. In general, the azimuthal angle ϕ needs to be correct as well, but is not directly related to momentum conservation. It corresponds to the crystal orientation *in* the plane of incidence. Phase-matching can be achieved for two different configurations, known as *Type-I* and *Type-II* phase-matching. They are distinguished by the polarization of the generated wave at the shortest frequency. A summary is given in Table 2.1[13].

	Positive uniaxial $(n_e > n_o)$	Negative uniaxial $(n_e < n_o)$
Type-I	$n_p^o\omega_p = n_s^e\omega_s + n_i^e\omega_i$	$n_p^e\omega_p = n_s^o\omega_s + n_i^o\omega_i$
Type-II	$n_p^o\omega_p = n_s^e\omega_s + n_i^o\omega_i$	$n_p^e\omega_p = n_s^o\omega_s + n_i^e\omega_i$

TABLE 2.1. Polarization of the interacting waves for Type-I and Type-II phase-matching. Table from [13].

Different terms are commonly used in literature to desrcibe this phase-matching technique,known as *critical*, *birefringent* or *angular phase-matching*. Critical phase-matching is usually applied for the generation of mid-IR light, commonly denoted as DFG. Frequency tuning involves the exact adaption of the crystal angle and significant angle tuning of several ten degrees (AOI) is required to achieve a broad tuning range. This goes along with several issues, such as Fresnel losses at the crystal facets in consequence

of high AOIs, or varying beam-pointing during frequency tuning, which impedes beam-pointing sensitive applications [24]. Furthermore, the effective nonlinearity results from a summation of the contributing tensor elements with respect phase-matching angle, polarization and azimuthal angle Φ. For $AgGaSe_2$ - silver gallium diselenide (AGSe) the effective nonlinearity with respect to the polarization of the interacting beams is [25]

$$d_{ooe} = d_{36} \sin(\theta) \sin(2\Phi) \qquad \text{Type-I pm,} \tag{2.33a}$$

$$d_{eoe} = d_{36} \sin(2\theta) \cos(2\Phi) \qquad \text{Type-II pm.} \tag{2.33b}$$

Due to this superposition the effective nonlinearity is smaller than the optimum value exhibited by the nonlinear medium.
Another limiting issue is the spatial separation of the interacting waves after some propagation length due to their polarization along different crystal axes. This might reduce the conversion efficiency significantly, as the effective interaction length might be extremely short. This effect, known as *spatial walk-off*, is expressed by the walk-off angle ρ, which is given in units of mrad and thus allows to calculate the effective interaction length ΔL. It is [25]

$$\rho = \pm \arctan\left(\left(\frac{n_o}{n_e}\right)^2 \tan(\theta)\right) \mp \theta, \tag{2.34}$$

where a negative uniaxial crystal is depicted by the upper sign, a positive uniaxial crystal by the lower sign.
Spatial walk-off also affects the angular acceptance, i.e. phase-matching bandwidth, which is defined as the full width at half maximum (FWHM) of the phase-matching angle θ over which significant gain ($G \geq \frac{G_{max}}{2}$) is achieved. For DFG it is

$$\Delta\theta = 1.772 \frac{\pi}{L} \left(\frac{\partial \Delta k}{\partial \theta}\right)^{-1}_{\theta=\theta_{PM}}. \tag{2.35}$$

The angular acceptance bandwidth is inversely proportional to the spatial walk-off angle.

A more elegant way to achieve phase-matching is quasi-phase-matching (QPM), which allows for zero AOI and doesn't require angular crystal tuning. Furthermore, the crystal can be oriented such that the maximum nonlinearity is exploited. In QPM, the wavevector mismatch is compensated by periodically changing the sign of the effective nonlinearity d_{eff} after one coherence length L_c. The coherence length defines the length over which the set wavelength can be still generated. Without phase-matching the energy would flow back and forth between the interacting waves with a periodicity of $2L_c$, i.e. back-conversion sets in after one L_c. The grating period Λ is therefore given by

$$\Lambda = 2L_c = 2\frac{\pi}{|\Delta k|}. \tag{2.36}$$

The condition for momentum conservation $\Delta k = 0$ is thus adapted to

$$\Delta k = k_p - k_s - k_i + \frac{2\pi}{\Lambda}. \tag{2.37}$$

QPM allows for several advantages compared to critical phase-matching. First of all, noncritical phase-matching can be applied, i.e. the incident waves exhibit identical polarization and propagate along a crystal axis. Thus, spatial walk-off is avoided. By adapting the crystal temperature the phase velocities of the propagating waves are matched, i.e. their phase-mismatch is minimized. As previously mentioned zero AOI is achieved and beam-pointing is maintained during frequency tuning.
With QPM high photon efficiencies become feasible, as a higher nonlinearity compared to angular phase-matching can be achieved. Crystals such as periodically-poled lithium niobate (PPLN) became indispensable in near-infrared (NIR) frequency conversion. As one grating period exhibits a limited gain bandwidth, i.e. only supports a limited wavelength range, commercial crystals often contain 10

and more different grating periods. Still, the acceptance bandwidth of each period is limited to a few nanometers. However, by changing the temperature of the crystal the resonance wavelength of the grating period is shifted. Thus, very broad tuning ranges are feasible. As temperature tuning and grating period changes are time consuming, fan-out poled crystal are available meanwhile. Instead of discrete poling periods these crystals provide a continuous grating, which changes over the crystal width and makes temperature tuning dispensable. For wavelength tuning the crystal position just needs to be laterally changed. Thus a gap-free tuning range, similar to periodically poled crystals in combination with temperature tuning is achieved.

Parametric oscillation, amplification and DFG

Optical parametric oscillation, amplification and difference frequency generation basically depict the identical process of mixing a pump and seed photon at frequencies ω_p, ω_s respectively. In consequence of the nonlinear response the pump photon is annihilated and a new seed photon and an idler photon of energy $\hbar\omega_i = \hbar\omega_p - \hbar\omega_s$ are generated. It is $\hbar\omega_p > \hbar\omega_s > \hbar\omega_i$. Thus, the seed beam is amplified and a new idler beam is generated. Fig. 2.6 depicts the corresponding energy diagram. The dotted energy level represents a virtual energy state to account for the parametric process. Parametric amplification and DFG are distinguished by the available gain.

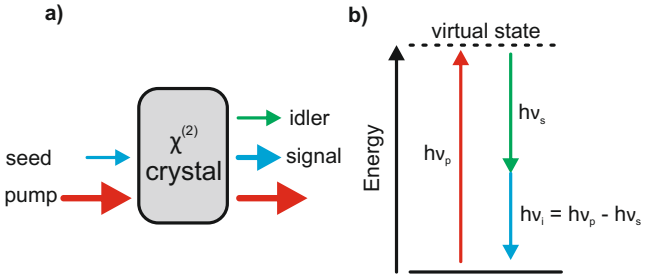

FIGURE 2.6. In DFG and optical parametric amplification (OPA) a strong pump beam and weak seed beam are spatially and temporally overlapped in a nonlinear $\chi^{(2)}$ gain medium. During the interaction the seed beam is amplified and an idler beam is generated (a). For each signal and idler photon one pump photon is annihilated. This response results from dipolar oscillations, exhibiting a nonlinear restoring force, which are induced by the incident electromagnetic fields. No energy is transferred to the gain medium. A schematic energy structure is depicted in b).

The interaction of pump and seed fields in the nonlinear medium is expressed by the *coupled-amplitude equations*, which relate the associated field amplitudes A_p, A_s, and A_i [26].

$$\frac{dA_s}{dz} = \frac{2i\omega_s d_{eff}}{n_s c} A_p A_i^* e^{i\Delta kz} \tag{2.38a}$$

$$\frac{dA_i}{dz} = \frac{2i\omega_i d_{eff}}{n_i c} A_p A_s^* e^{i\Delta kz} \tag{2.38b}$$

In Eq. (2.38) d_{eff} denotes the effective nonlinearity along the propagation direction. It is derived from the nonlinearity tensor $d_{ijk} = \frac{1}{2}\chi^{(2)}_{ijk}$ by accounting for the crystal structure and symmetry.

To solve Eq. (2.38) zero pump depletion, an initial seed field amplitude $A_s(0)$ and zero initial idler amplitude are assumed. Thus, the resulting signal and idler fields are [26]

$$I_s(L) = I_s(0)\left(1 + \frac{\Gamma^2}{g^2}\sinh^2(g \cdot L)\right), \tag{2.39a}$$

$$I_i(L) = I_s(0)\frac{\lambda_s}{\lambda_i}\frac{\Gamma^2}{g^2}\sinh^2(g \cdot L). \tag{2.39b}$$

The available gain g is given by the exponential gain coefficient Γ, which is decreased by the wavevector mismatch $\Delta k = k_p - k_s - k_i$. It is

$$g = \sqrt{\Gamma^2 - \left(\frac{\Delta k}{2}\right)^2}, \text{ with} \tag{2.40a}$$

$$\Gamma^2 = \frac{8\pi^2 d_{eff}^2}{n_i n_s n_p \lambda_i \lambda_s \varepsilon_0 c} I_p. \tag{2.40b}$$

Assuming perfect phase-matching, i.e. $\Delta k = 0$, and high gain $\Gamma L \gg 1$, the signal and idler intensities grow with $e^{\Gamma L}$, whereas the idler intensity depends linearly on the seed power. The exponential growth of both fields is explained by their mutual stimulation, as both act as "seed" sources. For an exponential growth, the seed power amplification can reach a single-pass gain

$$G = \frac{I_s(L)}{I_s(0)} \approx \frac{1}{4}e^{2\Gamma L} \tag{2.41}$$

on the order of 10^6 [26]. Therefore, this process is denoted as *optical parametric amplification*. By inserting Eq. (2.40b), we see that $G \propto e^{d_{eff}\sqrt{I_p}\cdot L}$. Note that the generated idler intensity is linearly proportional to the applied seed intensity $I_s(0)$, but it scales exponentially with the applied pump power.
Whereas OPA is a single-pass process, optical parametric oscillation (OPO) is achieved by setting up a cavity, in which the signal

and/or idler fields oscillate. Solely the pump field is incident and the signal and idler fields are generated in the gain medium from vacuum fluctuations, i.e.optical parametric generation (OPG). In consequence of the cavity feedback strong signal and idler fields are generated after several round trips and serve as efficient seed beams for the OPA process.
In contrast to parametric amplification, the term DFG is particularly used to describe the generation of MIR light at very low gain $\Gamma L \ll 1$. Thus, it is assumed that the wavevector mismatch is larger than the exponential gain coefficient $\Gamma < \frac{\Delta k}{2}$ [27], which means that the gain coefficient g given in Eq. (2.40a) becomes imaginary. It is rewritten in the form $g = i\tilde{g}$. Inserting this into Eq. (2.39), the resulting signal and idler intensities show oscillatory behavior instead of an exponential, continuous growth over the propagation distance L. The idler or DFG intensity is [27]

$$I_i(L) = I_s(0)\frac{\lambda_s}{\lambda_i}\Gamma^2 L^2 sinc^2\left(\tilde{g}L\right) \propto \frac{d_{eff}^2 \cdot L^2}{\lambda_i^2} I_s(0) I_p. \tag{2.42}$$

This means that the generated idler intensity, i.e. power, is proportional to the applied seed and pump power and both contribute linearly. This is in great contrast to OPA, where an exponential pump power dependency is observed.
The efficiency of a parametric process is depicted by the *photon efficiency*

$$\eta_{ph} = \frac{P_{s,i}}{P_p} \cdot \frac{\lambda_{s,i}}{\lambda_p}, \tag{2.43}$$

which maps the number of converted pump photons into signal or idler photons.
Another measure to express the performance is the *power conversion efficiency*, which is

$$\tilde{\eta} = \frac{P_{DFG}}{P_p}. \tag{2.44}$$

If the applied pump and seed power are similar, it is [25]

$$\tilde{\eta} = \frac{P_{DFG}}{\sqrt{P_p P_s\,(0)}}. \tag{2.45}$$

Assuming Gaussian Beams, maximum efficiency is achieved if the crystal length and confocal parameters of the interacting beams satisfy [28]

$$\frac{L}{b} = 2.84, \tag{2.46}$$

which is also known as *Boyd's criterion*.
So far, I neglected efficiency limiting effects due to dispersion, such as spatial and temporal walk-off. These effects determine the actual interaction length of the incident beams in the nonlinear gain medium. To achieve more realistic results, the so far used crystal length L should be replaced by the interaction length ΔL.
In consequence of dispersion, the pump and seed fields propagate at different group velocities and will loose their temporal synchronization after ΔL. The so-called *temporal walk-off* is expressed by the group-velocity mismatch (GVM) Δ_{ij} of the interacting pump and seed beams. It is in general defined as [13]

$$\Delta_{ij} = \left(\frac{\partial k}{\partial \omega}\right)_i - \left(\frac{\partial k}{\partial \omega}\right)_j = \frac{1}{v_{g,i}} - \frac{1}{v_{g,j}}. \tag{2.47}$$

The pulses are separated if the transit-time difference exceeds the pulse duration. Thus, the interaction length limited by the temporal walk-off is

$$\Delta L_t = \frac{\tau_p}{|\Delta_{si}|}. \tag{2.48}$$

To determine the achievable interaction length due to spatial walk-off Eq. (2.34) and the beam waists inside the crystal need to be considered. Here, a balance between applied intensity (i.e. beam waist) and interaction length needs to be achieved, as very tight focusing might lead to high gain, but to an extremely short interaction length.

The GVM between the signal and idler beams affects the achievable spectral gain bandwidth (OPA) or acceptance bandwidth (DFG), which describes the FWHM-bandwidth in which $G \geq \frac{G_{max}}{2}$. It is derived by series expanding the wavevector mismatch Δk as a function of frequency. In the first-order, the gain or acceptance bandwidth $\Delta\nu = \frac{\Delta\omega}{2\pi}$ is [27]

$$\Delta\nu = \begin{cases} 2\frac{\sqrt{\ln(2)}}{\pi}\sqrt{\frac{\Gamma}{L}}\frac{1}{|\Delta_{si}|} & \text{for OPA} \\ 0.886 \cdot \frac{1}{L\Delta_{si}} & \text{for DFG} \end{cases} \tag{2.49}$$

with Δ_{si} depicting the GVM between the signal and idler beams. Comparing these results for OPA and DFG, the parametric gain bandwidth exceeds the DFG acceptance bandwidth by $0.6\sqrt{\Gamma L}$ [27]. The dependence of the acceptance/gain bandwidth on the gain is also denoted as *gain broadening*.
OPAs in the NIR typically employ QPM. In contrast, most DFG gain media require angular phase-matching. By calculating the acceptance bandwidth $\Delta\theta$ for Type-I (T-I) and Type-II (T-II) phase-matching, several differences are observed. In general, the spectral acceptance bandwidth for T-I phase-matching exceeds the T-II acceptance bandwidth. Furthermore, $\Delta\nu_{T-I}$ increases towards degeneracy, whereas $\Delta\nu_{T-II}$ stays rather constant over the entire tuning range. In general, this allows to optimize the nonlinear process depending on the desired output. In [12] we observed higher output power at longer wavelength for T-II phase-matching.
To compare different nonlinear gain media, a useful parameter is the figure of merit

$$FOM = \frac{d_{eff}}{\sqrt{\lambda_i\lambda_s n_i n_s n_p}}. \tag{2.50}$$

At last, I would like to point out that there is no strict boundary between OPA and DFG. In [12, 24] we reported several ten percent photon conversion efficiency for a "classical" DFG setup. To differentiate in which gain regime the frequency conversion takes place,

I recommend to measure the output power in dependence of the applied pump power for a constant seed power, as the pump power contributes exponentially in the high gain regime and linearly in the low gain regime.

2.5 PARAMETRIC NIR LIGHT SOURCE

In this thesis cascaded parametric frequency conversion is employed to achieve a broadband tuning range from 1.3 to 20 µm. All setups are based on a solid-state pump oscillator at 1 µm wavelength. Then a fiber-feedback optical parametric oscillator (FFOPO) and an OPA are used to reach the near-IR spectral region from roughly 1.3 to 4.6 µm. This concept allows for a very compact setup and provides excellent long-term and peak-to-peak stability. As a FFOPO is rarely used and greatly differs from a bulk free-space OPO, a short introduction is given here.
The design of the utilized FFOPO is based on the setup presented in [29]. As a nonlinear gain medium, fan-out lithium tantalate or periodically-poled lithium niobate crystals are used in the linear cavity design. In contrast to a free-space OPO, the largest part of the cavity (2 m fiber-length at $f_{rep} \approx 40$ MHz) is transferred into a single-mode fiber instead of using several folding mirrors and free-space propagation. This allows for a very stable and compact setup, as the propagating beam becomes insensitive regarding ambient conditions, air flow, mechanical vibrations and drifts of optical components, which are critical issues in free-space OPOs. Furthermore, the oscillating signal pulses experience a slight temporal broadening in the fiber. This effectively stabilizes the temporal overlap with the incident pump pulses. Whereas active electronic stabilization is required in free-space OPOs, the FFOPO is passively stable. The FFOPO is singly-resonant for the signal wavelength, whereas residual pump and idler frequencies are filtered. The oscillating signal pulses are outcoupled directly after passing the gain medium, i.e. no pulse broadening due to the feedback-fiber is observed on the

outcoupled signal pulses.
As the fiber can be stored very compactly, a FFOPO has a footprint as small as about 15×20 cm.
The utilization of an OPA for amplifying the signal and generating the idler, allows for an excellent peak-to-peak stability and, in consequence of its high single-pass gain, for high output power and conversion efficiency. Excellent long-term stability for both signal and idler is achieved due to the employed seed source. A basic discussion of this concept is given in [30] and its good performance is proved in [31–38].

2.6 FTIR SPECTROSCOPY

FTIR spectroscopy provides a high sensitivity and signal-to-noise ratio (SNR) [4], a high spectral accuracy [6], as well as a high optical throughput [5] and thus fast measurements. State-of-the-art commercial devices allow for measurements over broad spectral ranges from the visible to the far-infrared by operating different detectors and light sources (*Globars*) and changing critical optical components (e.g. beamsplitters) automatically. High spectral resolution well below 1 cm^{-1} can be achieved, which makes FTIR spectroscopy are very versatile and robust tool for chemical analysis in both research and industry.

FTIR basics

In contrast to dispersive spectrometers, fourier-transform Infrared (spectrometer/spectroscopy) (FTIR) spectrometers are able to measure broadband spectra at once. This is accomplished by generating the interferogram of the light beam in a *Michelson interferometer* and then Fourier-transform it to derive the spectrum. This allows for fast scans, but also allows for a high spectral resolution, which

is given by the optical path length d of the moving mirror. The spectral resolution $\Delta\tilde{\nu}$ is given by

$$\Delta\tilde{\nu}\left[\mathrm{cm}^{-1}\right] = \frac{1}{d\,[\mathrm{cm}]}. \tag{2.51}$$

Thus, an optical path difference of 1 cm between the interferometer paths yields a spectral resolution of $1\,\mathrm{cm}^{-1}$. Still, a finite optical path length can lead to distortions in the derived spectrum, as the interferogram might not be recorded completely. To avoid distortions an *apodization function* is applied to the interferogram. It is unity at the interferogram center and becomes zero at the edges. A Gaussian function is a prominent example.
Due to the finite data sampling, the measured interferogram is a discrete data set. Due to the discrete Fourier-transformation the calculated spectrum might exhibit lower spectral resolution as technically achievable. This is overcome by *zero-filling* or *padding*, which means that zeros are added to the interferogram's edges, i.e. where it already is zero. Thus, no information is added, but a higher spectral resolution is achieved as more data points are available for the discrete Fourier-transform. Of course the physical limit of the spectral resolution given by Eq. (2.51) remains unchanged.
At last, the sampling interval allows to calculate the spectral bandwidth. If a given path length d is sampled into m equidistant steps, the maximum frequency ν_{max} is given by

$$\nu_{max}\left[\mathrm{cm}^{-1}\right] = \frac{m}{2d}. \tag{2.52}$$

Note that the symmetry of a discrete Fourier-transformation is described by the factor 2 in the denominator.

Conducting measurements

In order to derive the extinction of a sample two spectra need to be measured in FTIR spectroscopy. First a *reference* or *background spectrum* is conducted. It contains the extinction of the ambient conditions and bare light source spectrum. Then a *sample spectrum* is measured. Each background and sample spectrum can consist of multiple averaged scans to compensate for fast fluctuations. The vibrational signal from the sample is derived by normalizing the sample spectrum to the background, as shown in Eq. (2.53). Ideally, the signal spectrum shows a flat line of magnitude 1 with the vibrational signal as modulations on top of it. It is also commonly given in % and denoted as 100 %-line.

$$\Delta S = \frac{S_{sample}}{S_{background}} \tag{2.53}$$

By dividing the sample and background spectra, small changes between the spectra become visible. However, similar changes might be also introduced by fluctuations in ambient conditions, such as air flow, temperature or humidity changes, by mechanical drifts of the measurement setup or by spectral and power fluctuations of the light source. Especially at longer integration times this needs to be considered. Noise can appear on the signal spectrum in the following forms:

- Tilted and/or shifted spectra in consequence of spectral and power drifts, caused by the light source and/or mechanical drifts of the setup.
- root-mean-square (RMS) noise due to fast fluctuations of the ambient conditions, light source, or electronic detection noise.

Therefore it is recommended to use a short integration time for each background and sample spectrum, which accounts for fast fluctuations, and then record background and sample spectra alternating over a longer period of time. The measured signal spectra $\Delta S(\nu)$ are then averaged to account for mechanical instabilities and other slow noise sources. During the experiments, which are conducted in this thesis, each background and sample spectrum is typically integrated for about 7 s, resulting in 14 s integration time for a signal spectrum ΔS. Signal spectra are then averaged for up to 8 h depending on the utilized light source.

Micro-FTIR spectroscopy

To reach a spatial resolution in the µm-range, a microscopy setup is employed for the sample illumination. This allows tighter focusing, but still the minimum beam waist is limited to several tens or even hundreds of µm, in consequence of the broadband, incoherent black body radiation. A higher resolution is achieved by using an adjustable aperture, which limits the detected light to a certain sample area. With a Globar, minimum aperture sizes are on the order 40×40 µm², although smaller apertures of 10×10 µm² could be used. However, this goes along with increased noise as about 80 to 90 % of the incident radiation is blocked. Longer integration times are therefore required. Using other light sources, such as lasers or synchrotrons smaller aperture sizes can be used. An important measure to quantify the light source is the *brilliance*, or also known as *radiance*. In brief, it gives a time and area dependent photon density. as given in Eq. (2.54). The higher the photon density is, the lower is the electronic detection noise. The brilliance is given by the photon flux per second per unit area ΔA, unit solid angle $\Delta\Omega$ and within the 0.1 % bandwidth.

$$B = \frac{\Phi_{ph}}{A \cdot \Delta\Omega \Delta f_{0.1\,\%\mathrm{BW}}} \tag{2.54}$$

A Globar reaches a brilliance on the order of 10^{15} ph/s/mm²/sr/0.1 %BW [38], whereas synchrotrons [39] or intrapulse DFG laser sources [40] reach an about 3 orders of magnitude higher brilliance. A parametric laser source can exhibit a 5 orders of magnitude higher brilliance, as shown in [38].

Using external light sources

To couple an external light source to the spectrometer, the external beam needs to be mode-matched on the thermal beam, as the spectrometer design is optimized for the included Globar.
By applying different light sources on a sample the spectral response might differ slightly. In [32] the authors observed a spectral shift measuring plasmonic nanoparticles using a laser in comparison to a Globar. This shift is explained by the different illumination geometry at the sample position, as the wave fronts of a Globar beam significantly differ from a Gaussian laser beam. Similar effects might be observed for other samples.

Noise investigation

To quantify the sensitivity of different light sources for FTIR spectroscopy, the RMS noise of the measured 100 %-lines is calculated according to Eq. (2.55). The data set is normalized using its mean value. In Eq. (2.55) the data points are denoted as x_n, whereas the sum of all data points is given by N.

$$RMS\,[\%] = \sqrt{\frac{\sum_1^N \left(1 - x_n\right)^2}{N}} \cdot 100 \tag{2.55}$$

During the experiments that are conducted in this thesis, the RMS noise is typically calculated within the $1/e^2$-width of the laser spectrum. The input data sets consist of 100 %-lines measured *without a sample* to derive the intrinsic measurement noise. To derive the mean RMS noise of a single spectrum, the noise of the measured 100 %-lines is calculated and then averaged. In contrast, to derive the noise corresponding to a specific integration time, the 100 %-lines are averaged prior to the RMS calculation.

Signal-to-noise ratio

The SNR is derived according to

$$SNR = \frac{A_{signal}}{RMS}, \tag{2.56}$$

with the signal amplitude A_{signal}. In this thesis, a Lorentzian baseline correction is applied to derive the signal amplitude, as a plasmonic structure is employed for signal enhancement. Details are indicated during the discussion of the measurements in Chapter 5.

Sensitivity and detection limit

The accessible measurement sensitivity S for FTIR measurements is calculated by assuming a SNR of 1. According to Eq. (2.56) the minimum signal amplitude is $A_{signal} = RMS$. The detection limit, or *single-shot sensitivity* is reached if a single 100 %-line is used, whereas I utilize the term sensitivity for a certain integration time.

Light source and setup stability

To derive the light source and setup stability, individual spectra (no 100 %-lines) are employed to track the central frequency, bandwidth and intensity over time.

2.7 SURFACE-ENHANCED INFRARED ABSORPTION

IR spectroscopy is a powerful tool for chemical analysis, as material specific resonances are located in the MIR spectral region. However, it is generally hampered by the low molecular absorption cross-sections ($\sigma_{abs} \approx 10^{-20}$ cm^2), which lead to an inefficient and weak excitation. Therefore, relatively high sample concentrations are needed and the detection of single molecules is not feasible with e.g. standard FTIR spectroscopy. To overcome this limit, SEIRA is employed. It allows for a molecular signal enhancement of several orders of magnitude and thus, the reduction of the detected material concentration. Collective electronic oscillations at the surfaces of metal nanostructures, so-called *surface plasmon polaritons*, couple to the molecular vibrations and serve as highly efficient excitation pathways. In the following a brief introduction into SEIRA is given. For simplicity, a single gold nanoantenna is assumed as a metallic nanostructure, and polypeptides are adsorbed on the antenna. First, the resonance wavelength of the nanoantenna along the long symmetry axis is considered. It is given by

$$\lambda = 2L \cdot n \cdot a_1 + a_2, \tag{2.57}$$

as depicted in [41]. The resonance wavelength depends linearly on the antenna length L and the refractive index n of the surrounding medium. a_1 denotes the antenna geometry and material, a_2 accounts for the phase of the reflection at the antenna end. The resonantly excited plasmonic vibration can be considered as a standing

wave phenomenon, comparable to radio frequency antennas. The physical effect is described by a mixed state between the electronic oscillation along the antenna axis and the localized photons at the antenna surface. The corresponding quasi-particle is denoted as *surface plasmon polariton*. The plasmonic oscillation is characterized by a strong electromagnetic field confinement within a few tens of nanometers around the tip ends of the antenna [41–43], as depicted in Fig. 2.7a). The near-field can be up to 100 times more intense than the electromagnetic field without the plasmonic structure. In SEIRA the field confinement is exploited to detect minimum amounts of molecules, as only those molecules are excited, which are located at the antenna ends. Due to the intense near-field, efficient molecular excitation is achieved.

The antenna and molecular resonances are coupled by matching their resonances. Thus, the easily excitable antenna serves as an efficient excitation pathway for the "dark" molecular vibration. The enhanced, narrowband molecular signal is observed as a modulation on top of the broad plasmonic resonance, as illustrated in Fig. 2.7b). An intuitive description is given by the refined *coupled harmonic oscillators model* from Adato et. al [44], which also accounts for intrinsic, i.e. non-radiative material absorption, and external, i.e. radiation into the far-field, losses of the plasmonic antenna. For efficient SEIRA the antenna length L is tailored with respect to the desired resonance frequency, whereas the antenna material and aspect ratio need to be chosen such that the a balance between radiative and absorptive losses is achieved. In [45] the signal enhancement is measured as a function of resonance detuning $R = \omega_{vib}/\omega_p$, where ω_{vib}, ω_p denote the molecular and plasmonic resonances, respectively. Optimum enhancement is observed at R being slightly smaller than 1. This is in consequence of a slight red shift of the light in the antennas near-field, compared to the far-field response [42, 46].

In this thesis the utilized nanoparticles are made of gold, as it exhibits a nearly perfect Drude-type dielectric function in the IR and a

low damping rate, enabling sharp plasmonic resonances. Due to its chemically stability it is ideal for (biomedical) sensing applications.

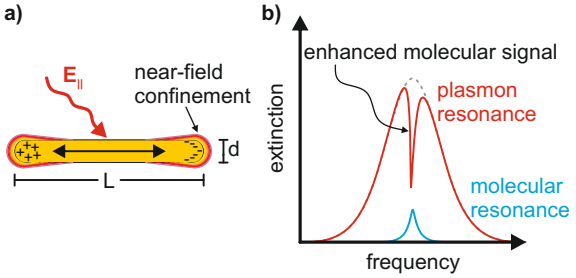

FIGURE 2.7. **a)** Sketch of a resonantly excited nanoantenna. The plasmon oscillation is excited by illumination with resonant electromagnetic radiation polarized along the antenna axis, i.e. parallel polarization. In consequence of the collective electronic oscillation electromagnetic radiation is confined around the tip ends (nm-range). This near-field can be up to 100-times more intense than the incident electromagnetic field. **b)** Schematic drawing of a typical SEIRA extinction spectrum. The antenna and molecular resonances are matched and the molecular vibration couples to the plasmonic oscillation. Thus the "dark" molecular resonance is excited and observed as a modulation on the plasmonic resonance at enhanced amplitude. In a grey line-color the bare plasmonic resonance is depicted.

3

ULTRAFAST, HIGH REPETITION RATE YB:CAF_2 LASER

Ultrashort laser pulses at high repetition rates are of high importance for e.g. broadband IR spectroscopy or time-resolved material analysis. Todays work-horses are Ti:Sa and Yb-based lasers. The latter radiate between 1030 and 1050 nm central wavelength and enable the efficient generation of near- and mid-infrared radiation exploiting parametric frequency generation. They are pumped by high-power laser diodes at 980 nm, thus allowing for a low complexity, high robustness, and a small footprint. In contrast, Ti:Sa oscillators are usually pumped by frequency-doubled solid-state lasers to achieve comparable output power. Lasing is achieved from 630 to 950 nm. In consequence of the broad gain bandwidth, very short pulse durations as short as 5.5 fs [47, 48] can be achieved. However, due to their shorter emission wavelengths, the generation of mid-IR radiation is more challenging. For that purpose 1 µm-pumping is beneficial, in consequence of the available gain material properties.

In this chapter, Yb:CaF_2 is investigated as a an alternative material for the commonly used Yb:KGW and Yb:CALGO crystals. It exhibits higher thermal conductivity, an extremely long excited state lifetime and lower dispersion. First laser cavities have been demonstrated reaching pulses as short as 68 fs [49]. However, the so-far presented output power remained low (mW to max. 2.3 W[49]). The goal of the following experiments is to set up a laser system that allows for short pulse durations close to 100 fs and several W output power. We aim for a short pulse repetition rate of 40 MHz,

whereas Yb:CaF_2 oscillators have been predominantly operated at 80 MHz and higher.

3.1 PROPERTIES OF YB-DOPED CaF_2

Already in the 1960s CaF_2 has been used as a laser host material [50]. In fact, one of the first diode-pumped lasers was built using it [51]. In the beginning, CaF_2 was doped with Nd^{3+}, but despite promising properties it was replaced by other host media, such as YAG soon after. This was due to the strong tendency of rare-earth doped fluorides to form complex site structures. In consequence, parasitic energy transfers close to the laser transition occur, reducing the laser efficiency significantly. Approaches to control this side structure formation had little effect.
This changed with the discovery of the properties of Yb-doped CaF_2 [52] and improved manufacturing processes. Yb^{3+} exhibits a simpler energy structure and no parasitic energy transfers occur. Incorporated into CaF_2, a laser gain medium is formed that provides reasonable absorption and emission cross-sections, low dispersion, a high damage threshold, a very high thermal conductivity, comparable to YAG, and an extremely long excited state lifetime [53, 54], as depicted in Table 3.1. Especially the last two properties are highly beneficial for high power lasing or laser amplifiers.
Table 3.1 depicts the material parameters in comparison to Yb:KGW and Yb:CALGO. Yb:CaF_2 exhibits a 4 to 6 times longer lifetime than Yb:KGW and Yb:CALGO, reaching 2.4 ms [51]. A long lifetime is beneficial for high power applications, as more energy is stored in the gain medium, and might allow for lower intensity noise. On the other hand, Yb:CaF_2 exhibits a low emission cross-section. This causes a strong tendency towards Q-switching, impeding soliton mode-locking [20].

	Yb:CaF_2	Yb:KGW	Yb:CALGO
τ_L (ms)	2.4	0.6	0.42
σ_{em} (10^{-20} cm²)	0.25	2.8	0.8
σ_{abs} (10^{-20} cm²)	0.54	12	1.65
$\sigma_{em} \cdot \tau_L$ (10^{-20} µs · cm²)	600	1680	336
$\Delta\lambda_{em}$ (FWHM) (nm)	30	25	80
minimum τ_p (fs)	36	44	14
κ (W/m/K)	9.7	3.3	11.4

TABLE 3.1. Material parameters of Yb:CaF_2, Yb:KGW and Yb:CALGO. Yb:CaF_2 exhibits a very long excited-state lifetime lifetime of the upper laser level (τ_L), as well as a reasonable high thermal conductivity thermal conductivity (κ), which makes it a promising candidate for high-power applications. However, the emission and absorption cross-sections emission cross-section (σ_{em}), absorption cross-section (σ_{abs}) are fairly low, which makes Q-switching probable. The spectral emission bandwidth $\Delta\lambda_{em}$ is comparable to Yb:KGW. This results in a theoretical minimum pulse duration of $\tau_{p,min} = 36$ fs at the Fourier-limit. Data from [53, 54].

3.2 SETUP

The initial setup design is based on the designs presented in [55, 56], whereas we ultimately aim for lower repetition rates. Fig. 3.1 depicts the cavity design. A fiber-coupled laser diode with 25.5 W output power at a wavelength of 981 nm power and an NA of 0.15 at 106.5 µm fiber diameter is used to pump the oscillator. It is focused into the crystal to about 64 µm beam waist. Including the losses from the collimation ($f = 30$ mm) and focusing lenses ($f = 50$ mm), as well as the dichroic incoupling mirror, about 20 W pump power can be applied to the Yb:CaF_2 oscillator.
A 2 mm-long Yb:CaF_2 with 4.5 at % doping (*Eksma Optics*) is used. It is placed on a copper heat sink, which is temperature controlled ($T \approx 18$ °C using a peltier element and water cooling. The crystal

position can be adjusted within ±1.25 cm range. Dispersion management is conducted using two gires tournois interferometer (GTI) mirrors, adding −2200 fs^2 per round-trip to the cavity. A SESAM is used for stable soliton mode-locking. Its position can be adjusted within ±1.25 cm as well. 5 % of the intracavity power are finally outcoupled.

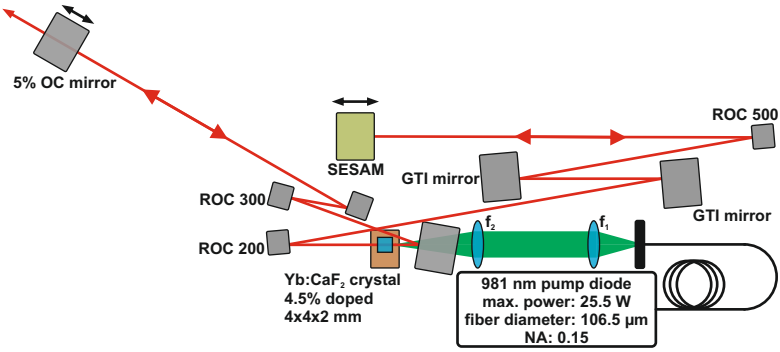

FIGURE 3.1. Design of the diode-pumped Yb:CaF$_2$ laser. A heavily doped crystal of 2 mm length is used. For stable mode-locking the SESAM position can be varied within ±1.25 cm and the dispersion is carefully controlled using GTIs. The crystal position can be adjusted within a ±1.25 cm range. The pump beam is collimated using a $f_1 = 30$ mm lens and focused into the crystal with a $f_2 = 50$ mm lens.

The caustic of the cavity design is depicted in Fig. 3.2. The SESAM is located at the 0 mm-position, whereas the OC-mirror is at 1860 mm on the x-axis. The cavity is designed for a pulse repetition rate of 80 MHz. The outcoupled beam is expected to be about 2 mm in diameter. Using this cavity design, the beam sizes in the crystal and on the SESAM are relatively small, in order to reach a high intensity and achieve a low lasing threshold and stable soliton mode-locking.

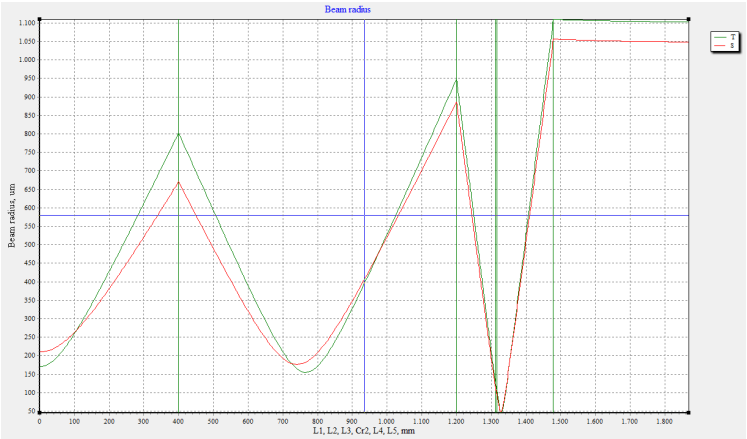

FIGURE 3.2. Caustic of the cavity design with 80 MHz repetition rate. The SESAM position is found on the left ($x = 0$), the crystal position at around 1330 mm, and the outcoupling mirror is on the right end with a beam waist of about 1055 µm.

3.3 RESULTS

First, the laser cavity is operated in the CW regime. For that purpose, the SESAM is replaced by a highly reflective mirror. The output power is shown in Fig. 3.3, with a threshold pump power of 1 W. A continuous increase is observed until the output power saturates at 3 W.
The given pump power denotes the applied power and is measured directly in front of the crystal, thus accounting for losses due to pump optics. Thus, a slope efficiency of 28.4 % is achieved.
Directly behind the crystal 34 % residual pump power is detected. But by accounting for losses at the crystal holder, we assume that about 40 % of the applied pump power is transmitted, thus the pump power extinction reaches about 60 %, including scattering on the crystal end facets, heat dissipation and more. The absorbed pump power is therefore expected to be lower, thus the conversion efficiency might be on the order of 30 to 40 %.

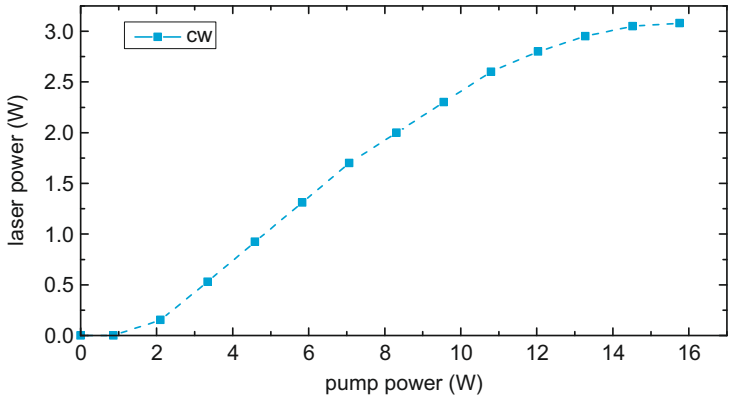

FIGURE 3.3. Generated CW laser power versus pump power. 1 W pump power is required for lasing and output power saturation is reached at 3 W. A slope efficiency of 28.4 % is calculated.

Next, the saturable absorber mirror is reinserted into the cavity. It is designed for a central wavelength of 1040 nm, exhibits a relaxation time of 1 ps, and a low intensity absorption of 1 %. The saturation fluence is 70 µJ/cm² and the modulation depth reaches 0.6 %. Stable mode-locking is achieved at 79.9 MHz pulse repetition rate. Q-switching is observed, but could be avoided by optimizing the cavity.
A maximum output power of 3.15 W is measured using 5 % outcoupling ratio, whereas different ratios are investigated as well. Fig. 3.4 depicts the generated laser power depending on the outcoupling ratio. As a guide to the eye, a fit is added according to Eq. (2.15a). As visible, a maximum is reached at 6 %.

For the generation of ultrashort pulses, the dispersion is optimized in the following. Table 3.2 summarizes these experiments, depicting the inserted dispersion per round-trip using different GTI mirrors. Finally, stable mode-locking is achieved at a central wavelength of 1050.1 nm, exhibiting 6.5 nm bandwidth (FWHM), as depicted in Fig. 3.5a), and a maximum output power of 2.6 W. A

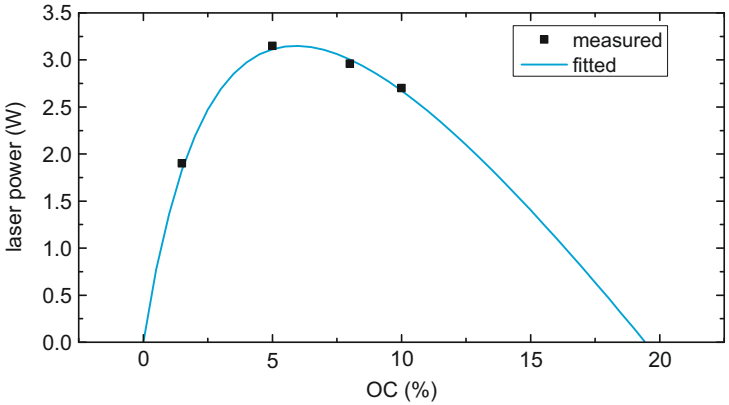

FIGURE 3.4. Measurement of the laser output power for different output coupler mirrors. As a guide-to-the-eye, a fitted line is added according to Eq. (2.15c). At 6 % outcoupling ratio, maximum output power can be achieved.

corresponding pulse duration of 194 fs is measured, giving a time-bandwidth product of 0.35. Thus nearly Fourier-limited pulses are generated. In this configuration, only one GTI mirror providing $-250\,\mathrm{fs}^2$ is used, whereas the other GTI is replaced by a highly reflective mirror. Unfortunately, these mirrors exhibit higher losses, compared to the original setup, which reduces the achievable output power to 2.6 W. A further reduction of the dispersion, did not allow for stable soliton mode-locking.
By monitoring the spectrum for several tens of minutes, CW spikes are observed occasionally. It is avoided by reducing the output power to about 90 %. Fig. 3.5b) depicts a long-term measurement of the laser output power. It exhibits fluctuations of 0.66 %rms, whereby it drops by about 30 mW. However, the measurement exhibits a specific pattern every 5 minutes. This is attributed to the water cooling, as it matches the cooling cycles of the used chiller.

To summarize these first results, an Yb:CaF_2 oscillator is presented, which provides up to 2.6 W stable output power, 194 fs

Dispersion/round-trip (fs^2)	λ_c (nm)	$\Delta\lambda$ (nm)
−2200	1049.5	2.9
−1100	1052.0	5.4
−500	1050.1	6.5

TABLE 3.2. Added dispersion per cavity round-trip using different GTI mirrors. Stable soliton mode-locking is achieved down to a minimum dispersion of −500 fs², reaching 6.5 nm (FWHM) broad laser pulses and a pulse duration of 194 fs . The TBP is close to the Fourier-limit reaching 0.35.

short pulses at 79.9 MHz pulse repetition rate and a central wavelength of 1050.1 nm. The laser output reaches a bandwidth (FWHM) of 6.5 nm. Thus, nearly Fourier-limited pulses are achieved (TBP: 0.35).

3.4 REPETITION RATE REDUCTION

To match our typically used parametric frequency conversion setup, we aim for a lower repetition rate between 40 to 60 MHz. As the intracavity pulse energy increases (assuming similar output power), Q-switching is expected to be avoided more efficiently. On the other hand, this impedes the generation of short pulses, as double pulses might form earlier [57]. Therefore, most Yb-based solid-state lasers delivering 100 fs pulses are operated between 70 to 80 MHz.
The new cavity is designed such that the mode size at the critical optical elements remains comparable to the previous design, as a good performance was observed. Fig. 3.6 depicts the setup design. The caustic is illustrated in Fig. 3.7. In comparison to the previous design (Fig. 3.2), the focusing into the crystal is less tight, with a larger minimum beam waist of about 75 µm to improve the mode-matching between pump and laser mode.

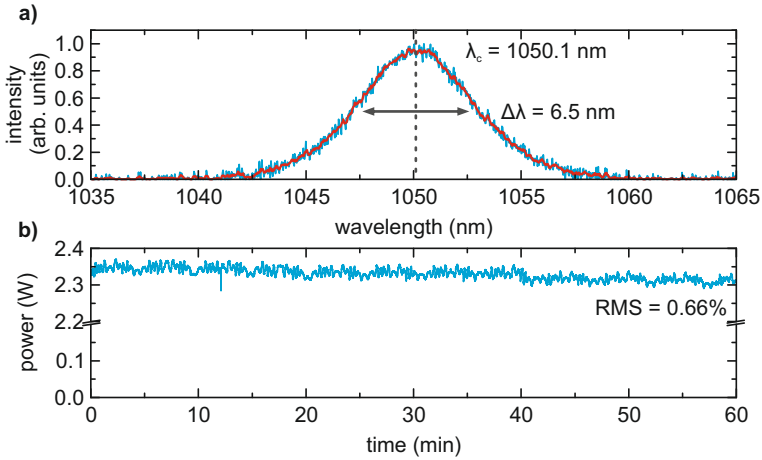

FIGURE 3.5. **a)** Spectrum of the laser output, exhibiting 6.5 nm bandwidth (FWHM) at 1050.1 nm central wavelength. Nearly Fourier-limited, 194 fs-long pulses are achieved. **b)** Generated output power monitored for 60 minutes. A slight loss is observed, as well as a repeating pattern with 5 min periodicity. This is attributed to the cooling cycles of our chiller.

In a first test, up to 3.7 W CW output power is generated by using highly reflective mirror instead of the SESAM. This is attributed to the improved mode-matching between pump and oscillating laser radiation, as well as to reduced cavity losses. By re-inserting the SESAM the output power reaches 3.15 W (λ_c =1050.1 nm). As depicted in Fig. 3.8a), a bandwidth of 5.7 nm (FWHM) is observed. The generated pulses are as short as 250 fs, resulting in a TBP of 0.39, which is close to the Fourier-limit. Here, I added $-1000\,\text{fs}^2$ dispersion per round-trip. At lower dispersion strong Q-switching is observed. The pulse repetition rate is 58.7 MHz, as shown in Fig. 3.8b). Output power saturation is setting in at around 3 W output power. The pump power threshold is increased to 2 W pump power, most probable due to increased cavity losses. Fig. 3.8c) depicts the output power as a function of applied pump power for both mode-locked and CW operation (incl. SESAM). Mode-locking is achieved between 1.2 to 3.15 W output power. A slope efficiency

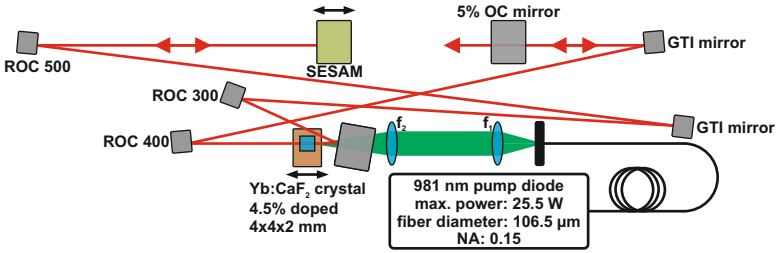

FIGURE 3.6. Setup design for 60 MHz pulse repetition rate. Mirrors with 300 mm and 400 mm radius of curvature (ROC) are used for focusing. This results in 75 µm minimum beam waist.

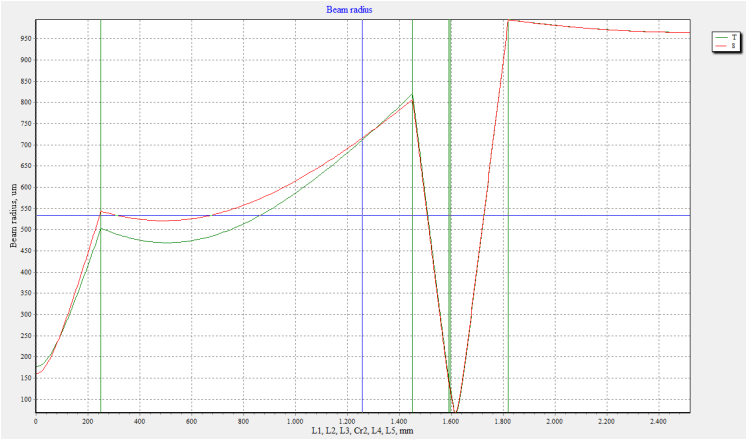

FIGURE 3.7. Caustic of the 60 MHz cavity. The SESAM mirror is at the 0 mm position. Here, the beam waist reaches 170 µm. At the crystal position a minimum beam waist of 75 µm is reached. The outcoupled beam exhibits a beam waist of about 960 µm.

of 38.6 % is calculated, thus exceeding the previously achieved efficiency (see Fig. 3.3 for comparison). This is in consequence of the improved mode-matching between the pump and laser beams.

Fig. 3.9 depicts the laser beam profile at 3 W laser power. Gaussian fits are added and a beam diameter ($1/e^2$) of 2.67×2.80 mm² is

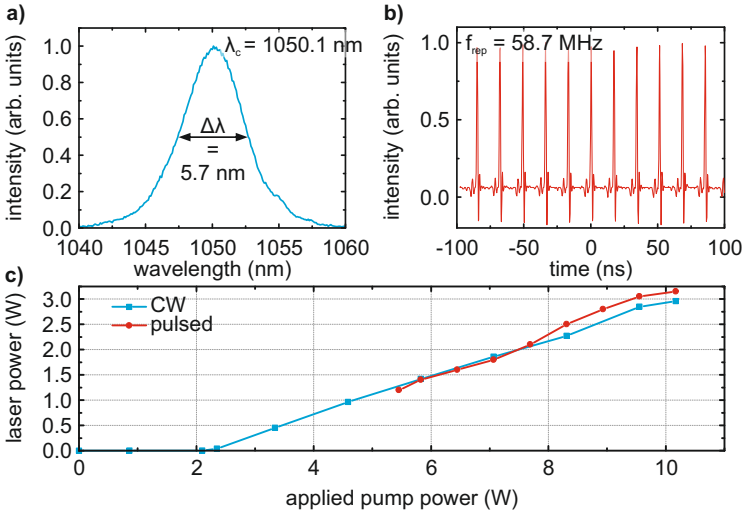

FIGURE 3.8. **a)** Spectrum of the pulses laser. A central wavelength of 1050.1 nm and a bandwidth (FWHM) of 5.7 nm is measured. **b)** Pulse train at 58.7 MHz repetition rate. **c)** Corresponding output power measured in dependence of the applied pump power. Both CW and pulsed operation are shown. The laser threshold is at 2 W pump power. Mode-locking can be achieved from 5.5 W pump power, which corresponds to about 1.2 W generated power. A saturating maximum power of 3.15 W is observed. A slope efficiency of 38.6 % is determined.

determined.

If the output power is increased, the beam profile shows the appearance of a higher mode. CW spikes are simultaneously observed on the spectrum.

As the fluence on the SESAM (1.2 mJ/cm²) is on the same order of magnitude as its damage threshold (3 mJ/cm²) and damages are already observed, it is decreased by increasing the beam waist on the mirror from 170 µm to 245 µm. However, Q-switching is then predominantly observed, whereas soliton mode-locking became highly unstable. In consequence of the low emission cross-section σ_{em} the intracavity power is calculated to be close to the critical Q-switching energy in general. According to Eq. (2.23a) the critical

energy increases from 0.11 to 0.16 µJ by increasing the laser spot size on the SESAM. From a practical point-of-view it is useful to also consider the uncorrected critical energy given in Eq. (2.22), as stable soliton mode-locking is achieved if the pulse energy is closer to this value. Using Eq. (2.22), the critical energy increases from 1.6 to 2.3 µJ. In comparison, the calculated internal pulse energy is on the order of 1.07 µJ. The significant increase of the critical required energy at constant pulse energy explains the increased tendency for Q-switching. Stable soliton mode-locking is achieved only within a small set of parameters and a high fluence on the SESAM is required.
To increase the mode-locking stability and eventually avoid Q-switching a SESAM with shorter relaxation time $\tau_r = 500\,\text{fs}$ is tested. Indeed, Q-switching is avoided efficiently. However, the laser solely exhibits double pulses in this configuration and even by adapting the added cavity dispersion this could not be avoided. In conclusion, the most promising configuration is the utilization of a SESAM with 1 ps relaxation time, $-1000\,\text{fs}^2$ dispersion per round-trip and a high fluence on the SESAM. These parameters are used as a basis for future power scaling.

3.5 OUTLOOK: POWER SCALING

For power scaling a pump diode, which provides up to 60 W pump power is installed. It exhibits a NA of 0.22 at 106.5 µm fiber diameter. Fig. 3.10a) depicts the measured spectrum showing the main peak at 976 nm central wavelength and some noise at slightly shorter wavelength. For comparison, the previously used diode is shown in a blue line color. In grey, the absorption cross-section σ_{abs} of Yb:CaF_2 is added. This data is extracted from [51]. Both laser diodes are close to the optimum absorption wavelength, therefore similar performance is expected.
Fig. 3.10b) depicts the polarization of both pump diodes using a

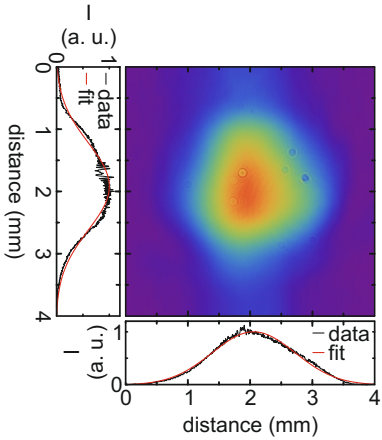

FIGURE 3.9. Beam profile measured at 3 W output power. Gaussian fits are applied along the x and y axis. A beam diameter ($1/e^2$) of 2.67 mm along the x axis, and 2.80 mm along the y axis is determined.

Glan-Thompson prism. Whereas the 25.5 W diode is linearly polarized, the new diode is unpolarized.

Next, the performance of the pump diode is tested at the existing cavity. However, the original pump focusing lens ($f = 50$ mm) is replaced by a $f = 100$ mm lens, as the pump spot seems to be significantly smaller than expected. About 3.5 W CW laser output are generated at 13 W incident pump power, which is comparable to the previous results. However, after several minutes a severe crystal damage is observed, making further experiments impossible. The crystal damages seem to be pump intensity related and a redesign of the pump beam is required in the future.
As an outlook, a cavity design intended to provide about 6 to 8 W output power at 50 MHz repetition rate is given in Fig. 3.13. A detailed scheme is depicted in Fig. 3.11. The corresponding caustic is plotted in Fig. 3.12. The design is based on the previous experiments. To achieve a reliable output, it is build into a solid CNC-cut aluminum box, which is actively temperature stabilized and can be

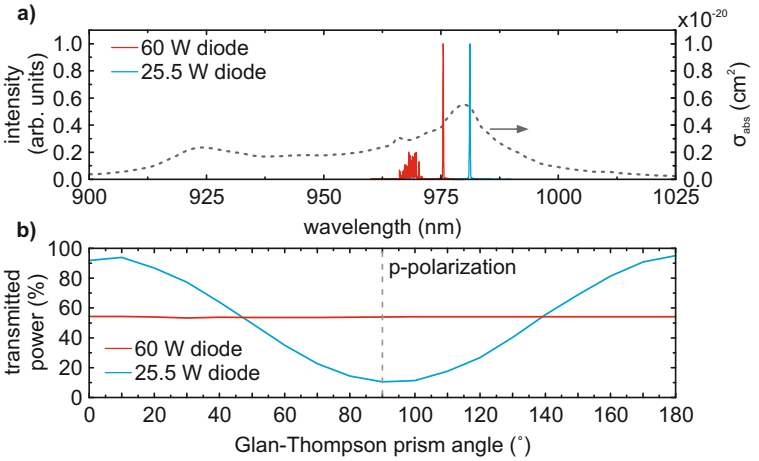

FIGURE 3.10. **a)** Spectra of the high-power and originally used pump diodes. The 25.5 W diode shows a clean spectrum at 981 nm wavelength, whereas the high-power diode is slightly blue-shifted to 976 nm and exhibits noise between 960 and 970 nm. However, both diodes match the peak absorption cross-section well, which is plotted in dashed grey lines in the background. It is adapted from [51]. **b)** Measured polarization of both diodes. The 25.5 W diode is linearly polarized, whereas the high-power diode is unpolarized.

purged with dry air. The repetition rate is intended to be close to our standard frequency converters, such that minor changes are required and that a high tuning range can be achieved.

3.6 CONCLUSION

Two different laser cavities based on Yb:CaF$_2$ have been presented. Initially, the laser was operated at 79.9 MHz repetition rate, exhibiting 6.5 nm bandwidth (FWHM) at 1050.1 nm central wavelength. A pulse duration of 194 fs measured, which is close to the Fourier-limit (TBP: 0.35). 2.6 W maximum output power was achieved at a slope efficiency of 28.4 %. The strong Q-switching tendency in

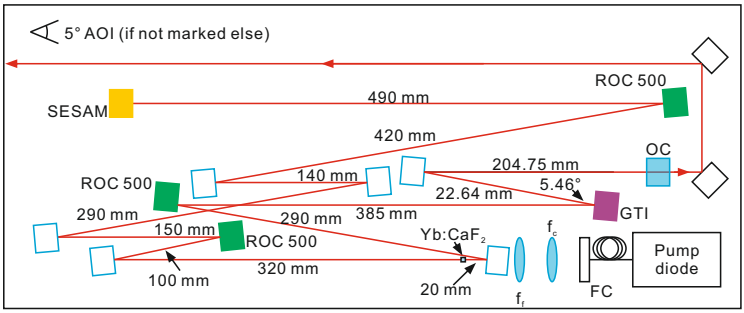

FIGURE 3.11. High power cavity design. Curved mirrors are green, folding mirrors are depicted in blue and GTIs in purple. The collimation and focusing lenses (with f_c, f_f respectively) of the pump beam need to be adapted depending on the utilized laser diode to mode-match the cavity design.
OC: Outcouping mirror FC: Fiber-coupler

consequence of the low emission cross-section was minimum in this configuration.
In a next step, the repetition rate was reduced to 58.7 MHz. In this configuration, a minimum pulse duration of 250 fs was achieved. The pulses were nearly Fourier-limited (TBP: 0.39), showing a spectral bandwidth of 5.7 nm at 1050.1 nm central wavelength. Higher output power (3.15 W) and slope efficiency (38.6 %) were measured due to an optimized mode-matching between pump and laser beam. The maximum output power was limited by SESAM losses and up to 3.7 W are possible by replacing it with a highly reflective mirror. However, a higher Q-switching tendency was observed and could be avoided only within a narrow range of cavity parameters. This is attributed to changed laser and SESAM dynamics in consequence of the shorter repetition rate, and to the increased laser mode in the crystal and on the SESAM.
In general, I do not recommend Yb:CaF_2 as a gain medium for solid-state lasers due to its low absorption and emission cross-section. Other Yb-based gain media, such as Yb:KGW or Yb:CALGO provide a better stability. However, Yb:CaF_2 is a suitable medium for

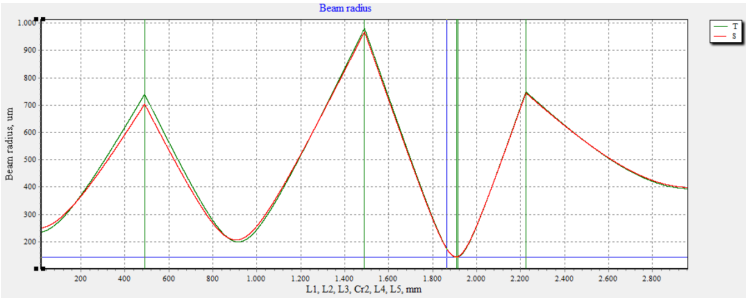

FIGURE 3.12. Caustic of the high power cavity design. The pump intensity is intended to be about 4 times higher compared to the previous design, thus allowing theoretically up to 64 W pump power. The cavity is intended to be operated at about 6 to 8 W output power, which is about a factor 2 higher than the reported power in this thesis. For stable mode-locking the a high fluence on the SESAM ($x = 0$ pos.) is required, according to the calculations to exceed the critical critical mode-locking energy.

ultrafast laser amplifiers, as it provides a high thermal conductivity, a high damage threshold and exhibits low dispersion. Promising results have been presented in [58–61].
It can be also implemented in thin-disk lasers, where Q-switching is avoided as the gain medium is passed m-times per round-trip. Thus the critical mode-locking energy decreases by $\frac{1}{m}$. The successful implementation is shown in [62, 63].

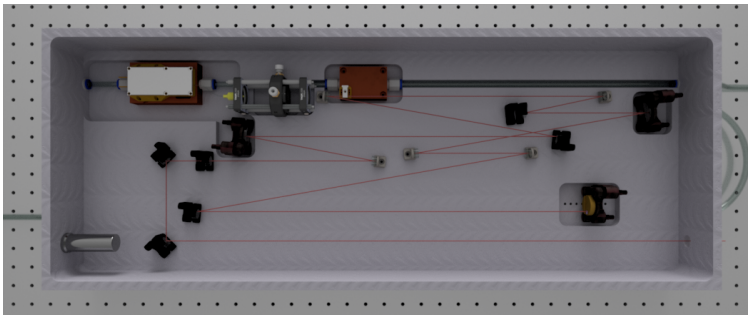

FIGURE 3.13. High power cavity optimized for robustness and stability. The cavity is built into a solid CNC-cut aluminum box. The cavity, pump diode and crystal are temperature stabilized using Peltier-elements and water cooling. Dry air purging can be applied.

4

FOURIER-TRANSFORM INFRARED SPECTROSCOPY NEAR THE DIFFRACTION LIMIT USING A BROADBAND FEMTOSECOND LASER

Material analysis on the low µm or even nm scale requires sophisticated spectroscopy techniques. Fourier-transform infrared (FTIR) spectroscopy is a well established spectroscopy technique but typically remains limited to large structures and relatively high sample concentrations. To push this limit, this chapter introduces a new mid-IR laser light source for commercial FTIR devices that allows for applications at µm spatial resolution, enables more than one order of higher sensitivity and thus significantly decreases measurement times from several hours to minutes. This chapter is mostly based on publication [64]:

F. Mörz, R. Semenyshyn, T. Steinle, F. Neubrech, U. Zschieschang, A. Steinmann, and H. Giessen, "Nearly diffraction limited FTIR mapping using an ultrastable broadband femtosecond laser tunable from 1.33 to 8 µm," *Optics Express* **25**, 32355-32363 (2017). Reprinted and adapted with permission. Copyright: 2017, Optical Society of America under the terms of the OSA Open Access Publishing Agreement

4.1 INTRODUCTION

FTIR spectroscopy allows to simultaneously measure a broad spectral region with a high optical throughput [5], high spectral accuracy [6], increased sensitivity and SNR [4] and at high speed compared to dispersive spectrometers. Commercial setups are equipped with a thermal light source, a so-called Globar, which emits incoherent but broadband radiation from about 1 to 20 µm. A typical spectrum is depicted in Fig. 4.1. Standard setups are frequently used to chemically characterize samples in many different fields, such as life sciences, quality control, drug testing or material science. However, sample sizes are typically limited to about 40×40 µm². At smaller areas the SNR and measurement sensitivity significantly drop and lead to unacceptable long integration times. This is due to the low beam quality and especially the low brilliance of the thermal light source, which is on the order of 10^{15} ph/s/mm²/sr/0 1%BW [38]. As shown in [38] and in this thesis, a laser exceeds this number by several orders of magnitude. Additionally, tighter focusing can be achieved with lasers in consequence of their excellent beam quality. These parameters are crucial for a further reduction of sample area, and increased sensitivity and measurement speed.
Commercially available laser sources for FTIR spectroscopy are quantum cascade laser (QCL) systems. However, they exhibit a narrow linewidth of about 1 cm^{-1} [10]. Thus, spectroscopy is associated with high effort as spectral sweeping and stitching is required. Laser sources with a more suitable bandwidth and a sufficient frequency tuning range include frequency combs and DFG schemes based on OPOs and OPAs. Here, we focus on the latter concept using a FFOPO for NIR frequency conversion. This allows for a passively stable system, which is easy to implement in standard FTIR spectroscopy.
The goal of this chapter is to enable chemical mapping with 10 µm spatial resolution with micro-FTIR spectroscopy [65] by applying a tunable mid-IR laser.

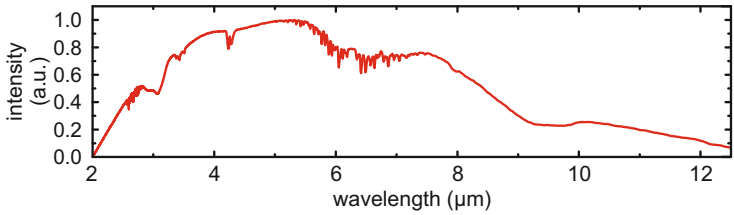

FIGURE 4.1. Typical spectrum of the utilized Globar measured with 4 cm^{-1} spectral resolution. The upper limit of 800 cm^{-1} (12.5 µm) is given by the transmission of utilized optics and the detector sensitivity.

4.2 EXPERIMENTAL SETUP

IR-active molecular vibrations serve as chemical identifiers for material analysis. They are mostly located in the range from 500 to 1500 cm^{-1} or 6.67 to 20 µm respectively, which is therefore denoted as the *fingerprint region*. Molecular resonances usually exhibit a bandwidth of a few cm^{-1} and, in order to chemically identify different materials, it might be necessary to investigate several molecular resonances. To avoid spectral sweeping, a light source with several 10 cm^{-1} bandwidth is desirable. Here, a parametric laser is presented, providing tunable mid-IR radiation with a bandwidth of 59 cm^{-1} at the FWHM or 100 cm^{-1} at the $1/e^2$-width, respectively. A schematic illustration of the applied laser setup is depicted in Fig. 4.2. A commercial pump oscillator from *Montfort Laser GmbH* is applied, providing up to 3 W output power at 1047.88 nm central wavelength and 12.92 nm spectral bandwidth (FWHM). During the experiments the laser crystal and SESAM have been damaged and exchanged. After realignment the laser exhibits a bandwidth of 9.4 nm FWHM (86 cm^{-1}) at a central wavelength of 1044.9 nm as depicted in Fig. 4.3a). A pulse duration of 200 fs (Fig. 4.3b)) is measured after propagation through a Faraday isolator (*E.O.T.*). This oscillator is used to pump a multi-stage parametric frequency conversion setup to reach the mid-IR frequency range. It is based on [12], where we demonstrated a tuning range from 500 to 7519 cm^{-1},

with up to 100 mW output power. However, in [12] the bandwidth was limited to about 26 cm^{-1} FWHM, as the main oscillator provided 450 fs-long pulses.

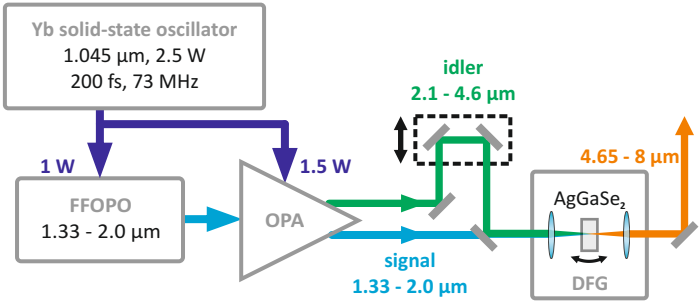

FIGURE 4.2. Schematic laser setup. The system is pumped by an Yb-based solid-state oscillator emitting about 200 fs pulses at 73 MHz. Signal and idler beams, which are tunable from 1.33 to 2.0 µm and 2.1 to 4.6 µm are generated in an amplified FFOPO. They are combined in a 2 mm-long $AgGaSe_2$ crystal to generate their difference frequency. The DFG beam is tunable from 4.65 to 8 µm, being limited by the low pump power. Figure adapted from [64].

Similar to [12] a FFOPO is used to initially convert the pump oscillator to the NIR range from about 1.33 to 2 µm. An OPA is then used to amplify the OPO output and generate an idler beam, which is tunable from 2.1 to 4.9 µm. The utilization of a post-amplified FFOPO enables a passively long-term stable input for a subsequent DFG. In contrast to a bulk free-space OPO, a large part of the cavity is transferred into a single-mode fiber in a FFOPO. Thus, a slight pulse broadening of the oscillating OPO signal pulse is achieved, which crucially enhances the temporal overlap stability with the OPO pump pulse. Thus an excellent long-term stability is achieved. Furthermore, as the single-mode fiber is the largest part of the FFOPO cavity, a very compact setup with only few free-space optical elements is created and the OPO becomes very insensitive

regarding ambient conditions. By amplifying the FFOPO output an excellent peak-to-peak stability and low RMS noise is achieved. Typically, the FFOPO is operated at low (pump) power and is used to provide a wavelength and power stable amplifier seed. The high OPA single pass gain is then used to generate high power signal and idler beams efficiently. More details can be found in [29, 30].

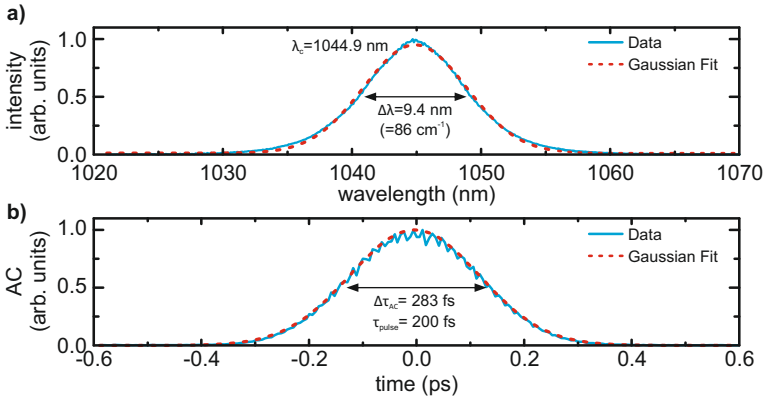

FIGURE 4.3. **a)** Spectrum of the utilized *Montfort M-FEMTO*. A bandwidth of 9.4 nm, which corresponds to 86 cm^{-1}, at a central wavelength of 1044.9 nm is measured. The corresponding autocorrelation is shown in **b)**. A pulse duration of 200 fs is measured after propagation through a Faraday isolator.

The achieved post-amplified FFOPO signal tuning range and signal and idler power are depicted in Fig. 4.4a). Between 100 to 350 mW signal power is generated from 1.4 to 1.8 µm. The idler power reaches maximum 102 mW at 1.55 µm. The corresponding autocorrelation traces are given in Fig. 4.4b). At wavelengths of high gain and power short pulses between 130 and 200 fs are measured. At wavelengths that suffer from atmospheric absorption or that are at the tuning range edges longer pulses are measured.

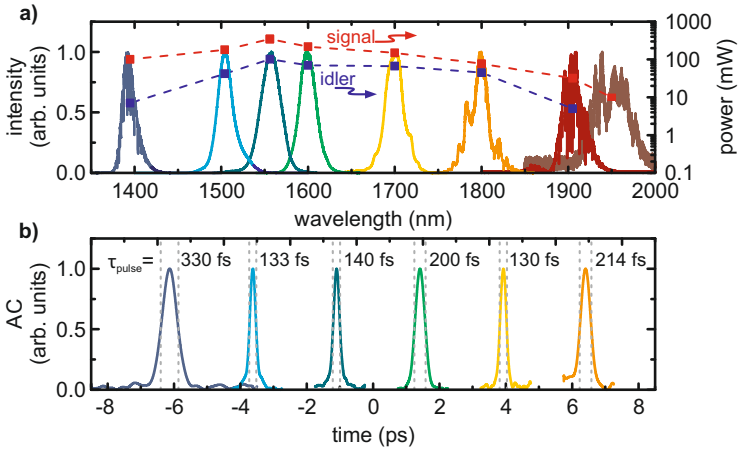

FIGURE 4.4. **a)** Signal tuning range and signal (red) and idler (blue) power. Up to 350 mW signal and 100 mW idler power is generated. **b)** Corresponding autocorrelation of the signal beam, assuming $sech^2$-pulses. Short pulses are generated at regions of high gain and power. At the tuning range edges and at wavelengths that suffer from atmospheric absorption longer pulse durations are measured. No autocorrelation is measured at 1.8 µm and higher, as the signal power was too low.

A summary of the pump laser and amplified FFOPO pulse characteristics is given in Table 4.1. In general, nearly Fourier-limited pulses are achieved, except at the tuning range edges.

The OPA signal and idler beams are spatially and temporally combined in a 2-mm-long AR-coated $AgGaSe_2$ crystal to generate their difference frequency. The resulting DFG beam is tunable from 4.65 to 8 µm wavelength (1250 to 2150 cm^{-1}), with a maximum output power of 2.65 mW at 5.5 µm wavelength (1818 cm^{-1}). At the tuning range edges about 0.2 mW power is measured, which is still sufficient for FTIR measurements. Fig. 4.5 shows the DFG tuning range and output power. The output power is measured after the beam delivery path to the FTIR, which means the given values denote the applicable power. The limited tuning range and relatively low power compared to previously presented setups is

Wavelength (nm)	FWHM (nm)	FWHM (cm^{-1})	pulse duration (τ_p) (fs)	TBP
1045	9.40	86.08	200	0.52
1395	17.58	90.34	330	0.89
1504	21.94	96.99	133	0.39
1556	27.01	111.56	140	0.47
1600	22.96	89.69	200	0.54
1700	24.66	85.33	130	0.33
1800	26.29	81.14	214	0.52
1905	28.93	79.72	-	-
1950	48.43	127.36	-	-

TABLE 4.1. Measured bandwidth and pulse duration of the pump laser (first row) and the amplified FFOPO utilized as DFG input. Nearly Fourier-limited pulses are achieved, except at the tuning range edges of the FFOPO.

due to the low pump power of the main oscillator. By increasing the available pump power to about 8 W, an extended tuning range and higher output power are expected. This is investigated in [66] in order to further optimize the laser source. Here, a *Light Conversion FLINT* laser, providing 123 fs-long pulses at an output power of 8 W is used for pumping the frequency conversion scheme. Thus, a DFG tuning range from 2000 to 909 cm^{-1} (5 to 11 µm) is presented, reaching a mean bandwidth ($1/e_2$) of more than 170 cm^{-1}. The lower frequency limit is given by the utilized OPO and OPA crystals (PPLT) and the short pump laser wavelength (1030 nm).

The spectra depicted in Fig. 4.5 exhibit a mean bandwidth of 59 cm^{-1} FWHM, or 100 cm^{-1} at the $1/e^2$-width. An exemplary measurement is depicted in Fig. 4.6a). To increase the measurement stability and robustness, the laser system is built on a single water cooled breadboard and installed into a solid box to avoid air flow. The system exhibits fluctuations of the central wavelength

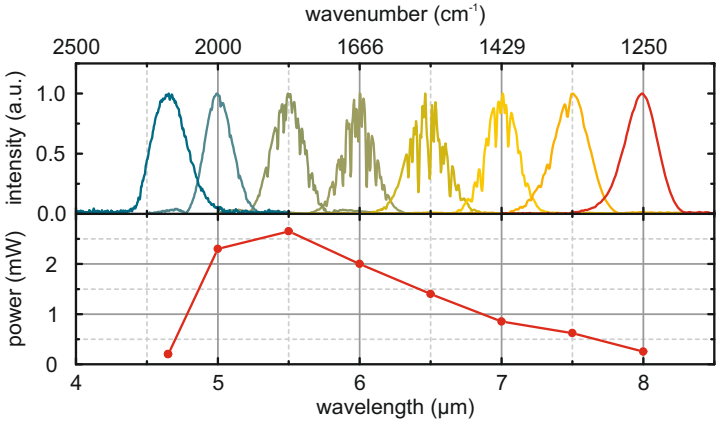

FIGURE 4.5. Mid-IR tuning range and output power (lower panel). The depicted power is measured at the FTIR input, i.e. after propagation through the beam delivery path. Between 0.2 mW power at the tuning range edges and 2.65 mW at 5.5 µm (1818 cm^{-1}) can be applied within the experimentally accessible range from 4.65 to 8 µm (1250 to 2150 cm^{-1}). Figure adapted from [64].

as small as 0.013 %RMS, measured at 7 µm (1429 cm^{-1}). The bandwidth fluctuates by just 0.61 %RMS, mainly affected by atmospheric absorption, as depicted in Fig. 4.6b). For FTIR measurements, nitrogen flushing of the light source and spectrometer is therefore recommended.

Special attention is paid to the beam delivery path from the laser to the FTIR for several reasons. First, the DFG laser setup requires angular phase-matching. This means that the nonlinear crystal orientation relative to the optical axis needs to be adjusted during wavelength tuning. Due to the large refractive index of $AgGaSe_2$ ($n = 2.58$) several 10°-crystal rotation are required to cover the full tuning range. In consequence, the DFG output beam experiences a crystal-orientation-dependent beam offset, which needs to be compensated during wavelength tuning in order to maintain coupling to the FTIR. More details are given in Chapter 6.

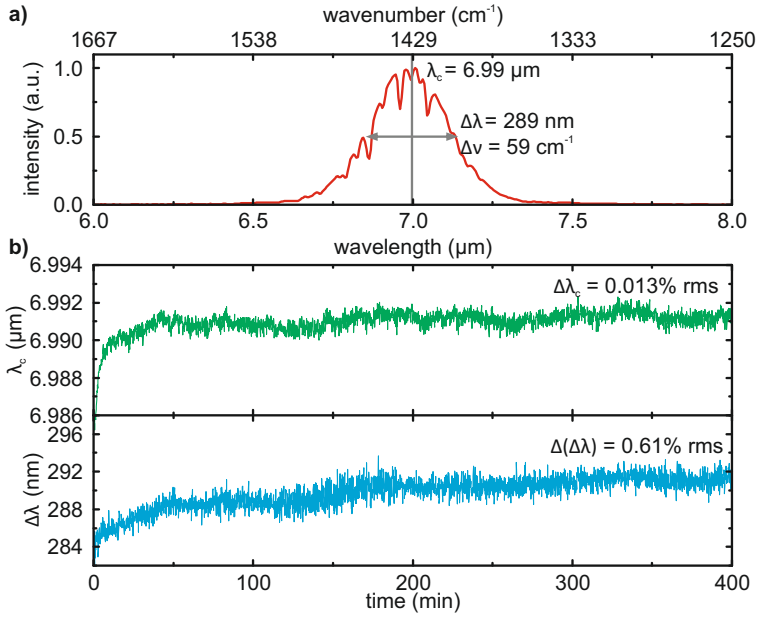

FIGURE 4.6. Measurement of the light source stability at 7 µm wavelength (**a**)). A bandwidth of 289 nm (59 cm^{-1}) is measured. **b)** Spectral stability measured over 400 min. The central frequency shows fluctuations of 0.013 %RMS, whereas the bandwidth fluctuates by 0.61 %RMS. No nitrogen flushing is applied during these measurements.

Second, the FTIR spectrometer, as well as the attached microscope are designed for a thermal light source. An external light source needs to be mode-matched on this optical design to achieve a high throughput. A 1:1 telescope is inserted into the beam delivery path for this purpose and optimized for maximum incoupling by adjusting the beam divergence. Ideally, reflective optics are used in order to avoid chromatic aberrations. However, we are currently using CaF_2 lenses in consequence of limited space. In a future setup, a design similar to [35] is recommended.

To conduct spatially resolved FTIR measurements a *Bruker Hyperion* 2000 microscope is attached to the spectrometer (*Bruker Vertex* 80). The microscope is used in transmission mode and

the IR beam is focused and collimated by using a 36x objective and condenser. The signal is detected by a liquid-nitrogen-cooled Mercury-Cadmium-Telluride (MCT D313) detector, providing a measurement range from 850 to 12 000 cm^{-1} and a sensitivity of $D^* > 4 \times 10^{10}$ $cmHz^{1/2}W^{-1}$. A detailed view on the setup is depicted in Fig. 4.7.
The investigated sample area is defined by adjusting the aperture in front of the MCT detector (Fig. 4.7), as described in Section 2.6, to 10×10 µm².

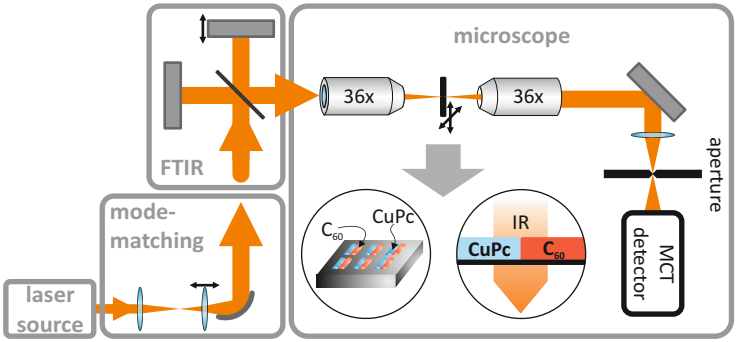

FIGURE 4.7. Schematic illustration of the micro-FTIR setup using a *Bruker Vertex* 80 spectrometer and *Bruker Hyperion* 2000 microscope. Before coupling the laser source into the device via the backwards input, the laser beam is mode-matched to the optical design of the spectrometer. A 36x objective and condenser are used for beam focusing and collimation. Thus, an aperture size of 10×10 µm² is feasible. The signal is measured with a liquid nitrogen cooled detector. Figure adapted from [64].

4.3 RESULTS

The goal of this work is to enable MIR chemical mapping at µm spatial resolution within reasonable time scales using FTIR spectroscopy. The investigated sample consists of several 100 nm-thick copper phtalocyanine (CuPc) and C_{60} layers. They are evaporated on a CaF_2 substrate by using stencil masks. CuPc exhibits a distinct molecular vibration at 1421 cm^{-1}, whereas C_{60} exhibits a resonance at 1429 cm^{-1}, as depicted in Fig. 4.8. These spectra are recorded with the thermal FTIR light source using highly concentrated samples. A 15x condenser and objective and an aperture size of 100×100 $µm^2$ are used for this characterization. 200 spectra with a spectral resolution of 4 cm^{-1} are averaged.
The laser is tuned to 1430 cm^{-1} in order to detect both the CuPc and C_{60} resonance with comparable light intensity. A 150×150 $µm^2$ area is mapped in steps of 10 µm with a spectral resolution of 2 cm^{-1}. On each pixel 15 *signal spectra* are recorded and averaged, resulting in 143 s/px integration time. A signal spectrum consists of a measurement at the sample position divided by a background position measurement. Sample and background spectra are measured alternating to account for mechanical drifts of the measurement setup, as well as spectral and power drifts of the light source. The impact of such drifts is discussed more detailed in Section 2.1 and [29].

After mapping the sample, each signal spectrum is evaluated within the FWHM of the laser spectrum. After a linear baseline correction the peak absorption of the respective resonance is determined, whereby a threshold of 0.25 % minimum absorption is applied. Fig. 4.9 depicts the evaluated maps, as well as a reference microscope image of the measured sample area (Fig. 4.9a)). On the microscope image CuPc appears blueish, whereas C_{60} is visible in a reddish color. The chemical analysis of this sample area is shown in Fig. 4.9b), which is in very good agreement with the microscope image. For simplicity, the same color code is used. Fig. 4.9c,d) show

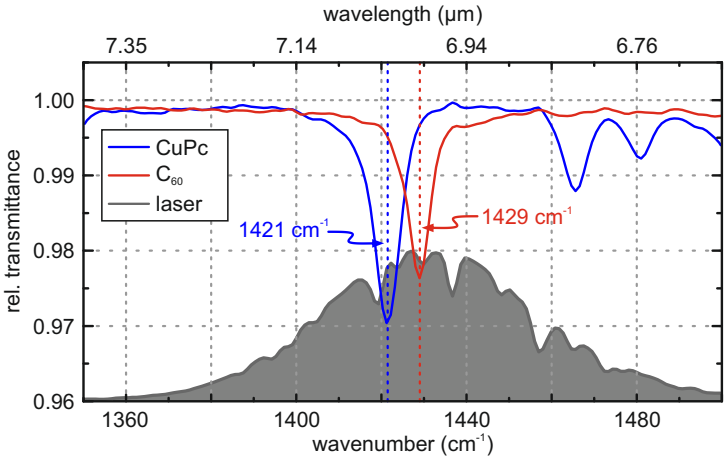

FIGURE 4.8. Molecular resonances of CuPc and C_{60} solutions. This characterization is measured with the Globar using 100×100 µm² aperture size and 4 cm^{-1} spectral resolution. 200 spectra are averaged, respectively. Below, a laser spectrum is shown as it is used during the mapping. The laser is tuned to 1430 cm^{-1}, thus covering both molecular resonances simultaneously at reasonable intensity. Figure adapted from [64].

the separated images of CuPc and C_{60}. Such separate information is not accessible using the microscope image and a significant benefit of chemical imaging.

The layer edges appear smeared out in comparison to the microscope image. Some layers also appear connected. The signal strength of these features is on the order of 0.4 % or higher, therefore measurement artifacts seem to be unlikely. We attribute these features to the evaporation process of the individual layers, during which some material might have leaked underneath the stencil masks. This information is feasible in consequence of the high sensitivity using a MIR laser. It highlights the potential for applications, such as quality control, or can improve the SNR and measurement speed in already existing FTIR setups. Still, a higher spatial resolution is required in our case, as the smeared out features probably appear too large on the map.

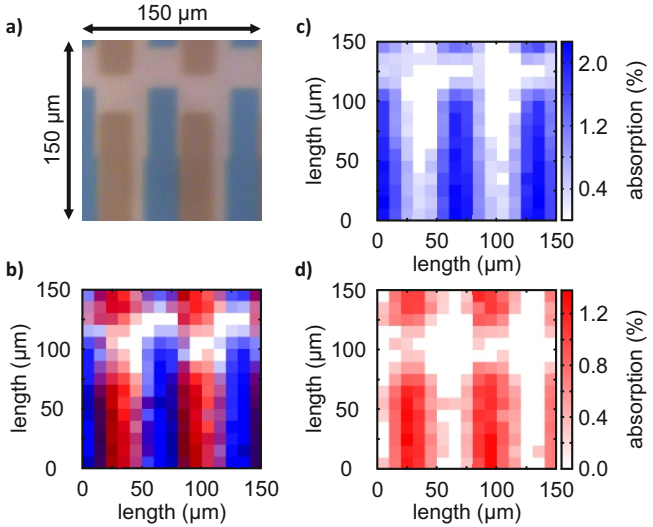

FIGURE 4.9. FTIR mapping applying the laser. **a)** Microscope reference image. The 100 nm-thick CuPc layer appears blue, C_{60} layers appear red. **b)** Chemical image applying 0.7 mW laser power at 1430 cm^{-1}. Each pixel ($10\times10\,\mu m^2$) is measured with 2 cm^{-1} spectral resolution and 143 s/px integration time. **c,d)** Extracted signal intensity of CuPc (1421 cm^{-1}) and C_{60} (1429 cm^{-1}). The laser mapping shows tiny signals distributed around the actual layer, which are not detected with the microscope. These signals are due to the sample preparation process, during which material is leaks below the sample mask. Figure adapted from [64].

Comparison to Globar

In the following the previously presented experiment is repeated using the internal FTIR light source (Globar). Fig. 4.10a) depicts the resulting maps after 8 h56 min total measurement time (t_{int} = 143 s/px). This is identical to the laser-based measurements shown in Fig. 4.9. However, no signal is detected using the Globar. This is attributed to its low brilliance and large beam waist.
In contrast to this, Fig. 4.10b) shows maps at a minimum integration time of 29 s/px measured with the laser. Due to the slightly

increased noise level, a signal threshold of 0.5 % is set during the evaluation. A reasonable SNR is achieved despite a 5-times shorter measurement time (t_{tot} = 109 min). Thus, by applying the laser source for FTIR mapping a scanning speed of 3.5 µm/s can be reached.

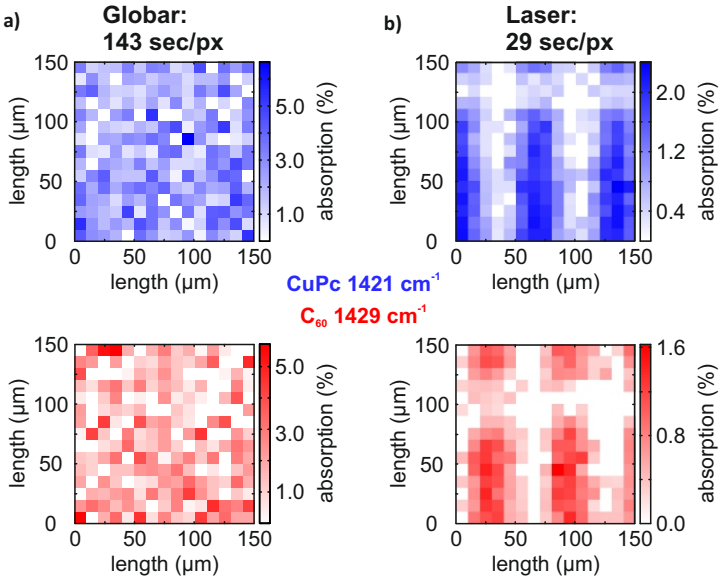

FIGURE 4.10. Mapping conducted with the Globar (**a)**) and the laser (**b)**) at minimum integration time. Despite 143 s/px integration time (t_{tot} = 8.9 h) no signal is detected with the Globar due to its low brilliance and large beam waist. In contrast, the laser allows for a reasonable SNR using a 5-times shorter measurement time (t_{tot} = 1.8 h). A scanning speed as short as 3.5 µm/s is reached. Figure adapted from [64].

Fig. 4.11 depicts raw spectra that are chosen from random pixels of the measured images. The CuPc resonance is plotted in the top row, whereas C_{60} spectra are displayed in the bottom row. The strong CuPc resonance at 1421 cm^{-1} is nicely visible using the

laser light source with minor differences between long (143 s/px) and short (29 s/px) integration time. At the weaker C_{60} resonance (1429 cm^{-1}) the signal and noise level are comparable defining the minimum integration time.
In contrast, the Globar spectra exhibit a significantly higher noise level, exceeding the molecular signals. This is attributed to the about 4-orders of magnitude lower brilliance of the Globar, as well as to a larger spot size compared to the laser. The Globar intensity decreases to about 11 % if the aperture is decreased from 40×40 µm² to 10×10 µm². In other words, the incident amount of photons at the detector is not sufficient to exceed the intrinsic detection noise.

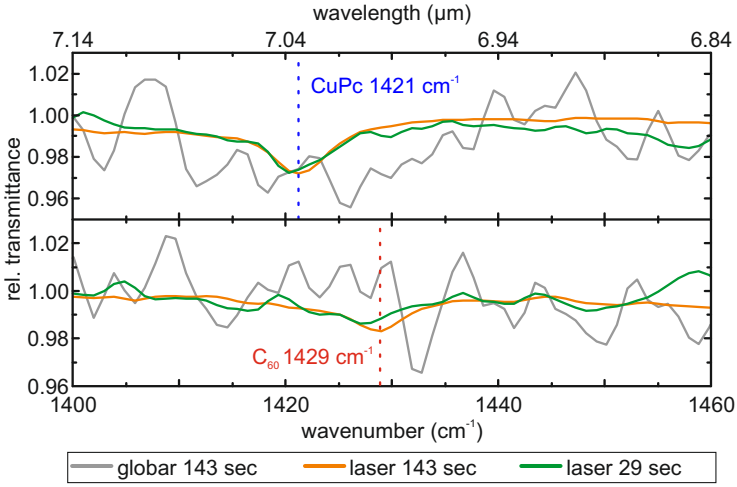

FIGURE 4.11. Raw FTIR spectra of arbitrarily chosen pixels of CuPc (top row) and C_{60} (bottom row). Globar measurements are depicted in grey, the laser is depicted in red for t_{int} = 143 s/px and in green for t_{int} = 29 s/px. High noise exceeds any molecular signal in the Globar spectra, whereas distinct resonances are detected with the laser. Figure adapted from [64].

This is further investigated by evaluating the accessible sensitivity and RMS noise of the laser and the Globar based on the previously acquired data. For that purpose, consecutive *background* spectra are divided to derive 100 %-lines. The RMS noise is calculated within the FWHM laser bandwidth (1400 to 1460 cm^{-1}) for both light sources. It is depicted in Fig. 4.12 for a total measurement time of 400 min. The mean noise level of the Globar reaches 6.41 %RMS, compared to 0.47 %RMS laser noise. These numbers depict the mean fluctuations of a single signal spectrum. Therefore they also give the minimum measurement sensitivity, assuming a SNR of 1. Thus, absorptive signals as small as 0.47 % can be detected single shot with the laser light source, whereas a more than 13-times higher signal strength is required if the Globar is used. For that reason, no successful mapping was possible applying the Globar.

SNR at different aperture sizes

At last, the measurement noise is investigated in dependence of the aperture size, i.e. the detected sample area. A sample with concentrated C_{60} is used for this purpose and investigated in the region from 1585 to 1700 cm^{-1}, as two distinct spectral features are visible here. The sample is measured using aperture sizes of 40×40 μm^2, 20×20 μm^2 and 10×10 μm^2. The integration time is increased from 1 min to 10 min. Fig. 4.13 depicts the measured data. The Globar is plotted in a grey linecolor, the laser light source is depicted in red. As visible, both light sources enable comparable results (SNR) at 40×40 μm^2 aperture size. However, they significantly differ if the aperture is reduced. Whereas the laser SNR remains nearly constant if the aperture is decreased, the Globar noise increases to several %RMS. This matches the previous observations of the mapping experiments. This experiment also indicates a large Globar beam waist compared to the laser. Indeed, the measured intensity drops by 89 % from the largest to the smallest aperture. In contrast,

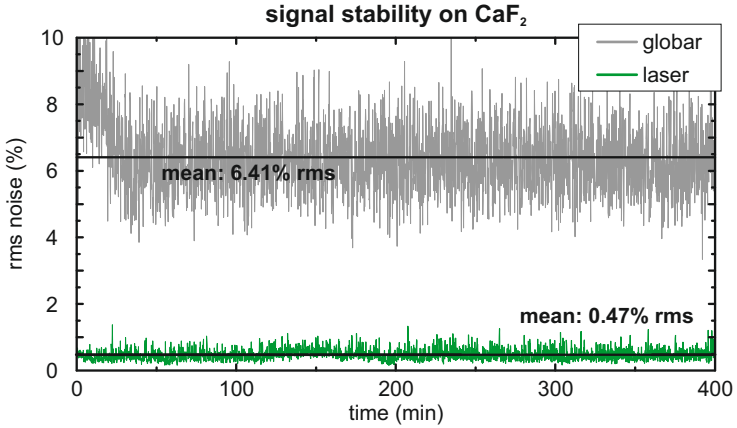

FIGURE 4.12. Laser and Globar RMS noise in the range from 1400 to 1460 cm^{-1} (laser FWHM). The mean Globar noise level reaches 6.41 %RMS, which is more than one order magnitude higher than the laser noise (0.47 %RMS). This measure describes the intrinsic noise originating from the light sources. It also defines the measurement sensitivity assuming a SNR of 1, i.e. absorptive signals as small as 0.47 % can be detected with a single laser measurement. Figure adapted from [64].

45 % laser intensity loss is measured. Thus, the laser reaches a significantly higher intensity on the sample and at the detector. This not only allows for a higher signal excitation but also for lower noise as the intrinsic detection noise is exceeded.

4.4 CONCLUSION

In conclusion a tunable MIR laser was introduced for micro-FTIR spectroscopy. It allows for enhanced sensitivity and enables fast chemical analysis at few µm spatial resolution. The laser design provides a passive long-term stability, which is crucial for FTIR spectroscopy, over the entire tuning range from 1250 to 7500 cm^{-1} (1.33 to 8 m). It exhibits 100 cm^{-1} bandwidth ($1/e^2$), which is more

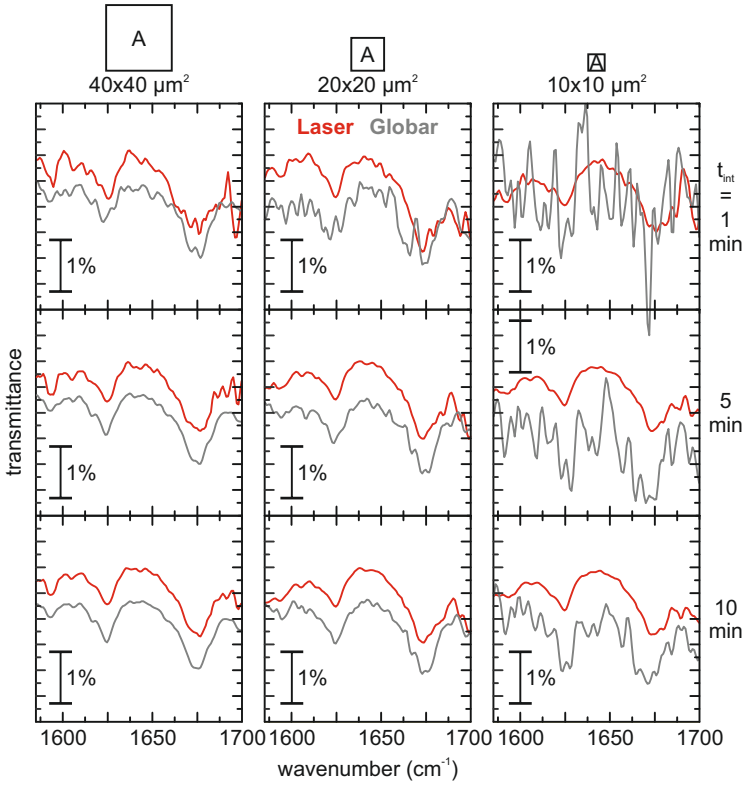

FIGURE 4.13. Signal spectra of concentrated C_{60} using different apertures between 40×40 µm² and 10×10 µm². The integration time increases from 1 min to 10 min. The laser is plotted in red, whereas the Globar appears in a grey linecolor. At the largest aperture similar results are obtained with both light sources. However, the Globar RMS noise significantly increases at smaller apertures. In contrast, a nearly constant SNR is observed using the laser. The detected Globar intensity drops by 89 % from 40×40 µm² to 10×10 µm² aperture size. In contrast to 45 % using the laser. This indicates a larger Globar beam waist and thus significantly lower intensity at the sample and detector.

than sufficient to detect molecular vibrations and avoids spectral sweeping and stitching. Compared to a Globar the system provides

a 13-times higher sensitivity, which enables a measurement time reduction by a factor 5. Thus, acceptable measurement times are in reach.
By using a pump oscillator with higher average power, the accessible tuning range and MIR power can be further increased. Due to the higher intensity, a further measurement time reduction is expected, as the SNR can be increased. With further advances regarding illumination geometry and detection, this system system can enable video rate spectroscopy and eventually even sub-µm spatial resolution.

5

IN-VITRO DETECTION OF POLYPEPTIDE CONFORMATIONS AT ATTOMOLAR CONCENTRATION

Infrared spectroscopy is a highly promising technique to investigate changes of the secondary protein structure. Such changes are associated with many human diseases, such as Alzheimers or Huntingtons disease. However, in order to understand these processes it is of major importance to in-vitro investigate a minimum amount of proteins, ideally a single protein, and their reaction to external stimuli. Monitoring such dynamic processes requires fast and highly sensitive measurement techniques. FTIR microspectroscopy is a promising candidate, but still requires several hundreds of thousands of molecules and hour-long integration times in current state-of-the-art experiments. This limit is given by the typically used thermal light sources, exhibiting a low brilliance. In the following, the in-vitro determination of polypeptide structures in less than 10 min is presented. By employing the MIR laser setup presented in Chapter 4 different conformational structures are distinguished at attomolar concentrations, which is about 100 times lower than previously shown. For comparison, measurements are conducted using the standard thermal FTIR light source, as well as a synchrotron light source. Due to the high sensitivity, short measurement time and tabletop size, the presented system can enable research on a daily basis. With further advances, the ultimate limit of detecting only a few or even a single protein in aqueous environment and investigate the conformational behavior can become possible.

This work has been carried out in close cooperation with Dr. Rostyslav Semenyshyn. Complementary details regarding sample preparation, functionalization and FTIR spectroscopy can be found in [67]. Parts of this chapter have been published in [68], with equal contribution from Dr. Rostyslav Semenyshyn and me.

R. Semenyshyn, F. Mörz, T. Steinle, M. Ubl, M. Hentschel, F. Neubrech, and H. Giessen, "Pushing down the Limit: In Vitro detection of a Polypeptide Monolayer on a Single Infrared Resonant Nanoantenna," *ACS Photonics* **6**, 2636-2642 (2019). Reprinted and adapted with permission. Copyright: 2019, American Chemical Society

5.1 INTRODUCTION

In the modern world, the number of people suffering from neurodegenerative diseases is growing, in consequence of an increased life expectancy and the modern world lifestyle. These diseases are considered to be associated with protein folding, during which proteins end up in a pathological state [69]. Until now, there is no successful treatment to stop or even revert these processes. In recent years there have been significant advances in detecting and monitoring structural protein changes by using FTIR micro-spectroscopy. In [70], the transition from a so-called β-sheet state to a disordered state has been monitored in-vitro, whereas in [71] the authors reported the reversible switching between the α-helical and β-sheet states in in-vitro conditions. However, both experiments required high polypeptide concentrations being limited by the measurement sensitivity resulting from the utilized thermal light source. Another promising approach was presented in [72], where s-SNOM [73–75] was employed, which allows for the detection of single protein complexes due to a spatial resolution on the nm-scale [75–78]. However, in-vitro measurement are not feasible with this technique at the current state-of-the-art, although first efforts are made.

Therefore a decision between investigating single protein complexes and in-vitro micro-FTIR measurements at high concentrations needs to be made. The goal of this work is to enhance the sensitivity, SNR and spatial resolution of micro-FTIR spectroscopy to push the in-vitro detection to minimum protein concentrations and narrow the gap between near- and far-field techniques.
As shown in the previous chapter, MIR lasers allow for a significant sensitivity increase in consequence of their high brilliance, beam quality and coherence. In [40] an intra-pulse difference frequency generation scheme was presented, which exhibits a bandwidth ranging from 833 to 2500 cm^{-1} (4 to 12 µm) and reaches a brilliance comparable to synchrotron light sources at 1000 cm^{-1}. However, its brilliance remains below the synchrotron brilliance at other frequencies, thus limiting its applicability. Therefore, we focus on our system presented in Chapter 4, which exceeds the synchrotron brilliance [79, 80] over its entire tuning range. At 1630 cm^{-1} the system reaches a brilliance on the order of 10^{19} ph/s/mm²/sr/0.1%BW as depicted in Fig. 5.2. Above all, it reaches passive excellent long-term stability and exhibits a small footprint.
To provide an ultrasensitive platform that allows for the detection of few proteins with dimensions below the diffraction limit at the nm-scale, we use a combination of laser-based FTIR spectroscopy and SEIRA [41]. Vibrational signals can be enhanced by several orders of magnitude, as described in Section 2.7.
In contrast to [70, 71] only a single gold nanoantenna is used to plasmonically enhance the molecular signal. This enables a concentration reduction of more than 2-orders of magnitude to about 1600 polypeptides. The number of detected polypeptides is derived from the light-confinement and molecule volumes.
In this chapter the in-vitro detection of polypeptide conformations at attomolar concentrations using laser-based FTIR spectroscopy is presented. Control experiments are performed with thermal (Globar) and synchrotron light sources, which are the common workhorses in FTIR spectroscopy. The experimental procedure is depicted in Fig. 5.1.

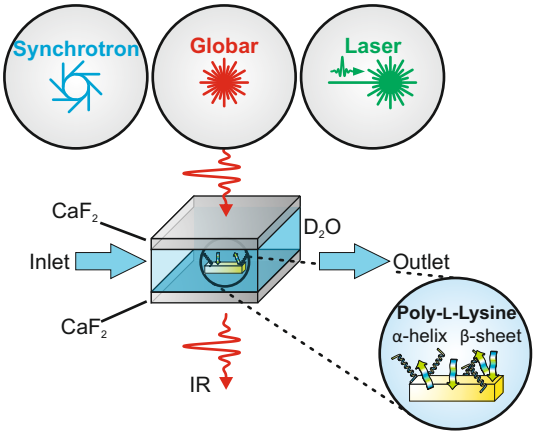

FIGURE 5.1. The secondary structure of poly-L-lysine is investigated using FTIR micro-spectroscopy. Attomolar concentrations at the nm-scale are detected by means of SEIRA. The resonant single gold nanoantenna, covered with polypeptides, is measured in living environment. We employ a Globar, synchrotron, and our broadband, tunable MIR laser, and compare the results in terms of accessible sensitivity, measurement time and footprint. This figure is adapted from [68].

5.2 EXPERIMENTAL PROCEDURE

The measurement setup is similar to the setup discussed in Chapter 4. The microscope aperture size is set to $10{\times}10\,\mu m^2$ and all spectra are recorded with a spectral resolution of $4\,cm^{-1}$. Each FTIR spectrum is accumulated for approximately 14.7 s. This includes 10 scans each on the background and sample position. The background position is located on the CaF_2 substrate far from the antenna. To account for both mechanical and spectral drifts the background and sample position are recorded alternating for each FTIR spectrum. Details about the synchrotron setup are given in [81].

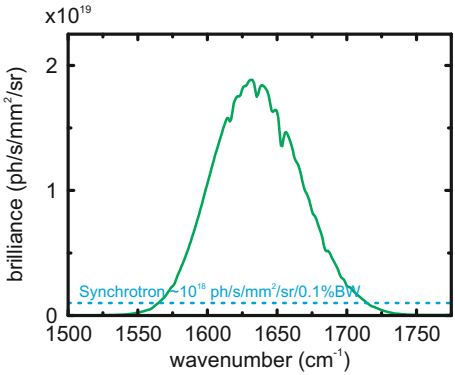

FIGURE 5.2. Spectral brilliance of the laser, which reaches up to 10^{19} ph/s/mm²/sr at 1630 cm^{-1} using an average power of 1.8 mW. The blue short-dashed line depicts the brilliance of a synchrotron, reaching 10^{18} ph/s/mm²/sr/0 1%BW, as described in [79, 80]. The Globar brilliance is on the order of 10^{15} ph/s/mm²/sr/0.1%BW (not shown)[38].

To conduct in-vitro measurements a flow-cell has been designed, which allows to control the liquid environment and to measure in transmission. The cell consists of two CaF_2 substrates, with a 1 µm-thick SiO_2 buffer layer in between. A cylindrical recess is etched centrally into the SiO_2 layer to form a sample compartment. A detailed view is shown in Fig. 5.3. As illustrated, the upper CaF_2-substrate contains an inlet and outlet to control the liquid environment. First, pure D_2O is utilized. Later, sodium-dodecylsulfate (SDS) is added in order to introduce protein folding.

Several antennas of 100 nm width and height are written onto the lower CaF_2 substrate. They vary in length (1.7 to 1.9 µm) to ensure optimum matching to the molecular resonance. The antennas are sufficiently separated to avoid interaction. For now, we use an antenna geometry similar to [70, 71, 82], where large antenna arrays have been used, for referencing our measurements. However, there might be room for optimization of the antenna design for laser light illumination, as the overlap with the laser intensity profile might not be ideal in the current state. This is beyond the

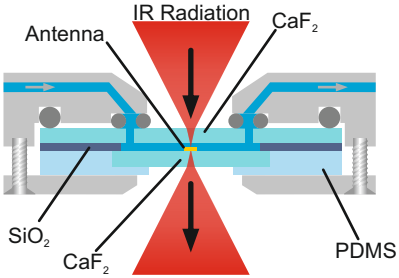

FIGURE 5.3. Schematic drawing of the utilized flow cell for in-vitro measurements. It consists of two CaF_2 substrates, which are separated by a 1 µm-thick SiO_2 buffer layer, to allow for transmission measurements. A cylindrical recess of 7 mm diameter is etched into the buffer layer to form a sample compartment. The cell contains an inlet and outlet to control the liquid environment. First, pure D_2O is utilized, later sodium dodecyl sulfate (SDS) is added. Figure adapted from [68].

scope of this work, but should be investigated in the future.
Poly-L-lysine is used as a model system for protein structure analysis. We monitor the amide-I vibration to investigate structural transitions. Its resonance frequency and line-shape change, as intramolecular bonds are rearranged during structural changes. Two different conformations can be distinguished in the present experiments. The α-helical state is located at 1648 cm^{-1}, whereas the β-sheet state resonance is found at 1618 cm^{-1}. Fig. 5.4a) depicts both resonance peaks measured in a saturated PLL solution.

To adsorb the polypeptides to the antenna a binding layer consisting of MUA/MUoL is required. As PLL only binds to MUA, the ratio of MUA/MUoL allows to control the spacing between the polypeptides, which is crucial to enable structural changes. An illustration is depicted in Fig. 5.4b). The functionalization is conducted in neutral environment to avoid a preferred structure. Thus, both α-helix and β-sheet should be distributed equally. Later, SDS is added to the D_2O environment to fold the polypeptides into the β-sheet state [85–87]. The functionalization recipe is taken from

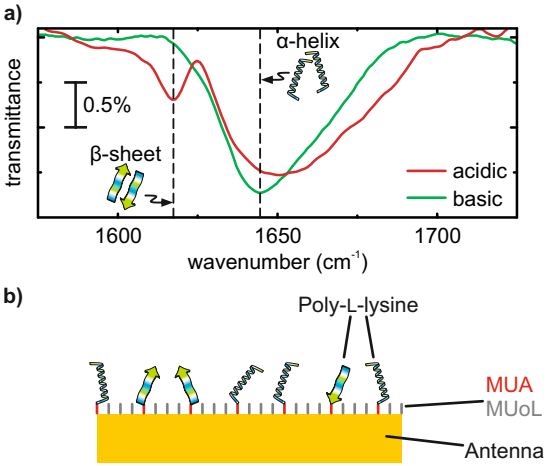

FIGURE 5.4. **a)** Characterization of a poly-L-lysine (PLL) solution using the Globar source. The amide-I vibration is monitored. If the polypeptides are in the α-helical structure, the central resonance frequency is found at 1648 cm^{-1}. If PLL folds into the β-sheet state the resonance shifts to 1618 cm^{-1}. **b)** Adsorption of PLL molecules on a gold nanoantenna. A layer of 11-mercaptoundecanoic acid (MUA)/11-mercaptoundecanol (MUoL) is used as a binding layer. By adjusting the MUA/MUoL ratio the spacing between neighboring PLL molecules is controlled, as the molecules only bind to MUA. This is required to allow for folding. More information can be found in [67, 71, 83, 84]. Figure adapted from [68].

literature [83] and has been refined in previous experiments [71, 84].

Sample localization

In order to detect the nanoantenna, careful alignment of the sample is required. The antenna needs to be positioned in the center of the microscope aperture, i.e. laser beam, to avoid distortions due to the illumination geometry [32].
Initially, the sample is coarsely aligned by means of orientation

markers using the microscope bright-field mode. Then a 20×20 µm² area is mapped in steps of 2 µm at 32 cm^{-1} spectral resolution. 50 spectra are averaged per pixel. The position of maximum plasmonic signal amplitude is defined as the coarse measurement position. Finally, the position is optimized by switching to 4 cm^{-1} spectral resolution. This procedure is carried out similarly for all light sources. In our lab, the Globar is used for characterizing the plasmonic resonance prior to the laser measurements.

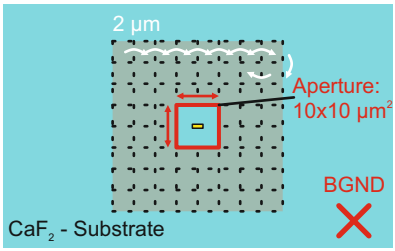

FIGURE 5.5. Alignment of the nanoantenna sample. After a coarse alignment using markers, an area of 20×20 µm² is mapped at 10×10 µm² aperture size in steps of 2 µm at a spectral resolution of 32 cm^{-1}. 50 spectra are averaged per pixel. The position of maximum plasmonic signal amplitude is finally optimized by another more precise mapping using 4 cm^{-1} spectral resolution.
The background position (BGND) is located on the bare CaF_2 substrate, sufficiently separated from the sample position. Figure adapted from [68].

Data analysis

To quantitatively compare the different light sources, the RMS noise and the SNR are calculated. From these values the sensitivity and the detection limit can be derived, as described in Section 2.6. Here, the RMS noise is calculated based on the recorded background

spectra. Subsequent background spectra are divided to derive 100 % lines. To avoid correlation effects, which would decrease the RMS noise, background spectra are used in pairs of two, i.e. the first and second spectrum, the third and fourth, and so on. Therefore, based on the measurement time of a single signal spectrum, an integration time of 10 min requires 84 background spectra (i.e. 42 signal spectra).
The SNR is calculated according to Eq. (2.56). The signal amplitude A_{signal} is derived by fitting the antenna profile using a Lorentzian function, which is used for a baseline correction. The Lorentzian fitting is carried out in several steps. First, the antenna spectrum measured with the Globar is fitted to derive the resonance frequency and the product of resonance width and modulation depth. As already mentioned, the antenna resonance slightly changes, if it is measured with the laser due to a slightly different illumination geometry [32]. The resonance measured with the laser might appear narrower and exhibit a deeper modulation depth. However, the product of resonance width and modulation depth remains constant, as the oscillator strength of the antenna is defined by the antenna design [88]. By means of this parameter, as well as the resonance frequency as a coarse starting point, the antenna profile can be approximated to the spectra obtained with the laser.

5.3 EXPERIMENTS AND DISCUSSION

First, measurements are conducted using the internal thermal FTIR and the synchrotron light sources. These measurements serve as benchmarks for the experiments conducted with the laser. Fig. 5.6 depicts the spectra of a 1.75 µm-long PLL-covered antenna measured with the Globar (red line color). The measurement conducted with the synchrotron is depicted in a blue line color. Here, a 1.8 µm-long antenna is used. The spectra exhibit the broad plasmonic resonances with central frequencies of 1650 and 1700 cm^{-1}, respectively. For a better visualization the spectra are shifted in transmittance.

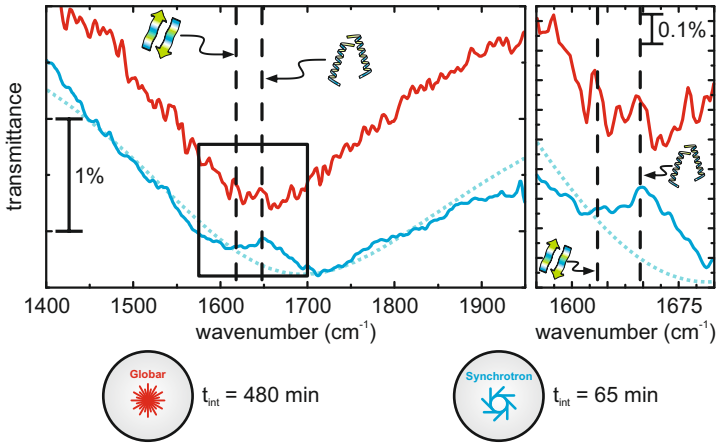

FIGURE 5.6. Measurements conducted with the Globar (red line color, L_{ant} = 1.75 µm) and synchrotron (blue line color, L_{ant} = 1.80 µm). For a better visibility, the spectra are shifted in transmittance. Additionally, the bare resonance profile of the synchrotron measurement is indicated in a short-dotted line and the α-helical and β-sheet resonances are indicated by vertical long-dashed lines. The inset on the right depicts a magnified view of the area of interest. In consequence of high noise, no PLL signal is detected on the Globar measurement. In contrast, a distinct signal at the α-helical resonance (1648 cm^{-1}) is observed using the synchrotron, which exhibits less noise in general despite a significantly shorter measurement time. A SNR of 13 is reached, enabled by the higher synchrotron brilliance. Figure adapted from [68].

Additionally, the antenna profile of the 1.8 µm-long antenna is indicated in a short-dotted line, as well as the expected resonance frequencies of the PLL conformations.

The Globar spectrum exhibits large noise despite a very long integration time of 480 min. Any molecular signal is hidden inside the noise floor, as visible on the right panel of Fig. 5.6 depicting a zoomed in view on the region of interest (1585 to 1700 cm^{-1}). In contrast, a distinct spectral feature at the α-helical amide-I resonance frequency stands out from the antenna spectrum taken with the synchrotron. Despite an 8-times shorter intergration time,

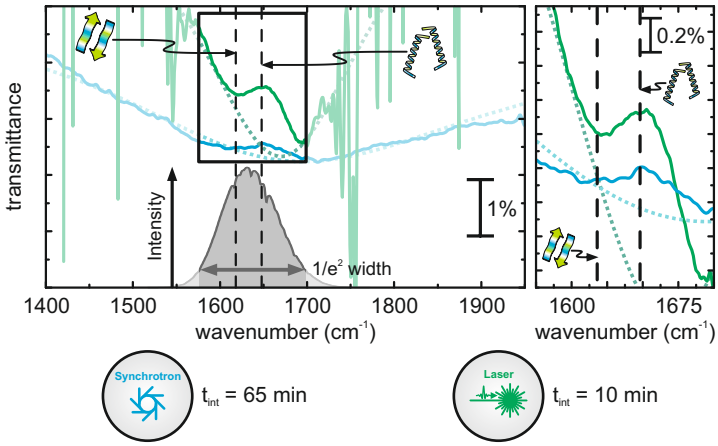

FIGURE 5.7. Application of the laser source. As a reference, the synchrotron spectrum is included as well. The laser intensity distribution, measured on the CaF_2 substrate, is depicted in grey. The laser is tuned to 1634 cm^{-1}, which is central to both PLL resonances. Within its $1/e^2$-width (125 cm^{-1}) sufficient intensity is available for FTIR measurements. The measured antenna spectrum (L_{ant} = 1.75 µm) is depicted in a dark green line color. Lorentzian fits of the antenna profiles are indicated. On the right, the magnified inset is given. The laser spectrum exhibits a significant peak at the α-helical resonance, spectrally matching the synchrotron measurement. A SNR of 58 is measured, compared to 13 using the synchrotron. Figure adapted from [68].

this spectrum exhibits significantly less noise. A SNR of 13 and a single-shot sensitivity of 0.23 % are calculated. As no signal at the β-sheet resonance (1618 cm^{-1}) is detected, the measurement indicates that the polypeptides on this antenna are predominantly in the α-helical state. Similar spectral features have been detected by [70, 71] on large antenna-fields. Our result highlights the importance of a highly brilliant light source to increase the measurement sensitivity. Thus, commercial FTIR setups are capable of detecting and investigating polypeptides at attomolar concentrations.
So far, we showed the feasibility to detect PLL using a single

nanoparticle for plasmonic signal enhancement. However, the synchrotron measurement time is rare and cost-intensive. Ultimately, tabletop sources are the way to go. Therefore, we apply our MIR laser for the following experiments. It is tuned to a central frequency of 1634 cm^{-1}, which is central between the two PLL resonances. Thus, we ensure a similar photon flux for both resonances. The spectral intensity distribution is shown in Fig. 5.7 (grey colored). As the system is purged with nitrogen only minor atmospheric absorption is visible. The laser exhibits 125 cm^{-1} ($1/e^2$-width), which defines the accessible measurement range. In Fig. 5.7 it is confined by semitransparent areas.

Similar to the Globar experiments, a 1.75 µm-long antenna is measured with the laser. The spectrum, as well as the Lorentzian antenna profile are plotted in a green line color. As a reference, we also included the previous synchrotron measurement. The laser FTIR spectrum exhibits very low noise, which is significantly lower than the noise observed on both the synchrotron and Globar spectra. An integration time as short as 10 min is used, being 6- and 48-times shorter than the synchrotron and Globar measurement times, respectively.

By comparing the slopes of the laser and synchrotron spectra, the laser spectrum appears distinctly steeper. This is due to the different illumination geometry of the light sources [32]. Moreover, please note that due to the narrow laser spectrum only parts of the full antenna resonance are visible.

Similarly to the synchrotron measurement, the spectrum conducted with the laser exhibits a strong spectral feature at 1648 cm^{-1} matching the α-helical vibration. The spectra match each other well, as visible on the enlarged view on the right side of Fig. 5.7. However, we reach a SNR of 53 with the laser. This is mainly attributed to the higher laser brilliance and, to some extend, to the illumination geometry. Moreover, the accessible sensitivity using the laser increases fast if data is accumulated. After 10 min, we reach a sensitivity of 0.02 % and after 25 min signals as small as 0.015 % are

detectable. In contrast, the synchrotron exhibits a maximum sensitivity of 0.019 % reached after 30 min, which is 27 % lower compared to the laser. From these observations we conclude that the laser exhibits lower RMS noise in general. However, both light sources exhibit a single-shot sensitivity of 0.23 %. This indicates that this measure is probably due to the spectrometer setup. Possible noise sources are detection noise, mechanical drifts of the microscope, or changes in ambient conditions.

So far, we solely observed α-helical signals. By adding SDS to the liquid environment the polypeptides are partially folded into the β-sheet state ($\nu_{res} = 1618\,\mathrm{cm}^{-1}$). Note that SDS can also cause a polypeptide denaturation. We observed a maximum molecular signal by using a 1.8 µm-long antenna. The full antenna profile measured with the Globar is depicted in Fig. 5.8a). The plasmonic resonance is found at a central frequency of $1600\,\mathrm{cm}^{-1}$ and the spectrum exhibits higher noise compared to an antenna measured in pure D_2O. This is in consequence of additional OH-vibrations due to the SDS.
The measurements conducted with the laser are depicted in Fig. 5.8b). The left panel shows the already presented spectrum, using pure D_2O, whereas the result obtained in D_2O-SDS is given in the right panel. This spectrum shows a broad resonance at $1618\,\mathrm{cm}^{-1}$ at a SNR of 8, which matches the resonance frequency of the β-sheet conformation. The previously observed strong α-helical peak at $1648\,\mathrm{cm}^{-1}$ vanished completely. This observation and the detected signal strength indicate that the polypeptides folded into the β-sheet state or denaturated.
In the D_2O-SDS solution we derive a decreased single-shot sensitivity of 0.58 % due to the additional OH-vibrations. After 45 min integration time the sensitivity reaches 0.068 %.
During the experiments we measured several other antennas to reproduce the results and investigate the plasmonic enhancement. Another measurement conducted in D_2O is shown in Fig. 5.9. In a), the full profile of the 1.70 µm-long antenna (Globar measurement) is depicted, showing a central frequency of $1750\,\mathrm{cm}^{-1}$. The

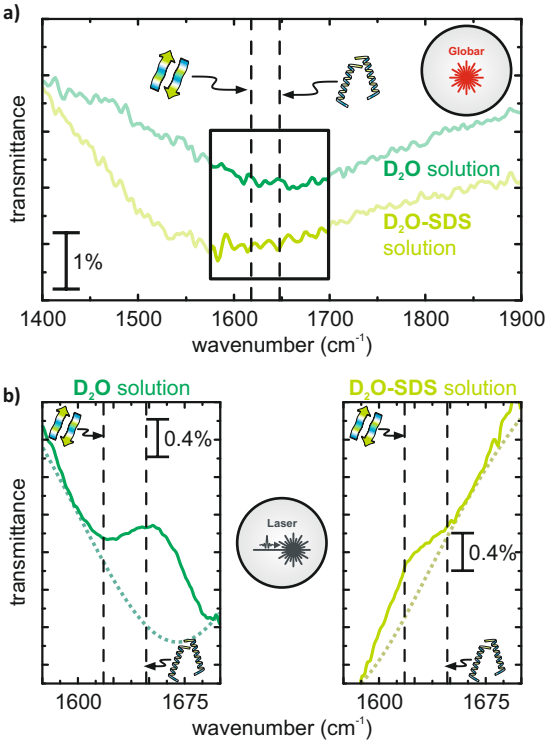

FIGURE 5.8. Investigation in D_2O-SDS solution. Here, the β-sheet conformation is expected to be more pronounced. **a)** Antenna characterization in D_2O-SDS (light green line color, $L_{ant} = 1.80\,\mu m$) and D_2O employing the Globar. OH-vibrations resulting from SDS lead to a higher noise level, in general. **b)** Results obtained in the different environments employing the laser. Again, Lorentzian fits indicate the antenna profiles. Compared to the measurement in D_2O (dark green) the distinct α-helical peak vanished, whereas a signal at the β-sheet resonance is detected. A SNR of 8 is measured after 45 min integration time. This comparison shows that both PLL conformations can be detected with the laser *without* frequency tuning and within minutes. Figure adapted from [68].

corresponding spectrum measured with the laser ($t_{int} = 45$ min) is given in Fig. 5.9b). In contrast to the spectrum obtained with the 1.75 µm-long antenna (right panel), this measurement exhibits two

spectral features on top of the antenna profile. The peaks match the α-helical and β-sheet resonances, as indicated. As the signal strength is small, the first derivative of the spectrum is plotted below, showing the two distinct peaks more clearly. This measurement highlights the laser bandwidth, allowing for the detection of both PLL conformations simultaneously without frequency tuning, which has not been feasible with previous laser sources.
The weak signal strength of this measurement is most likely attributed to the sample functionalization or preparation, as the polypeptide adsorption strongly depends on the condition of the MUA/MUoL layer. It might happen that the polypeptides clump, denature, or that the adsorption, i.e. coupling to the antenna is low.

To show the high measurement sensitivity that is achieved with the laser, the temporal evolution of the measurements in D_2O is depicted in Fig. 5.10. A distinct signal is already visible after 1 min, as shown in the right panel. But also weaker signals are well visible after a few minutes as depicted on the left panel. In general, the RMS noise is low and the sensitivity reaches the previously mentioned 0.02 % after 10 min.

An additional measurement conducted in D_2O-SDS is given in Fig. 5.9a) and b). Here, a 1.75 µm-long antenna is used. Despite a weak signal amplitude two weak peaks at the corresponding α-helical and β-sheet resonances are visible. Again, the first derivative is plotted below, highlighting the two peaks. The weak signal amplitude is attributed to the added SDS, which also causes a denaturation of the polypeptides.

5.4 CONCLUSION

Based on these results, different polypeptide conformations have been investigated in-vitro using attomolar concentrations. This is

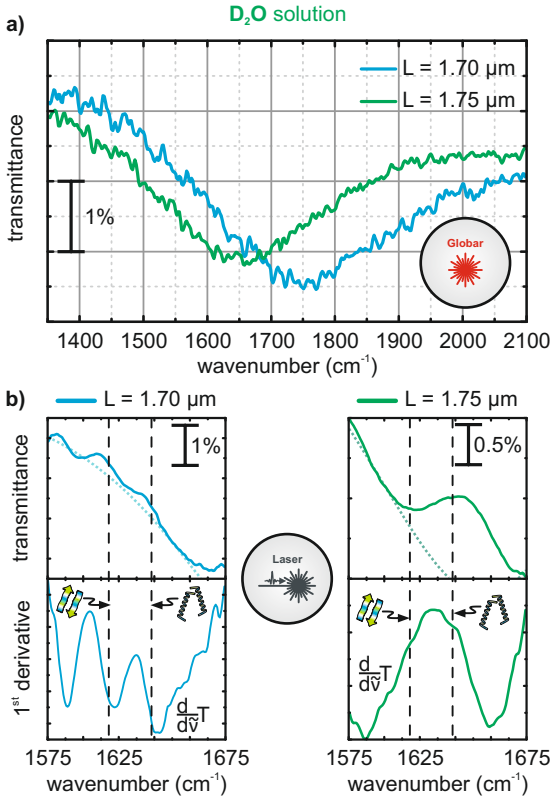

FIGURE 5.9. Comparison between the 1.75 µm-long reference (dark green) and a 1.70 µm-long (blue) antenna in D_2O solution. **a)** Antenna profiles measured with the Globar. With decreasing antenna length the resonance frequency blue-shifts to 1750 cm^{-1}. **b)** Spectra of both antennas obtained with the laser. The calculated first derivatives are plotted below. In comparison to the reference (dark green), two peaks are visible on the blue-shifted antenna spectrum, matching the α-helical and β-sheet resonances. The signal magnitude is reduced in consequence of the increased detuning [45] and functionalization. Both peaks are distinctly visible in the first derivative. This shows that both PLL conformations are present on the antennas in D_2O, but at different ratio and magnitude. Figure adapted from [68].

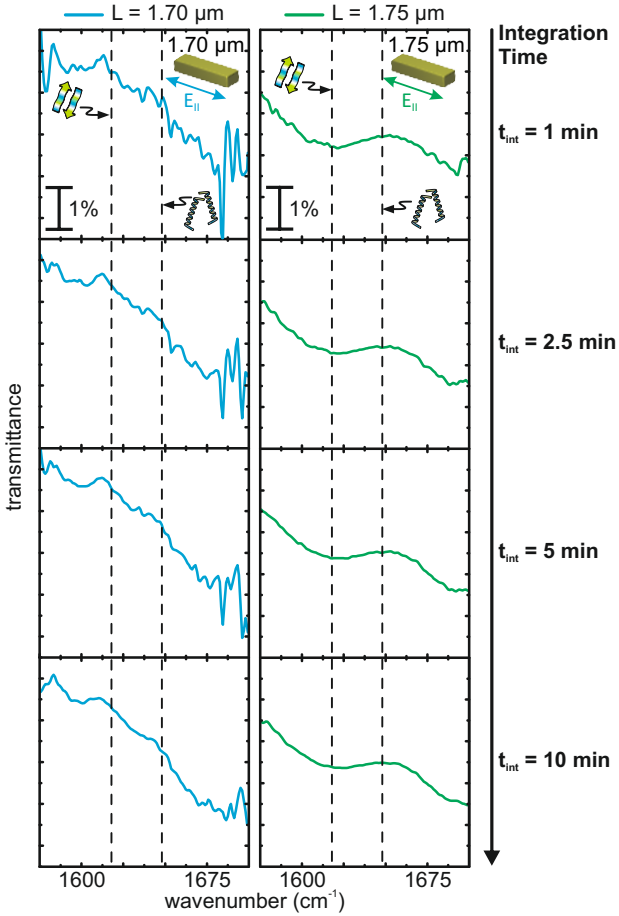

FIGURE 5.10. Temporal evolution of the spectra depicted in Fig. 5.9a). For optimum signal enhancement, i.e. optimum matching of the PLL and plasmonic resonance frequencies, the molecular signal is well visible after 1 min integration time. In general, a high SNR is reached after 10 min for both measurements, in consequence of a low RMS noise of 0.02 %. Figure adapted from [68].

enabled by employing a laser light source, which reaches a brilliance on the order of 1×10^{19} ph/s/mm²/sr. In consequence of its

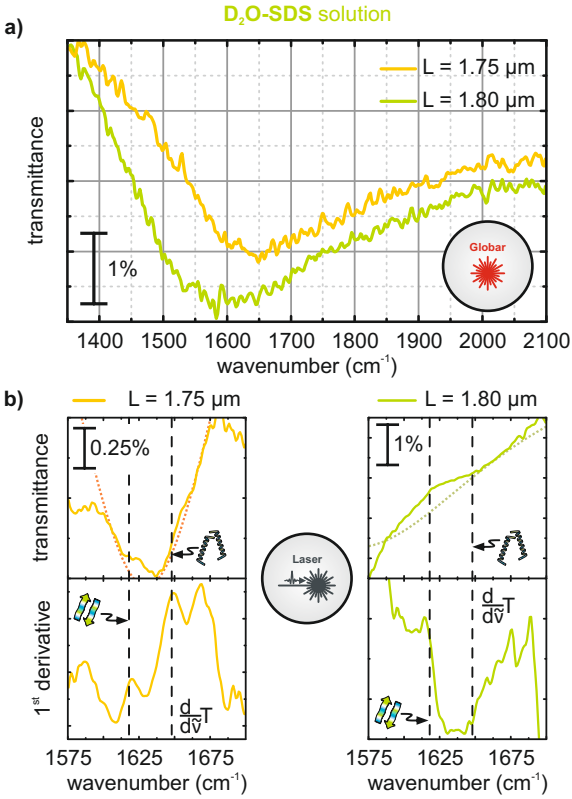

FIGURE 5.11. Comparison between the 1.80 µm-long reference (light green) and a 1.75 µm-long (yellow) antenna in D_2O-SDS solution. **a)** Characterization of the antenna profiles. The 1.75 µm-long antenna exhibits a resonance frequency of 1650 cm^{-1}. **b)** Spectra measured with the laser and first derivatives. Using the 1.75 µm-long antenna, the spectrum exhibits a molecular signal at the β-sheet resonance. A weaker signal at the α-helical resonance is visible as well. Both peaks are also visible in the first derivative. Compared to the reference (light green), a higher noise level is obvious on that antenna sample. The weaker signal amplitudes are attributed to more pronounced denaturation of the polypeptides. Figure adapted from [68].

high brilliance, excellent beam quality and long-term stability, the achieved measurement sensitivity significantly exceeds the sensitivity of Globar and synchrotron light sources. Thus, about 1600 PLL molecules (attomolar concentration) can be detected within a few minutes. Short integration times are of crucial importance to investigate dynamic folding mechanisms. Further advances of laser-based micro-FTIR spectroscopy will enable measurements close to, or reaching single protein concentrations, which is the ultimate goal to investigate their reaction to external stimuli. Furthermore, this setup offers a great variety of new FTIR applications, which have been impeded so far by long integration times and high noise using thermal light sources, or limited measurement time and high costs at synchrotron facilities.

6

ROBUST AND EFFICIENT DIFFERENCE FREQUENCY GENERATION WITH INTRINSICALLY STABILIZED BEAM POINTING

Mid-infrared laser systems can provide significant advantages in IR spectroscopy compared to the often used thermal light sources. As discussed in the previous chapters they allow for an enhanced sensitivity, nm-scale spatial resolution and significantly shorter measurement times. In consequence of the growing demand for MIR spectroscopy in order to investigate new materials for e.g. hydrogen storage, solar cells, ultrasmall (opto-)electronic devices, such light sources that provide high power over a broad MIR range are strongly required. In this chapter we address two main issues, which we experienced during the application of our MIR laser system [12, 64, 68], presented in Chapters 4 and 5. First, we observe a spatial beam offset during wavelength tuning in consequence of birefringent phase-matching, which is typically required in DFG. Second, higher conversion efficiency beyond 10 µm wavelength would be beneficial for many applications, especially if the available oscillator power is limited as described in Chapter 4. We present an approach that successfully circumvents beam pointing issues over a broad wavelength range and provides up to 10 times higher conversion efficiency for wavelengths exceeding 11 µm compared to a signal-ider DFG setup. Thus, milliwatts of output power are measured up to 20 µm wavelength.

This chapter is based on the following peer-reviewed publication [24]: F. Mörz, T. Steinle, H. Linnenbank, A. Steinmann, and H. Giessen, "Alignment-free differnce frequency light source tunable

from 5 to 20 µm by mixing two independently tunable OPOs," *Optics Express* **28**, 11883-11891 (2020). Reprinted adapted with permission. Copyright: 2020, Optical Society of America under the terms of the OSA Open Access Publishing Agreement

6.1 INTRODUCTION

The application of MIR laser systems, exhibiting a high brilliance, enables a high sensitivity, low noise, and thus, fast spectroscopic measurements. In the previous chapter, I applied such a laser system for the in-vitro detection of polypeptide conformations at attomolar concentrations, i.e. at nm spatial resolution [68], which has not been feasible with standard thermal light sources. Other applications that are based on MIR lasers are for example the detection of individual protein complexes [72], monitoring the hydrogen diffusion into metal hydrides [35], or the characterization of novel materials in the fingerprint region for optoelectronic devices. Different MIR laser systems have been presented in recent years, being based on supercontinuum generation [89], quantum cascade laser (QCL) [10, 11], frequency combs [7, 8], MIR OPOs, or intrapulse DFG [40].
Our system which has been employed in Chapter 4 and Chapter 5 mixes the signal and idler beams of a single OPO or OPA for difference frequency generation. Beside its broad tuning range and high output power [12] this system is easy to implement for near- and far-field applications [35, 64, 68]. However, its beam pointing stability during wavelength tuning and its conversion efficiency at wavelengths exceeding 11 µm can be improved. Due to angular phase-matching the nonlinear gain medium needs to be rotated during wavelength tuning, which causes a spatial beam offset of the generated beam according to Snell's law. There are only few nonlinear MIR crystals allowing for QPM, such as OP-GaP or OP-GaAs, but those are limited in phase-matching bandwidth and

transmission range [90–94]. Therefore most MIR laser systems require a beam offset compensation to achieve stable beam pointing, i.e. to maintain the coupling into spectroscopy setups during wavelength tuning. Currently, this is addressed by active beam pointing stabilization with reflective optical elements or counter-rotating optics that compensate the crystal rotation. However, active beam pointing stabilization requires the monitoring of the beam position and multiple movable optics. This can become rather complex and expensive, or time consuming, if done manually. Counter-rotating optics can be mechanically synchronized to the nonlinear crystal, which simplifies the beam offset compensation at first glance. However, they need to exhibit similar characteristics as the utilized nonlinear crystal. This adds dispersion and significantly reduces the MIR output power due to transmission and Fresnel losses.
Furthermore, the performance of standard DFG schemes using signal and idler beams of a single OPO/OPA decreases for longer wavelengths ($> 11\,\mu m$), as the OPO/OPA needs to be operated near degeneracy to provide the required, close-lying signal and idler wavelengths. This results in reduced signal, idler power and stability and translates to the DFG setup. Additionally, the transparency of MIR gain media significantly decreases between 10 to 20 µm, which reduces the achievable output power even more.
In the following, we address these issues and present a DFG scheme, which exhibits intrinsically stabilized beam pointing from 11 to 20 µm and exhibits stable photon efficiency from 5 to 15 µm. This is achieved by mixing two independently tunable input beams instead of the wavelength dependent signal and idler beams of a single OPO/OPA. Thus, an additional degree of freedom is introduced, which allows to fix the crystal orientation and satisfy phase-matching by choosing the appropriate input wavelengths. GaSe is used as a nonlinear crystal, as it allows for DFG up to 20 µm, exhibits a high damage threshold and high nonlinearity. To validate our concept we present a detailed comparison to the more commonly used signal-idler DFG.

6.2 EXPERIMENTAL PREPARATION

The experimental setups of our Dual OPO/OPA DFG concept and the reference signal-idler DFG are depicted in Fig. 6.1a) and b). Both setups are pumped by a Yb-based solid-state oscillator, delivering 7 W at a central wavelength of 1.039 µm. It exhibits 500 fs-long pulses at a repetition rate of 40 MHz. The oscillator synchronously pumps a FFOPO and an subsequent OPA, which amplifies the FFOPO-signal. In total 2.3 W pump power is applied on the FFOPO and about 2.3 W to pump the post-amplifier. Both use 10 mm-long lithium tantalate crystals with fan-out poling as nonlinear gain media. The generated signal beam is used to pump the DFG. In the required range from 1.45 to 1.60 µm about 1 W power is accessible. In order to circumvent rotating the DFG crystal we added a second FFOPO, which is also pumped by the identical Yb-oscillator, as depicted in Fig. 6.1a). A maximum pump power of 2.3 W is applied. This second FFOPO delivers the seed beam for the DFG process. Periodically-poled lithium niobate is used as a nonlinear gain medium. Seed wavelengths between 1.60 and 1.95 µm are required for the DFG process. In that range the FFOPO delivers 225 to 500 mW output power. By pumping the amplified FFOPO and the second FFOPO with the identical oscillator, temporal synchronization of the DFG input pulses is easy to establish. The input beams are combined using a polarizing beam splitter.
As indicated in Fig. 6.1b), the post-amplified FFOPO delivers the input beams for the signal-idler DFG. For this purpose, the OPA pump power is increased to 4 W.
As a DFG gain medium GaSe is used, as it provides a high damage threshold, high nonlinearity, and supports a broad tuning range. However, due to the large spatial walk-off (57 mrad at 10 µm wavelength), the effective interaction length in GaSe is very short, which results in a low conversion efficiency. As a brief example, I assume a minimum beam waist of 30 µm at 10 µm wavelength. This corresponds to the required beam waist w_0, which satisfies Boyd's criterion, given in Eq. (2.46), for a 4 mm-long crystal. However,

after propagating 1 mm in GaSe, the interacting beams are spatially separated by 57 µm, i.e. they are completely separated. For that reason different GaSe crystals with varying length between 1 and 4 mm are tested, with increasing beam waists. The highest power is finally achieved with a 4 mm-long GaSe crystal (*Eksma Optics*). The estimated beam waist in the crystal is about 50 µm, although it is probably larger in reality. The transmission through the crystal at about 35° AOI is given in Fig. 6.2.

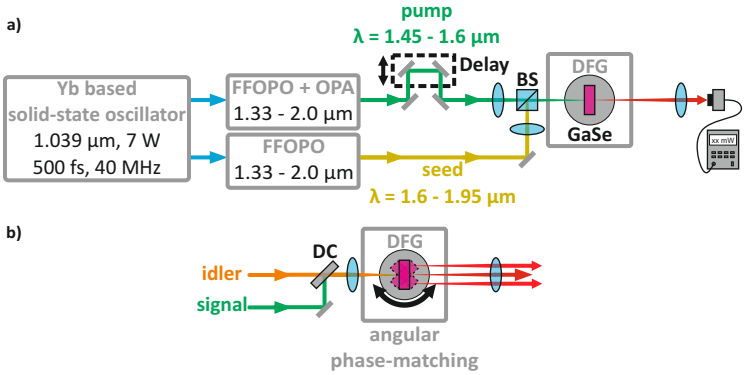

FIGURE 6.1. Schematic setup of **a)** the *Dual OPO/OPA DFG* and the commonly used *signal-idler DFG* (**b)**). The setups are pumped by an Yb solid-state oscillator. In **a)** it synchronously pumps two FFOPOs, from which one is further amplified. About 2.3 W pump power is applied for each FFOPO and the OPA. The amplified FFOPO delivers the pump beam for the DFG. The wavelength-independent pump and seed beams are combined using a polarizing beam splitter. In **b)**, the signal and idler beams of the amplified FFOPO are used to pump and seed the DFG. Here, 4 W pump power is used for the amplifier. Both setups use a 4 mm-long GaSe DFG crystal (Eksma Optics). Figure adapted from [24].

Behind the crystal the DFG beam is separated from the residual pump and seed beams and collimated using an off-axis paraboloid with 50.8 mm reflected focal length (RFL). For mid-IR wavelengths

shorter than 11.5 µm a 4.7 µm long-pass filter is employed, whereas a 7.3 µm long-pass filter is installed for longer wavelengths. The generated DFG power is measured using a thermal power meter (Ophir 3A sensor) after the collimation and spectral filtering. To calculate the photon efficiency, the reflected input power on the crystal front facet is subtracted from the applied input power, measured in front of the crystal. In consequence of the high refractive index and large AOI (typ. 35°) the reflected power reaches 25 % of the applied power, in average. For other tilt angles or type-II phase-matching even higher Fresnel losses are expected.

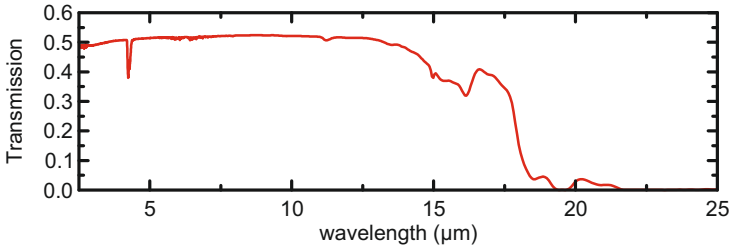

FIGURE 6.2. Qualitative transmission through a 4 mm-long GaSe crystal at 35° AOI. Measured at a *Bruker Vertex* 80 FTIR spectrometer using air as a reference. The quantitative transmission might differ, due to the spectrometer alignment.

Phase-matching

In a standard DFG setup, i.e. signal-idler DFG, the DFG wavelength requires a specific signal wavelength according to

$$\lambda_{DFG} = \frac{\lambda_{sig} \cdot \lambda_{osc}}{2\lambda_{osc} - \lambda_{sig}}. \tag{6.1}$$

This equation is only satisfied by a single OPO/OPA signal wavelength λ_{sig} for a given oscillator and DFG wavelength λ_{osc}, λ_{DFG}, respectively. Phase-matching is achieved by adjusting the crystal angle, as described in Section 2.4, for each set of wavelengths. By using two independently tunable input beams, this equation changes to

$$\lambda_{DFG} = \frac{\lambda_{sig} \cdot \lambda_{sig2}}{\lambda_{sig2} - \lambda_{sig}}. \tag{6.2}$$

This equation is satisfied by many different combinations of input wavelengths. This degree of freedom allows to fix the crystal angle during wavelength tuning and satisfy phase-matching by choosing the appropriate pair of input wavelengths. Here, λ_{sig} denotes the signal wavelength of the amplified FFOPO, i.e. the DFG pump wavelength, whereas λ_{sig2} denotes the DFG seed wavelength, delivered by the second FFOPO. It is $\lambda_{sig} < \lambda_{sig2}$.
We aim for a constant crystal angle over the broadest possible wavelength range to achieve intrinsically stable beam pointing. However, we define the following limits. First, we solely use OPO/OPA signal wavelengths, which means the input wavelengths range from 1.4 to 2 µm. This allows for standard optics and a simple setup. Second, we avoid atmospheric and known AR-coating induces absorption windows. Third, to achieve high DFG power and stability from 10 to 20 µm, we avoid operation close to the degeneracy of the input sources in that region. Finally, we allow for maximum angular variations within the mean acceptance bandwidth of GaSe ($\Delta\theta = 0.4°$) to refer to a constant DFG crystal angle. Within this range phase-matching can be achieved without adjusting the crystal, as discussed in Section 2.4. The mean acceptance bandwidth is derived from the *SNLO* library. Accounting for these limits, we achieve a constant crystal orientation in the range from 9 to 20 µm. In general, this concept is applicable to many different gain media and we calculated different configurations for some of the most frequently used DFG crystals. Fig. 6.3 compares the required angular variation relative to the beam propagation direction for our

concept (left panel) and a signal-idler DFG (right panel). We assume type-I phase-matching if possible. The semitransparent red areas illustrate the acceptance bandwidth $\Delta\theta$ for the respective crystal using 4 mm length. We neglect the spectral dependence of the acceptance bandwidth and the given values depict the median acceptance bandwidth. All data points that are within the semitransparent red areas can be generated without adapting the crystal angle. Of course, optimum phase-matching is achieved at zero deviation from the exact phase-matching angle, i.e. at the center of the red areas. Fig. 6.3 shows that our concept allows to significantly minimize the required angle tuning. Especially GaSe, $AgGaSe_2$ and CdSe allow for broad wavelength ranges with nearly zero angular tuning. In comparison, the signal-idler DFG typically requires several degrees of crystal tuning in the identical range.
A more detailed investigation shows that other crystal parameters such as the effective nonlinearity, figure of merit (FOM), or the spatial walk-off can be tailored as well using our concept.

6.3 RESULTS

Dual OPO/OPA DFG

First, experiments are conducted using the Dual OPO/OPA DFG. As mentioned, nearly zero angular tuning can be achieved from 9 to 20 µm. The crystal angle is set to 35° AOI. The calculated pump and seed wavelengths are depicted in Fig. 6.4a). They are adjusted with a precision of 0.3 nm. For wavelengths exceeding 12.5 µm the pump wavelength remains constant at 1.46 µm. This simplifies the operation of our concept significantly, as only the seed wavelength needs to be adjusted to reach higher wavelengths. To validate our concept and measure the experimental angular variation, the crystal angle is optimized during tuning. Below 9 µm DFG wavelength, the required seed would exceed our allowed

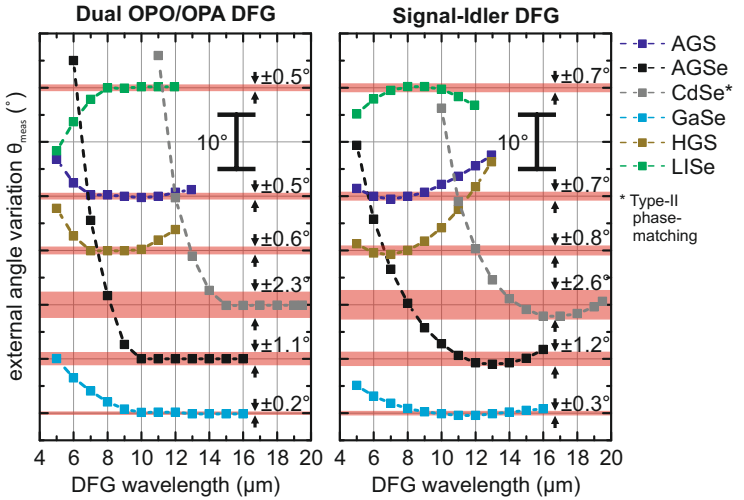

FIGURE 6.3. Angle *variation* relative to the beam propagation direction of the Dual OPO DFG (left panel) and signal-idler DFG (right panel). Type-I phase-matching is used, if not marked differently. The red areas depict the median acceptance bandwidth for 4 mm crystal length. By using decoupled input beams the required angular variation can be significantly minimized. Especially GaSe, $AgGaSe_2$, or CdSe allow for nearly zero angular tuning over a broad wavelength range. In contrast, the signal-idler DFG requires several degrees tuning within the identical range. Figure adapted from [24].

input range. To access shorter wavelength, we adjusted the crystal angle. Here, the seed wavelength is kept fairly constant. As this is beyond the intention of this work, this wavelength range is plotted semitransparent.

As shown in Fig. 6.4b) about 1 W pump power is available in average. The seed power *increases* to about 400 mW with *increasing* DFG wavelength. Thus, high input power and stability is ensured at the DFG limit. This is in contrast to a signal-idler DFG, where the input power of both pump and seed beam drops in consequence of the near-degeneracy operation of the OPO/OPA.

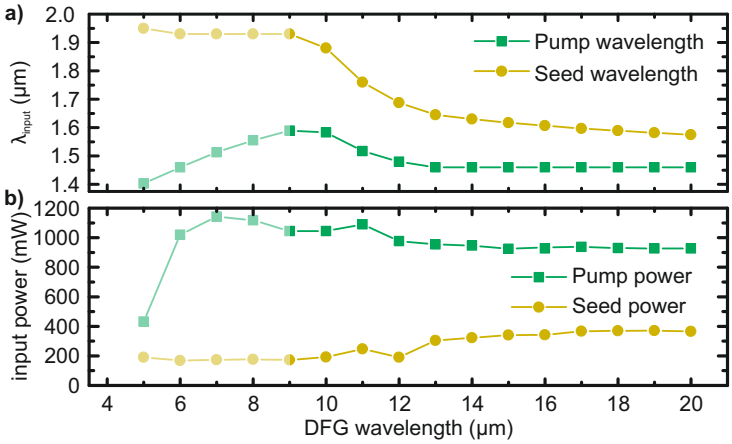

FIGURE 6.4. **a)** Required pump and seed wavelengths for the Dual OPO/OPA DFG. As the DFG is optimized to achieve a constant crystal angle above 9 μm wavelength, the shorter wavelengths appear semitransparent. Above 12.5 μm the pump wavelength remains constant, which simplifies the operation significantly as only the seed wavelength is adjusted. The GaSe crystal is fixed at 33.5° from 9 to 20 μm. This corresponds to a phase-matching angle of 11.6°. **b)** About 1 W pump power is applied from 6 to 20 μm DFG wavelength. The seed power *increases* to about 400 mW for *increasing* DFG wavelengths, which ensures high output power at the DFG limit. Figure adapted from [24].

The generated MIR power and photon efficiency are depicted in Fig. 6.5. A maximum output power of 13 mW is achieved at 7 μm, which corresponds to a photon efficiency of 5.3 %. 1142 mW pump and 174 mW seed power is applied. The photon efficiency remains on the order of 5 % between 5 and 14 μm, with 6.2 % maximum efficiency at 11 μm. From 15 to 20 μm the output power and photon efficiency decrease continuously in consequence of the decreasing transparency of GaSe as depicted in Fig. 6.2. At 20 μm about 0.5 mW is still generated, which corresponds to just below 1 % photon efficiency.

At 12 μm a significant power and efficiency drop is observed. This is due to low seed power (see Fig. 6.4), as the FFOPO is operated at

the limit of the corresponding poling period.
Finally, the photon efficiency is investigated as a function of applied pump and seed power. At 11.5 µm wavelength, saturation is observed using a constant seed (190 mW) but continuously increasing pump power. In contrast, the efficiency exhibits no saturation by applying a constant pump (1000 mW) but increasing seed power. The identical behavior is observed at 13.5 µm. This shows that the accessible efficiency and output power can be further increased by applying higher seed power, whereas the pump power is at optimum level (saturating efficiency). Both measurements exhibit a linear dependence of the generated DFG power on the pump and seed power, which shows that the reported experiments remain in a low gain regime, matching Eq. (2.42). Therefore comparable pump and seed power is beneficial, which needs to be adapted in the future. However, this is currently limited by the available oscillator power.

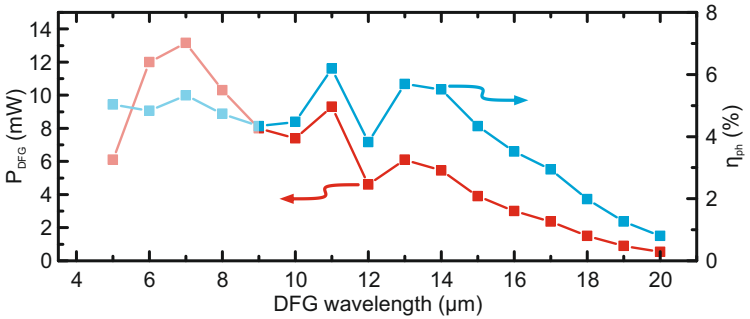

FIGURE 6.5. Dual OPO/OPA DFG output power. A tuning range from 5 to 20 µm is achieved, exhibiting maximum 13 mW output power at 7 µm. Maximum photon efficiency of 6.2 % is detected at 11 µm. About 5 % efficiency is measured up to 15 µm wavelength. Figure adapted from [24].

Fig. 6.6 depicts the measured and calculated angular variation. The measurement follows the expected values well and shows minimum angular variation within the allowed limit of the acceptance bandwidth of $\Delta\theta = 0.4°$ above 9 µm. From 11 to 20 µm the crystal angle changes negligible by just 0.3°.

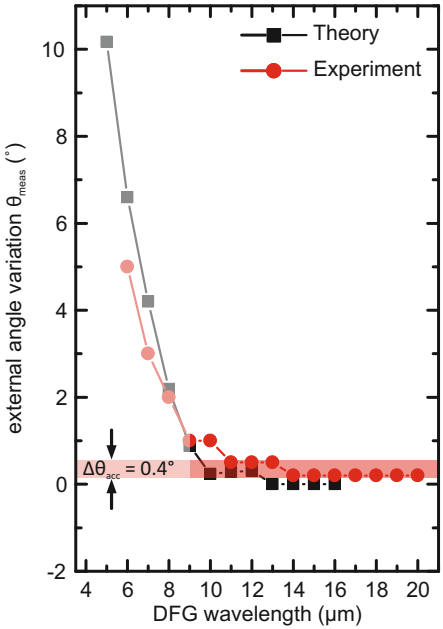

FIGURE 6.6. Measured and calculated angle variation. The crystal remains constant from 11 to 20 µm. Negligible rotation of 0.3° is measured after verifying the set angle for maximum output power. As calculated the angular variation remains within the acceptance bandwidth of $\Delta\theta = 0.4°$. A significant angle variation is required below 9 µm, as we limited the seed wavelength to 1.95 µm. From 5 to 9 µm phase-matching is achieved via angle tuning. Figure adapted from [24].

Fig. 6.7 depicts the long-term power measured at 12 µm wavelength. The DFG output is set to 1.935 mW and monitored for

45 min. Within that time duration a standard deviation of 38 µW is measured, which corresponds to the intrinsic noise of the power meter. In consequence of the parametric frequency conversion, the DFG noise directly depends on the noise of the input beams, which show a long-term stability of 0.1 %rms [12].

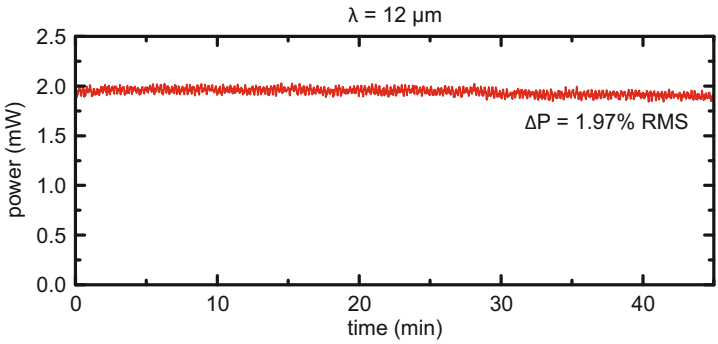

FIGURE 6.7. Power stability measurement at 12 µm wavelength. A standard deviation of 38 µW is measured corresponding to 1.97 %rms. This corresponds to the intrinsic power meter noise. The FFOPO and OPA show a standard deviation of 0.1 %rms, which is expected for the DFG as well. Figure adapted from [24].

Signal-idler DFG

Next, experiments are conducted using the signal-idler DFG scheme. The identical GaSe crystal and beam parameters are applied. The applied input wavelengths and corresponding power is shown in Fig. 6.8a) and b). Reaching longer DFG wavelengths the input beams approach the OPA degeneracy. This results in a decreasing input power, as visible in Fig. 6.8b). At 6 µm DFG wavelength 813 mW pump power is available, compared to 268 mW at 17 µm. Simultaneously the seed power drops from 276 to 127 mW. In contrast,

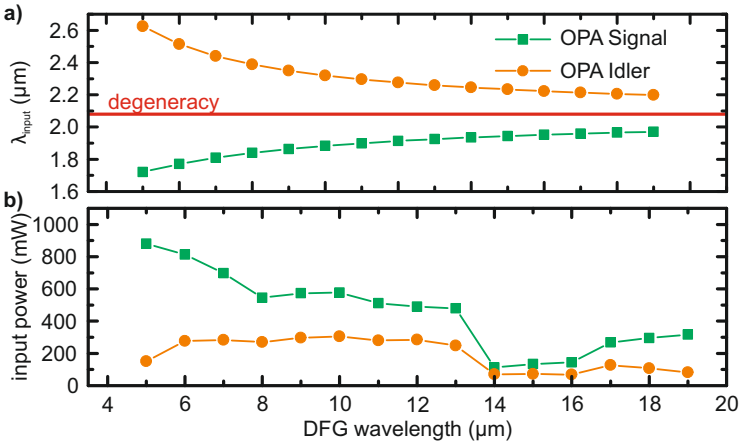

FIGURE 6.8. Input wavelengths (**a**) and power (**b**) of the signal-idler DFG. The wavelengths approach the OPO/OPA degeneracy for longer wavelengths. This results in a decreasing DFG pump and seed power. At 6 µm 813 mW pump power and 276 mW seed power is applied. At 17 µm the pump power drops to 268 mW, the seed power reaches 127 mW. Between 14 and 16 µm the pump power drops significantly due to an AR-coating induced absorption. The increasing pump power from 17 to 19 µm is partly due to idler power (seed) leaking into the pump power beam path, as the wavelengths are close to the dichroic mirror's (beam combiner) filter edge. Figure adapted from [24].

the Dual OPO/OPA DFG allows for nearly constant pump power around 1 W and about 400 mW seed power.

Fig. 6.9 depicts a direct comparison of the obtained results to the Dual OPO/OPA DFG. Up to 35 mW output power is achieved at 6 µm wavelength. This corresponds to 14.4 % photon efficiency. At 6 µm wavelength, 813 mW pump and 277 mW seed power is applied, which is efficiently used as GaSe shows maximum gain in this wavelength region. Towards longer wavelengths, the performance of the signal-idler DFG drops significantly, as visible in Fig. 6.9a) and b). However, it is is unexpectedly low between 14 to 16 µm. This is attributed to an AR-coating induced absorption in the range from 1.93 to 1.95 µm, which attenuates the signal and idler power,

as shown in Fig. 6.8b). The typically expected DFG power can be estimated by assuming a continuous decrease from 13 to 17 µm. Towards 19 µm the output power drops to a few tens of µW and no power is detected at 20 µm.

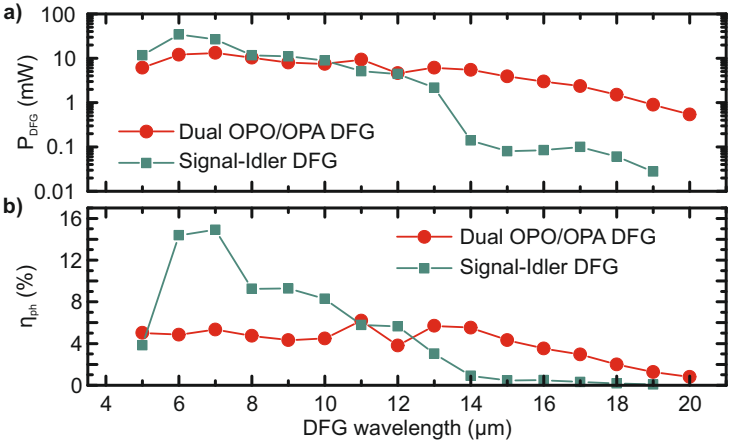

FIGURE 6.9. Performance comparison of the signal-idler and Dual OPO/OPA DFG. **a)** 35 mW are achieved using the signal-idler DFG, which shows better performance below 11 µm. At longer wavelengths the performance drops significantly due to the near-degeneracy operation of the amplified FFOPO. Only a few tens of µW are generated at 19 µm maximum wavelength. **b)** Corresponding photon efficiency. Below 11 µm the signal-idler DFG remains superior, whereas the Dual OPO/OPA DFG exhibits stable performance from 5 to 20 µm. Figure adapted from [24].

To qualitatively compare both DFG setups the photon efficiency is more meaningful, as it normalizes the generated power to the applied pump power. A direct comparison is given in Fig. 6.9b). The signal-idler DFG performance is superior in the range from 5 to 10 µm in consequence of a higher seed power. However, this range is basically outside the range for which the Dual OPO/OPA DFG

is designed. From 11 µm on the Dual OPO/OPA DFG concept provides both higher output power and up to 10-times higher photon efficiency. Up to 20 µm it allows for mW output power compared to µW using the signal-idler DFG. This is attributed to the shorter applied pump and seed wavelengths, as the gain, output power, FOM and efficiency are anti-proportional to these wavelengths, as discussed in Section 2.4. Furthermore, the corresponding input power is higher using the Dual OPO DFG, as visible by comparing Fig. 6.4b) Fig. 6.8b). I would like to point out that the pump to seed power ratio of the signal-idler DFG is favorable. The applied seed power remains disregarded in the photon efficiency calculation, but contributes to the generated power comparable to the pump power, as described in Section 2.4.
Absorption resulting from optical elements is avoided efficiently using our concept. The most important difference between the two DFG concepts is depicted in Fig. 6.10, comparing the angle variation of both concepts. Whereas the Dual OPO/OPA DFG requires negligible angular tuning from 9 µm on, the signal-idler DFG requires about 5° crystal rotation. Note that the range below 10 µm is neglected, as the Dual OPO/OPA DFG concept is intended for longer wavelengths. All in all, the observed beam pointing issues resulting from crystal rotation can be avoided with our new concept. Different wavelength ranges are covered by using different sets of input wavelengths and, or other gain media, as depicted in Fig. 6.3. This also goes along with an increased photon efficiency and the concept allows for tailoring other parameters, such as the effective nonlinearity, or the spatial walk-off.

6.4 ALTERNATIVE CONFIGURATIONS USING THE DUAL OPO/OPA CONCEPT

So far, I presented one possible configuration using the the Dual OPO/OPA concept. Beside maintaining a specific crystal orientation, this concept allows for other configurations, exploiting the

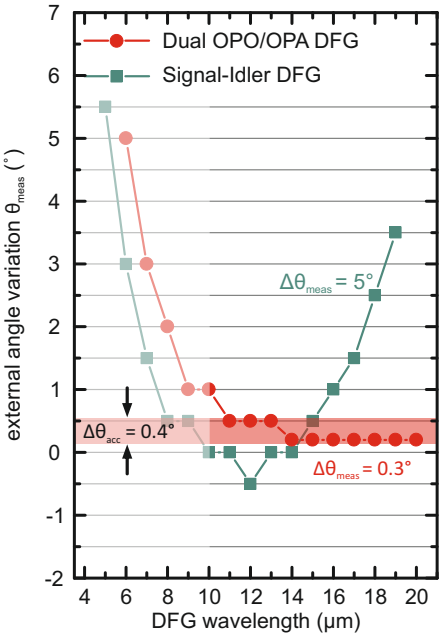

FIGURE 6.10. Comparison of the experimentally measured crystal rotation from 9 to 20 µm. Negligible crystal rotation within the acceptance bandwidth $\Delta\theta$ is achieved with the Dual OPO/OPA DFG, compared to 5° rotation using the signal-idler DFG. The range below 9 µm is neglected, due to the self-set wavelength limit using the Dual OPO/OPA DFG. Figure adapted from [24].

additional degree of freedom of independently tunable input wavelengths. The reviewers for [24] remarked that it might be complex to wavelength tune two OPO setups, instead of one. For automated setups this is negligible, but it is correct for manual setups. Therefore, I would like to present a configuration, which uses a constant seed wavelength over the entire tuning range. This configuration also requires angular crystal tuning, but in general its complexity is similar to a signal-idler DFG setup. However, it also avoids near-degeneracy operation at long MIR wavelengths and thus allows for an improved performance. By using a seed wavelength of 1.75 µm

high input power is applicable, absorption windows are avoided and standard optical elements can be used. As depicted in Fig. 6.11a), the pump beam is tuned from 1.4 to 1.6 µm, which enables a DFG tuning range from 7 to 19 µm. The lower limit ($\lambda_p = 1.4$ µm) is given by the amplified FFOPO tuning range. The applied input power is shown in Fig. 6.11b). About 1 W pump power is applied from 8 to 19 µm. The effectively applied seed power reaches about 250 mW.

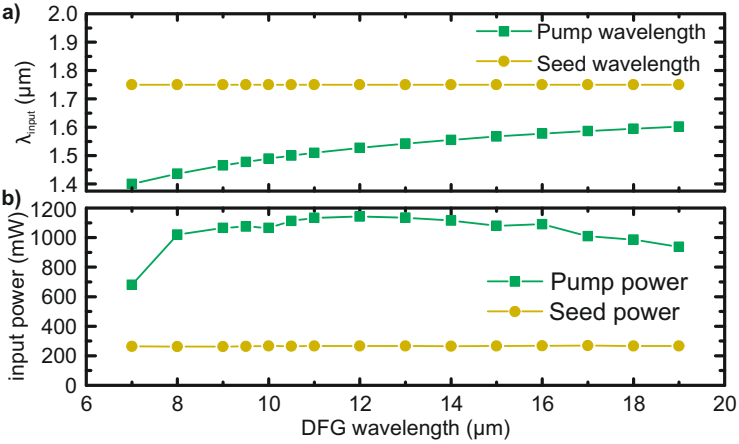

FIGURE 6.11. **a)** Pump and DFG wavelengths for using a seed beam at 1.75 µm wavelength. The pump wavelength is tuned from 1.4 to 1.6 µm. Thus, critical atmospheric absorption is avoided, and standard optical elements can be used. **b)** More than 1 W pump power is available in general. The input power remains at long DFG wavelength, ensuring high DFG power.

Fig. 6.12 depicts the calculated and measured crystal rotation to achieve phase-matching. 10° rotation is required of the entire tuning range, which is on the order of the signal-idler DFG. However, the angle remains fairly constant above 12 µm.

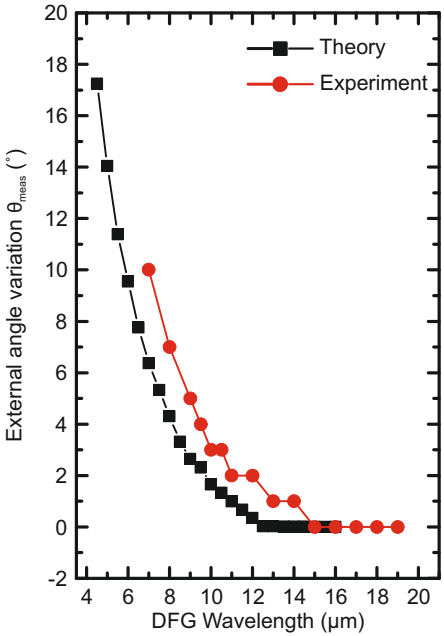

FIGURE 6.12. Calculated (black) and measured (red) crystal rotation to achieve phase-matching. In total about 10° rotation is required, which is on the order of a signal-idler DFG. However, little crystal rotation is required to reach wavelengths above 12 µm. At 14 µm the absolute crystal angle is 33.2°, which correspond to an internal phase-matching angle of 11.5°.

Up to 14 mW DFG power is generated using this concept. The output power remains in the mW-range up to 19 µm, as both input sources are operated within their optimum performance range. Fig. 6.13 depicts the achieved output power (red linecolor) and photon efficiency (blue linecolor). Up to 7 % photon efficiency is measured. Higher output power is achieved compared to the previous configuration using a constant crystal orientation below 11 µm. Above, the performance is slightly weaker.

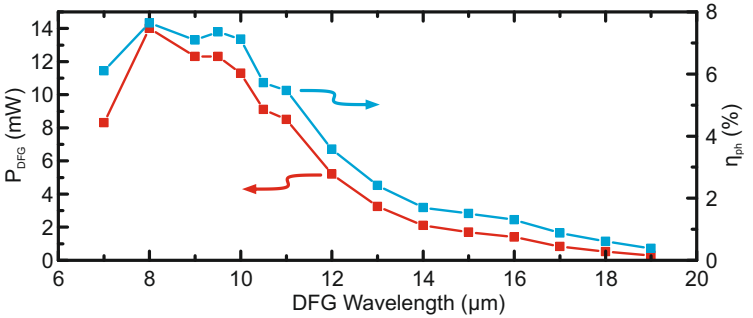

FIGURE 6.13. DFG output power and photon efficiency using a constant seed wavelength. Up to 7 % photon efficiency is achieved. 14 mW maximum output power is observed at 8 µm. As nearly constant pump and seed power is applied over the entire tuning range, the performance follows the GaSe transmission and gain spectrum.

All in all, a tuning range from 7 to 19 µm is achieved using a constant seed wavelength. In comparison to a signal-idler DFG lower output power and photon efficiency is achieved in the wavelength range below 13 µm. At longer wavelengths a higher efficiency and power is observed, as the applied input wavelength and power is beneficial. This is in accordance with the observation using a constant crystal orientation.

6.5 GENERAL OBSERVATIONS

At last, I would like to compare the presented DFG configurations more detailed. Fig. 6.14 summarizes the presented output power and photon efficiency. In general, the signal-idler DFG exhibits superior performance below 11 µm, but weak performance at longer wavelengths. The reasons for this observation is given in the following. First, the main experimental difference between the different configurations is the pump and seed wavelength. For the Dual OPO/OPA DFG they are well below 2 µm, which enables high input power,

as well as very close-lying wavelengths. The difference between pump and seed wavelength is illustrated in Fig. 6.15. The constant θ and constant λ_s configurations exhibit a crossing at 11 µm.
The effect of the shorter and closer pump and seed wavelength becomes obvious by considering the crystal parameters that describe the nonlinear interaction. As depicted in Fig. 6.16a)-c), the effective nonlinearity, figure of merit and the exponential gain coefficient are significantly higher for the Dual OPO/OPA DFG configurations (const. θ, const. λ_s). The higher nonlinearity was not expected, but this observation needs to be considered for future experiments. A higher figure of merit and exponential gain coefficient are achieved in consequence of their dependency on the nonlinearity, pump intensity (assuming 50 µm beam waist), and $\left(\lambda_s\right)^{-1}$, as derived in Eqs. (2.40b) and (2.50). Especially the significantly higher pump power is beneficial, which was one of the main reasons for these experiments. The experimental observations match these parameters very well.
However, from 5 to 10 µm we achieved maximum output power and photon efficiency using the signal-idler DFG. This is attributed to the lowest spatial walk-off as depicted in Fig. 6.16d). As the estimated beam waists are on the order 50 µm, the interaction length for the signal-idler DFG is on the order of 2 mm at 7 µm wavelength, whereas it is about 1.5 mm for the constant seed wavelength configuration. As the interaction length contributes quadratically to the photon efficiency (see Eqs. (2.42) and (2.43)), the constant seed wavelength is expected to exhibit at least 46 % lower efficiency. As visible in Fig. 6.14 the difference is even slightly larger. Thus, the increased interaction length between the pump and seed beams compensates the lower nonlinearity and gain. At around 11 µm the spatial walk-off of all configurations is comparable with respect to the beam waists. In consequence of the higher nonlinearity and gain, the Dual OPO/OPA DFGs become then superior. Please note that the temporal walk-off is negligible due to the long pulse durations.

In Fig. 6.15 a crossing between the Dual OPO/OPA DFG configurations is observed. This crossing is also observed in the effective nonlinearity and spatial walk-off (Fig. 6.16a), d)). From this I conclude that both parameters depend on the difference or product of pump and seed wavelengths. This needs to be investigated more detailed and is beyond the scope of this thesis.

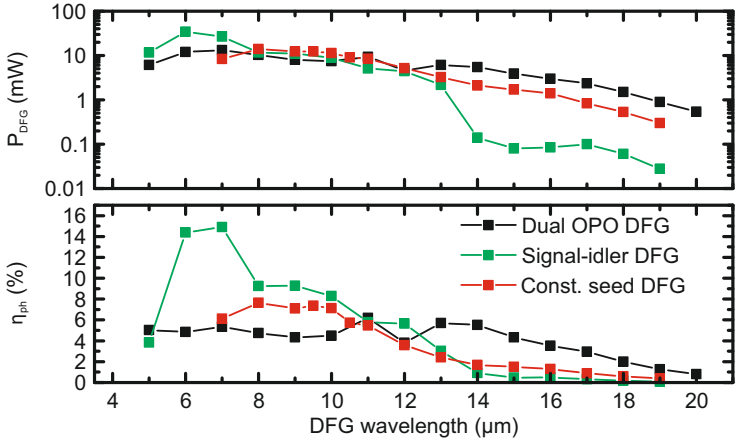

FIGURE 6.14. Summary of the generated mid-IR power and achieved photon efficiency of the presented configurations. Below 10 μm, the signal-idler DFG is superior. At higher wavelengths, the Dual OPO/OPA DFG configurations allow for higher power and efficiency.

6.6 CONCLUSION

In conclusion a new concept for difference frequency generation is introduced, which allows for an intrinsically stable beam pointing during wavelength tuning and high efficiency in the long mid-IR wavelength range. Compared to a signal-idler DFG setup higher

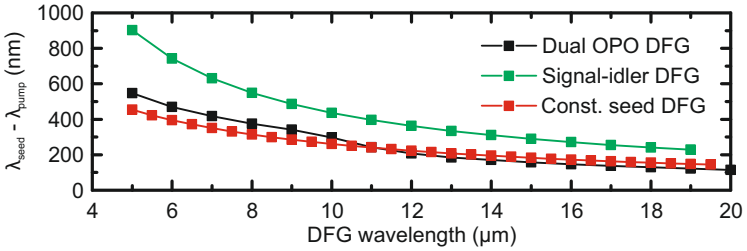

FIGURE 6.15. The Dual OPO/OPA DFG allows for shorter pump and signal wavelengths. The shorter the wavelengths, the closer the pump and seed wavelengths become. This enables higher nonlinearity, as depicted in Fig. 6.16.

output power is achieved from 11 µm and higher. Up to 20 µm the generated power remains in the mW range. GaSe is used as nonlinear gain medium, but other very promising crystals are presented as well. Their utilization can be chosen according to the desired application and wavelength range.

Due to the additional degree of freedom of two temporally synchronized, but independently wavelength-tunable input beams, this approach allows to choose higher or more favorable values of crystal parameters such as the effective nonlinearity, spatial walk-off, or dispersion. This can be investigated in future experiments.

Another interesting future experiment might be the application of a spectrally broadened seed beam. As visible in Fig. 6.4a), the seed wavelength only changes slightly between 12 to 20 µm and the pump beam and crystal angle are constant in the same range. By applying a supercontinuum seed in that range, a very broad DFG tuning range could be achieved by adjusting the temporal overlap of the pump and seed pulses.

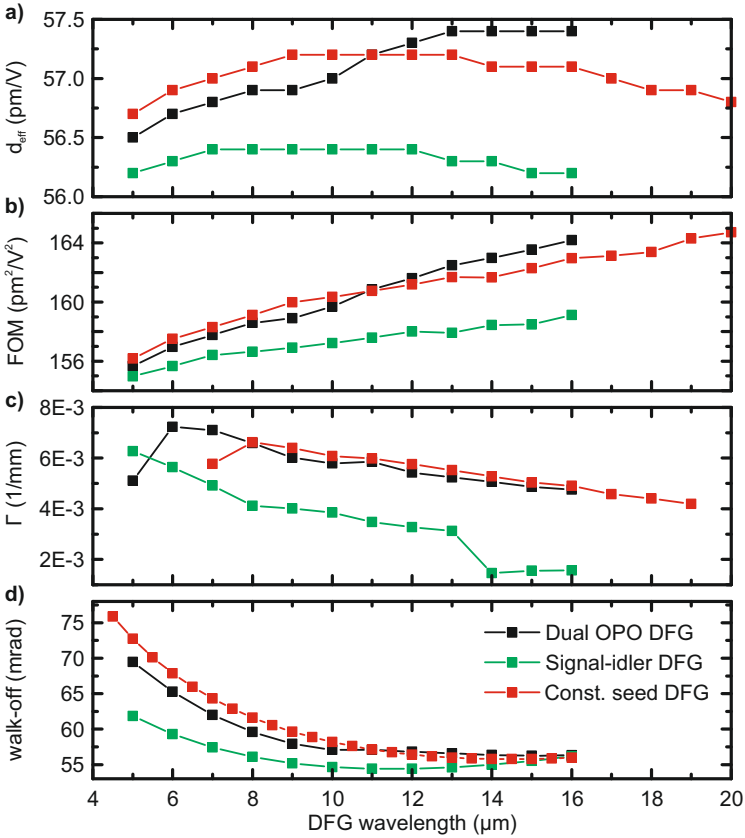

FIGURE 6.16. The Dual OPO/OPA DFG and constant seed DFG exhibit higher nonlinearity (**a)**), FOM (**b)**), and gain (**c)**) in general, compared to the signal-idler DFG. However, they exhibit significantly higher spatial walk-off below 11 µm (**d)**), which limits the achievable DFG power and efficiency in consequence of the reduced interaction length. Here, the signal-idler DFG is beneficial. The shorter the applied pump and seed wavelengths, the higher nonlinearity, gain and FOM.

7

CONCLUSIONS AND OUTLOOK

In this thesis the operating principle, implementation and further development of a parametric laser system for IR spectroscopy has been presented. The growing demand for faster, more sensitive, robust, compact and cost-effective spectroscopic systems is met by tunable, ultrafast laser sources, which extend the current limits given commonly used light sources, such as Globars or synchrotrons. Here, I focus on parametric MIR light sources consisting of several cascaded frequency conversion modules. This concept enables a broad applicable wavelength range from 1.33 to 20 µm with up to 125 cm^{-1} bandwidth ($1/e^2$), excellent long-term spectral and power stability, and high output power in the mW-range up to 20 µm wavelength.

The presented concept is based on a 1 µm solid-state laser. Typically, Yb:KGW or Yb:CALGO is employed as a laser gain medium. A promising alternative is Yb:CaF_2, exhibiting an order of magnitude longer excited state lifetime, a high thermal conductivity and a broad emission bandwidth. An oscillator is implemented to characterize the performance of this new gain medium. At 79.9 MHz pulse repetition rate 2.6 W output power is achieved. The nearly Fourier-limited, 194 fs-long pulses exhibit a bandwidth (FWHM) of 6.5 nm at 1050.1 nm. By reducing the repetition rate to 58.7 MHz a maximum output power of 3.15 W is measured, with a high slope efficiency of 38.6 %. In this configuration, a spectral bandwidth of 5.7 nm at 1050.1 nm central wavelength and 250 fs pulse duration was achieved.

Despite these promising results, I do not recommend Yb:CaF_2 as a solid-state laser gain medium, as it exhibits a very strong Q-switching tendency, which impedes stable soliton mode-locking. In general, stable mode-locking was achievable only in a narrow parameter range. Similar or better but more robust performance is achieved with Yb:KGW, Yb:KYW, or Yb:CALGO. However, Yb:CaF_2 is suited for thin-disk lasers or laser amplifiers that provide ultrashort pulses, as it exhibits low dispersion and allows for high energy storage.

In [12] we presented the above mentioned frequency conversion concept for the first time. This is further optimized to reach a broader spectral bandwidth. The system is realized by using a commercial 2.5 W pump laser, which exhibits 200 fs-long pulses. A tuning range from 1.33 to 8 µm (1250 to 7519 cm^{-1}) is demonstrated, with 350 mW power at 1.55 µm and 2.65 mW in the MIR at 5.5 µm wavelength. Up to 125 cm^{-1} bandwidth ($1/e^2$) are measured. The tuning range limit is currently given by the low power of the pump laser.
This setup is implemented for micro-FTIR spectroscopy. In standard FTIR spectrometers thermal light sources are applied, which only allow for a spatial resolution of several ten micrometer due to their low brilliance. In contrast, the presented laser source exhibits a 4-orders of magnitude higher brilliance of 1×10^{19} ph/s/mm²/sr/0.1%BW at 6 µm wavelength (1630 cm^{-1}). This allows for a high sensitivity and fast FTIR measurements, significantly exceeding the performance of the commonly used Globar or synchrotron light sources.

Nearly diffraction-limited FTIR mapping is presented in the fingerprint spectral region. At 7 µm (1435 cm^{-1}) wavelength samples are chemically analyzed and an exact image of the distribution of different molecules on the sample is created. Due to the broad laser bandwidth, different molecular species can be distinguished without spectral sweeping and stitching, as it is required with quantum

cascade lasers. A 150×150 µm² area is mapped in steps of 10 µm and 10×10 µm² pixel size. A pixel dwell time of 29 s/px is reached. In comparison, mapping is not feasible with a Globar at all. This is due to the high sensitivity that is reached by applying the laser. In the presented experiments, the minimum absorption, which can be detected with a single laser measurement is 0.47 %, compared to 6.4 % using the Globar.

With further advances of the measurement setup, we realized the in-vitro detection of different polypeptide conformations using attomolar concentrations. Thus, the current minimum polypeptide amount of several hundreds of thousands is reduced to about 1600. This is achieved by using surface-enhanced infrared absorption to excite and enhance the polypeptide resonances (amide-I). 0.23 % single-shot sensitivity and 0.015 % maximum sensitivity after 25 min integration time is reached. This is an improvement of 27 % compared to a synchrotron light source. Due to the high sensitivity and broad bandwidth of the laser, we determined the polypeptide structure within just 1 min in D_2O solution for optimum conditions. Integration times between 1 and 45 min are feasible in general, depending on the exact measurement conditions. In contrast, 65 min integration time was required using the synchrotron without reaching a comparable signal-to-noise ratio.

These applications show the capabilities of parametric laser sources for IR spectroscopy. They allow to significantly reduce the integration time compared to synchrotrons or Globars. Furthermore, their broad bandwidth avoids spectral sweeping and stitching, which can be extremely time-consuming. Due to the high sensitivity that is reached in both conventional IR spectroscopy and by means of SEIRA, the accessible time-scales are reduced to minutes or even seconds, which enables monitoring of dynamic processes. Due to their small footprint and relatively low-cost, such laser sources can enable research in every laboratory on a daily

basis, instead of waiting for expensive measurement time at synchrotron facilities.

A common issue of mid-infrared light generation is the intensive rotation of the nonlinear crystal for frequency tuning due to birefringent phase-matching. Stable beam-pointing over a broad tuning range is only achieved by actively compensating the beam offset due to the crystal rotation. However, this goes along with additional losses and sophisticated electronics and, or movable optics. Furthermore, common DFG setups exhibit low power and efficiency above 10 µm. These issues are addressed by presenting a new concept for difference frequency generation. Intrinsically stable beam-pointing is achieved from 11 to 20 µm and an up to 10-times higher photon efficiency is measured in the same range compared to the commonly used DFG concept, mixing signal and idler beams of an OPO or OPA. The presented concept allows for mW output power up to 20 µm wavelength. This is achieved by using two synchronously pumped OPO/OPAs to pump and seed a DFG setup. Thus, we are able to use pump and seed wavelengths between 1.4 and 1.95 µm, which enables an enhanced effective nonlinearity, higher input power, avoids atmospheric absorption windows, and allows for standard optical elements.

An outlook on the individual experiments is already given in the corresponding chapters. However, I would like to summarize possible future steps briefly.

The presented detection of polypeptide conformations has been done statically so-far. In a next step structural changes should be monitored, which allows to investigate the reaction of polypeptides or proteins to external stimuli.
Furthermore, the utilized setup is currently limited by the low power of the pump oscillator. To access longer wavelengths and

higher MIR power, a new pump laser with about 6 to 8 W power should be employed. Experiments on Glucose sensing, as it has been done by L. Kühner [95] in our labs, could be accomplished then, as they require wavelengths around 10 µm.

DFG light sources that reach the 10 to 20 µm range are based on $AgGaSe_2$ or GaSe crystals. However, the former exhibits a low damage threshold and limited availability, whereas the latter only allows for low efficiency and power due to significant spatial walk-off. Therefore new nonlinear gain media should be recommended. I conducted first calculations using $\mathbf{BaGa_4Se_7}$, a nonlinear gain medium allows for light generation up to 17 µm [96] and exhibits a promising figure of merit [97]. So far, it has not been applied for DFG with femtosecond pulse duration. Calculated phase-matching angles are shown in Figs. 7.1 and 7.2. We ordered and received a crystal, which is manufactured according to these calculations. This experiment should be conducted in the future.

At last, the experiments on the Dual OPO/OPA DFG concept showed that the 12 to 20 µm range can be covered by just adapting the seed wavelength. By using a supercontinuum seed with 1.65 µm central wavelength, broadband DFG should be feasible (assuming pulse compression after supercontinuum generation). By chirping the broadband seed, narrowband DFG could be realized using the temporal overlap between pump and seed pulses for wavelength tuning. In general, this concept could allow for a robust, alignment-free DFG source with intrinsically stable beam-pointing and broadband or narrowband output.

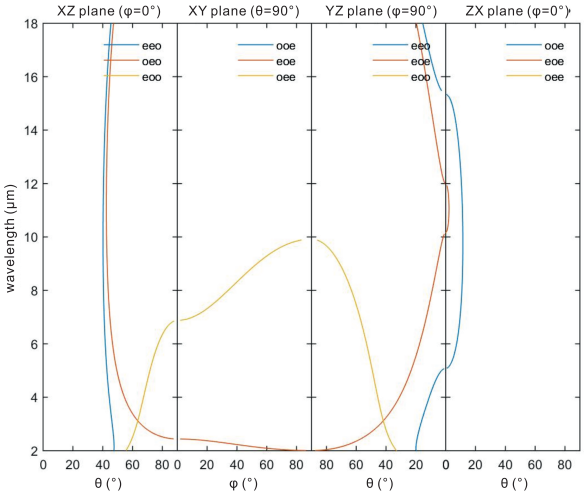

FIGURE 7.1. Phase-matching angles for different planes of $BaGa_4Se_7$.

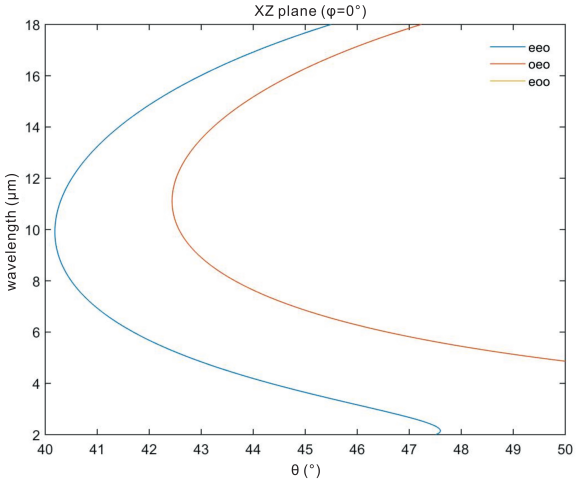

FIGURE 7.2. Detailed view on the phase-matching angle θ in the XZ plane of $BaGa_4Se_7$.

8

AUSFÜHRLICHE ZUSAMMENFASSUNG

Schnelle, verstimmbare MIR Laser haben in den letzten Jahren stark an Bedeutung gewonnen. Sie ermöglichen chemisch selektive und zeitaufgelöste Untersuchungen in den Material- und Biowissenschaften, genaue und hochaufgelöste Untersuchungen in der Medizin oder Qualitätsprüfungen in der Industrie. Vorteilhaft sind eine kurze Pulsdauer im Bereich von 100 fs, eine hohe Pulsrepetitionsrate (mehrere 10 MHz), geringes Rauschen und die Abdeckung eines großen spektralen Bereiches. Besonders wichtig ist die sogenannte *fingerprint region*, der Bereich zwischen 6 to 13 µm, in der die materialspezifischen Absorptionen liegen. Eine breit genutzte Spektroskopiemethode ist die Fourier-Transformations Infrarot (FTIR) Spektroskopie. Diese ermöglicht schnelle, breitbandige Messungen mit einer hohen spektralen Auflösung und hohem optischen Durchsatz, wodurch die Signalqualität entscheidend verbessert wird. Kommerzielle Systeme finden sowohl in der Wissenschaft als auch in der Industrie Einsatz. Jedoch zeigen kommerzielle FTIR-Spektrometer eine limitierte Sensitivität, die ihren Einsatz auf Proben mit Absorptionen im Bereich von mehreren Prozent und mehreren 10 µm räumlicher Ausdehnung begrenzt. Dies ist auf die typischerweise verwendeten thermischen Lichtquellen, die eine geringe Brillanz und Strahlqualität zeigen, zurückzuführen. Einige heutige Anwendungen erfordern jedoch eine höhere Sensitivität, um bspw. geringere Absorptionen oder Proben mit sub-µm Ausdehnung zu detektieren und kürzere Messzeiten zu erreichen. Dies kann durch die Verwendung eines Lasers anstelle des inkohärenten Globars erreicht werden. Der Einsatz in kommerziellen Systemen steht jedoch erst am Anfang und einfacher nutzbare und kompakte

Lasersysteme sind erforderlich.
Ziel dieser Arbeit ist die Entwicklung und Anwendung eines MIR-Lasers für die FTIR-Spektroskopie, der eine ausreichende Bandbreite und einen breiten nutzbaren spektralen Bereich aufweist. Um einen breiten Spektralbereich abzudecken, werden mehrere Frequenzkonversionsstufen, basierend auf einem Pumplaser mit 1 µm Wellenlänge, verwendet. Parameter wie Pulsdauer, Rauschen, erzielbare Ausgangsleistungen und der erreichbare Frequenzbereich werden durch diesen vorbestimmt. Daher ist die Wahl eines geeigneten Pumplasers essentiell und sollte sich immer an den Applikationsanforderungen orientieren. Viele grundlegende Eigenschaften sind durch das Lasermedium gegeben. In dieser Arbeit wird ein kommerzieller Yb:CALGO Oszillator als Pumpquelle verwendet. Da dieser jedoch nur eine geringe Pumpleistung bietet und dadurch der erzielte MIR Spektralbereich eingeschränkt ist, beschäftigt sich diese Arbeit auch mit der Erprobung eines alternativen, bisher kaum verwendeten Lasermaterials, Ytterbium-dotiertes Calciumfluorid Yb:CaF_2. Der sehr breite Emissionsquerschnitt erlaubt die Erzeugung von zeitlich kurzen und spektral breiten Pulsen. Aber besonders die sehr lange Lebensdauer des angeregten Laserniveaus bietet interessante Eigenschaften. Hierdurch kann viel Energie im Medium gespeichert werden, wodurch ein besonders effizienter Laserbetrieb und hohe Leistungen erzielt werden könnten. Weiterhin bietet Yb:CaF_2 eine hohe Zerstörschwelle und eine geringe Dispersion. Der Einsatz von Yb:CaF_2 als Lasermedium wird in dieser Arbeit untersucht, mit dem Ziel mehrere Watt Ausgangsleistung bei gleichzeitig kurzen Pulsen (<200 fs) und ca. 40-60 MHz Pulswiederholrate zu erreichen und damit eine Alternative für den, während den Spektroskopie-Experimenten, verwendeten Yb:CALGO Oszillator zu realisieren.
Um die vom Pumplaser bereitgestellte Leistung bis in den mittelinfraroten Frequenzbereich zu konvertieren, sind mindestens zwei bis drei Frequenzkonversionsstufen nötig. In einem ersten Schritt wird typischerweise ein kleiner Teil der verfügbaren Leistung in den nahinfraroten Bereich konvertiert. Dieses Licht wird häufig als

sogenannter Seed für einen Verstärker verwendet. Darin wird der Seedstrahl verstärkt und ein zweiter Laserstrahl, der sogenannte Idler, erzeugt. Gepumpt wird diese Stufe ebenfalls von dem 1 µm-Pumplaser. Die erzeugten Signal- und Idlerstrahlen werden dann gemischt und deren Differenzfrequenz erzeugt. Solche mehrstufigen System bieten den Vorteil einer hohen Puls-zu-Puls Stabilität, einer breiten Durchstimmbarkeit und hohen Ausgangsleistungen. Kritisch ist hierbei vor allem die Erzeugung des Seedstrahls, die großen Einfluss auf die Stabilität und die Durchstimmbarkeit des System hat. Das hier vorgestellte System verwendet hierfür einen sogenannten Faser-Feedback optisch parametrischen Oszillator (FFOPO). Dieser bietet eine exzellente, immanente Wellenlängen- und Leistungsstabilität, die durch die Verwendung einer single-mode Glasfaser erreicht wird. Durch die Faser wird das umlaufende Signal zeitlich leicht gestreckt, was den zeitlichen Überlapp mit dem Pumpstrahl bedeutend verbessert. Des Weiteren wird durch die Propagation in der Faser der Einfluss äußerer Bedingungen reduziert und die Grundfläche des OPOs signifikant verkleinert. Der verwendete FFOPO kann typischerweise von etwa 1.3 bis 2 µm durchgestimmt werden. Anschließend wird diese Strahlung in einem optisch parametrischen Verstärker (OPA) um ein Vielfaches verstärkt. Der erzeugte Idlerstrahl kann von 2.1 to 4.6 µm verstimmt werden.

Ein großer Teil dieser Arbeit beschäftigt sich mit der anschließenden Differenzfrequenzerzeugung (DFG) durch Mischen der Signal- und Idlerstrahlen. In vorangehenden Veröffentlichungen konnten wir mit diesem System verstimmbares Licht in einem Bereich von 5 to 20 µm (500-2000 cm^{-1}) bei bis zu 100 mW Leistung erzeugen [12]. Aufgrund der geringen Leistung des verwendeten Yb:CALGO Pumplasers bleibt der Spektralbereich hier auf maximal 8 µm begrenzt. Dafür ist dieses System für den Einsatz in der FTIR Spektroskopie optimiert und bietet eine erhöhte nutzbare Bandbreite von 125 cm^{-1} ($1/e^2$), sowie eine exzellente Langzeitstabilität. Über mehrere Stunden werden Fluktuationen der Zentralwellenlänge von etwa 0.013 %RMS beobachtet.

Im ersten Teil dieser Arbeit wird dieses System kurz vorgestellt. Besonders die Verwendung eines FFOPOs als Seedquelle ist ein wesentlicher Bestandteil des Designs. Anschließend wird das System für die FTIR Spektroskopie verwendet. Es werden verschiedene Experimente gezeigt, die nur durch die Verwendung unseres Lasersystem ermöglicht werden, und der Laser mit der typischerweise verwendeten thermischen Lichtquelle und einem Synchrotron verglichen.
In einem ersten Experiment wird eine chemische Abbildung einer 150x150 μm^2 großen Probe gemessen. Hierzu wird eine Pixelgröße von 10×10 μm^2 verwendet, um einzelne etwa 100 nm dicke Molekülschichten räumlich zu unterscheiden. Die detektierten Vibrationsbanden liegen bei etwa 1430 cm^{-1} (7 µm), es werden jedoch mehrere 10 cm^{-1} Bandbreite benötigt, um die verschiedenen Vibrationsbanden zu detektieren. Dieses Experiment dient der Charakterisierung der Laserquelle hinsichtlich Sensitivität und erzielbarer Messzeit, nutzbarer Bandbreite und Langzeitstabilität. Die interne thermische Lichtquelle des Spektrometers wird dabei als Referenz genutzt. Im direkten Vergleich wird mit dem Laser eine um eine Größenordnung höhere Sensitivität erreicht. Dadurch wird eine Detektion der Molekülabsorptionen von ca. 1 % innerhalb von Minuten möglich.
Anschließend wird das optimierte FTIR System zur Detektion von Proteinstrukturen eingesetzt. Veränderungen der Proteinstrukturen, sogenannte Faltungen, werden für zahlreiche neurodegenerative Krankheiten verantwortlich gemacht. Zur Erforschung dieser Prozesse müssen geringste Proteinmengen, idealerweise einzelne Proteine, in-vitro detektiert und die Reaktion auf externe Stimuli beobachtet werden können. Dies erfordert höchst sensitive Messungen bei einer räumlicher Auflösung im nm-Bereich, was über das Beugungslimit hinausgeht. Solche Anwendungen sind mit thermischen Lichtquellen nicht oder nur mit sehr hohen Proteinmengen und langen Messzeiten realisierbar. Die Kombination aus FTIR und oberflächenverstärkter Infrarot-Absorptionsspektroskopie (SEIRA), d.h. die Verwendung plasmonischer Strukturen zur Verstärkung der

Proteinsignale, ermöglichte bereits eine signifikante Reduzierung der Proteinkonzentration. Es werden jedoch weiterhin mehrere 100 000 Proteine benötigt, um ein ausreichend starkes Signal zu detektieren und kurze Messzeiten zu erreichen, die die Beobachtung dynamischer Prozesse erst erlauben. Zur plasmonischen Signalverstärkung werden typischerweise große Antennenfelder verwendet. Ziel dieses Experimentes ist es die erforderliche Proteinkonzentration und Messzeit signifikant zu reduzieren. Durch die hohe Sensitivität kann anstelle großer Antennenfelder eine einzelne Nanoantenne zu Verstärkung des Proteinsignals verwendet werden. Dadurch reduziert sich die Zahl detektierter Moleküle auf ca. 1600, was attomolaren Konzentrationen entspricht. Eine erfolgreiche Detektion der Polypeptidstruktur ist innerhalb von minimal einer Minute möglich. Zur Validierung der Ergebnisse werden identische Messungen mit einem Globar, sowie einer Synchrotronquelle durchgeführt. Eine Detektion der Proteinstruktur ist hierbei mit dem Globar trotz bis zu 9 Stunden Integrationszeit nicht möglich. Auch mit dem Synchrotron wird die Struktur nur nach 65 Minuten und bei hohem Rauschen sichtbar. Diese Messungen zeigen das Potential einer Laserquelle für die MIR-Spektroskopie. Dynamische Veränderung der Molekülstruktur können so in kurzer Zeit unter in-vitro Bedingungen beobachtet werden und es werden Anwendungen wie die Untersuchung von Proteinfaltungen im Alltag möglich.

Im abschließenden Kapitel wird ein neues DFG Konzept vorgestellt, das zuvor beobachtete Probleme umgeht. So geht eine Wellenlängenänderung bei einer DFG, die Signal und Idlerstrahlen mischt, mit einem Strahlversatz einher, da der Winkel des nichtlinearen Mediums angepasst werden muss. Dieser Strahlversatz erschwert die Einkopplung in Spektroskopiesysteme und muss kompensiert werden. Weiterhin weist eine Signal-Idler DFG typischerweise eine stark abnehmende Effizienz und Ausgangsleistung oberhalb von 10 µm auf. Dies ist auf den Betrieb des FFOPOs und OPAs nahe der Entartung von Signal und Idler zurückzuführen. Beide Probleme werden mit dem vorgestellten Konzept effizient gelöst

und eine um eine Größenordnung höhere Effizienz oberhalb von 10 µm wird erreicht. Unser Konzept erlaubt einen konstanten DFG-Kristallwinkel zwischen 11 und 20 µm, wodurch der erzeugte MIR Strahl immanent stabil ist und auf eine aktive Strahlversatzkompensation verzichtet werden kann. Weitere DFG Konzepte können mit diesem Aufbau realisiert und das Gain-Verhalten des verwendeten nichtlinearen Mediums untersucht werden. Die so gewonnenen Beobachtungen erlauben das Design effizienterer DFG-Stufen, die optimal auf verschiedene Anwendungen angepasst sind.

LIST OF ACRONYMS

κ	thermal conductivity
σ_{abs}	absorption cross-section
σ_{em}	emission cross-section
τ_L	lifetime of the upper laser level
τ_p	pulse duration
AGSe	$AgGaSe_2$ - silver gallium diselenide
AOI	angle of incidence
AOM	acousto-optic modulator
CW	continuous wave
DFG	Differenz Frequenz Erzeugung
DFG	difference frequency generation
FFOPO	Faser-Feedback optisch parametrischer Oszillator
FFOPO	fiber-feedback optical parametric oscillator
FOM	figure of merit
FTIR	Fourier-Transformations infrarot Spektroskopie/Spektrometer
FTIR	fourier-transform Infrared (spectrometer/spectroscopy)
FWHM	full width at half maximum
GDD	group delay dispersion
GTI	gires tournois interferometer
GVD	group velocity dispersion
GVM	group-velocity mismatch
KLM	kerr-lens mode-locking

MIR	mid-infrared
MUA	11-mercaptoundecanoic acid
MUoL	11-mercaptoundecanol
NA	numerical aperture
NIR	near-infrared
OPA	optisch parametrischer Verstärker
OPA	optical parametric amplification
OPG	optical parametric generation
OPO	optical parametric oscillation
PLL	poly-L-lysine
PPLN	periodically-poled lithium niobate
QCL	quantum cascade laser
QPM	quasi-phase-matching
RFL	reflected focal length
RMS	root-mean-square
ROC	radius of curvature
s-SNOM	scattering-type scanning near-field optical microscopy
SAM	saturable absorber mirror
SDS	sodium dodecyl sulfate
SEIRA	surface enhanced infrared absorption
SESAM	semiconductor saturable absorber mirror
SFG	sum frequency generation
SHG	second harmonic generation
SNR	signal-to-noise ratio
SPM	self-phase modulation
STED	stimulated emission depletion
TBP	time-bandwidth product

LIST OF FIGURES

LIST OF TABLES

BIBLIOGRAPHY

[1] R. J. Glauber: *Nobel lecture: One hundred years of light quanta.* Reviews of Modern Physics **78**, 1267–1278 (2006). DOI 10.1103/RevModPhys.78.1267, cit. on p. 1.

[2] J. L. Hall: *Nobel lecture: Defining and measuring optical frequencies.* Reviews of Modern Physics **78**, 1279–1295 (2006). DOI 10.1103/RevModPhys.78.1279, cit. on p. 1.

[3] T. W. Hänsch: *Nobel lecture: Passion for precision.* Reviews of Modern Physics **78**, 1297–1309 (2006). DOI 10.1103/RevModPhys.78.1297, cit. on p. 1.

[4] P. B. Fellgett: *On the ultimate sensitivity and practical performance of radiation detectors.* Journal of the Optical Society of America **39**, 970–976 (1949). DOI 10.1364/JOSA.39.000970, cit. on pp. 1, 38, 66.

[5] P. Jacquinot: *New developments in interference spectroscopy.* Rep. Prog. Phys. **23**, 267–312 (1960). DOI 10.1088/0034-4885/77/5/056502, cit. on pp. 1, 38, 66.

[6] P. Connes and G. Michel: *Astronomical Fourier Spetroscopy.* Annu. Rev. Astron. Astrophys. **8**, 209–230 (1970). DOI 10.1364/ao.14.002067, cit. on pp. 1, 38, 66.

[7] J. Mandon, G. Guelachvili, and N. Picqué: *Fourier transform spectroscopy with a laser frequency comb.* Nature Photonics **3**, 99–102 (2009). DOI 10.1038/nphoton.2008.293, cit. on pp. 2, 106.

[8] I. Coddington, N. Ewbury, and W. Swann: *Dual-comb spectroscopy.* Optica **3**, 414–426 (2016). Cit. on pp. 2, 106.

[9] C. R. Petersen, U. Møller, I. Kubat, B. Zhou, S. Dupont, J. Ramsay, T. Benson, S. Sujecki, N. Abdel-Moneim, Z. Tang, D. Furniss, A. Seddon, and O. Bang: *Mid-infrared supercontinuum covering the* 1.4 *to* 13.3 µm *molecular fingerprint region using ultra-high NA chalcogenide step-index fibre*. Nature Photonics **8**, 830–834 (2014). DOI 10.1038/nphoton.2014.213, cit. on p. 2.

[10] R. F. Curl, F. Capasso, C. Gmachl, A. A. Kosterev, B. McManus, R. Lewicki, M. Pusharsky, G. Wysocki, and F. K. Tittel: *Quantum cascade lasers in chemical physics*. Chemical Physics Letters **487**, 1–18 (2010). DOI 10.1016/j.cplett.2009.12.073, cit. on pp. 2, 66, 106.

[11] A. Hasenkampf, N. Kröger, A. Schönhals, W. Petrich, and A. Pucci: *Surface-enhanced mid-infrared spectroscopy using a quantum cascade laser*. Optics Express **23**, 5670–5680 (2015). DOI 10.1364/oe.23.005670, cit. on pp. 2, 106.

[12] T. Steinle, F. Mörz, A. Steinmann, and H. Giessen: *Ultra-stable high average power femtosecond laser system tunable from* 1.33 *to* 20 µm. Optics Letters **41**, 4863–4866 (2016). DOI 10.1364/ol.41.004863, cit. on pp. 2, 3, 5, 36, 67, 68, 105, 106, 117, 130, 137.

[13] R. W. Boyd: *Nonlinear Optics*, 3rd edition, Academic Press (), 2008. ISBN 9780123694706, cit. on pp. 7, 26–28, 35.

[14] M. Eichhorn: *Laserphysik*, Springer Spektrum (), 2013. ISBN 9783642326479, cit. on pp. 13, 14.

[15] W. Koechner: *Solid-State Laser Engineering*, 6th edition, Springer (), 2006. ISBN 9780387290942, cit. on pp. 15, 17.

[16] U. Keller, K. J. Weingarten, F. X. Kärtner, D. Kopf, B. Braun, I. D. Jung, R. Fluck, C. Hönninger, N. Matuschek, and J. Aus Der Au: *Semiconductor saturable absorber mirrors (SESAM's) for femtosecond to nanosecond pulse generation in solid-state lasers*. IEEE Journal on Selected Topics in Quantum Electronics **2**, 435–451 (1996).
DOI 10.1109/2944.571743, cit. on pp. 19, 20.

[17] R. Paschotta and U. Keller: *Passive mode locking with slow saturable absorbers*. Applied Physics B: Lasers and Optics **73**, 653–662 (2001).
DOI 10.1007/s003400100726, cit. on pp. 20–22.

[18] F. X. Kärtner, I. D. Jung, and U. Keller: *Soliton mode-locking with saturable absorbers*. IEEE Journal on Selected Topics in Quantum Electronics **2**, 540–556 (1996).
DOI 10.1109/2944.571754, cit. on pp. 21, 22.

[19] R. Paschotta: *RP Photonics Encyclopedia - Q-switched Mode Locking*, https://www.rp-photonics.com/q{_}switched{_}mode{_}locking.html (visited on June 19, 2020).
Cit. on p. 23.

[20] C. Hönninger, R. Paschotta, F. Morier-Genoud, M. Moser, and U. Keller: *Q -switching stability limits of continuous-wave passive mode locking*. **16**, 46–56 (1999).
Cit. on pp. 23, 24, 48.

[21] H. A. Haus: *Parameter Ranges for CW Passive Mode Locking*. IEEE Journal of Quantum Electronics **12**, 169–176 (1976).
DOI 10.1109/JQE.1976.1069112, cit. on p. 23.

[22] J. J. Degnan: *Optimization of Passively Q-Switched Lasers*. IEEE Journal of Quantum Electronics **31**, 1890–1901 (1995).
DOI 10.1109/3.469267, cit. on p. 23.

[23] G. J. Spühler, R. Paschotta, R. Fluck, B. Braun, M. Moser, G. Zhang, E. Gini, and U. Keller: *Experimentally confirmed design guidelines for passively Q-switched microchip lasers using semiconductor saturable absorbers: errata*. Journal of the Optical Society of America B **16**, 376–388 (1999). DOI 10.1364/josab.18.000886, cit. on p. 23.

[24] F. Mörz, T. Steinle, H. Linnenbank, A. Steinmann, and H. Giessen: *Alignment-free difference frequency light source tunable from* 5 *to* 20 µm *by mixing two independently tunable OPOs*. Optics Express **28**, 11883–11891 (2020). DOI https://doi.org/10.1364/OE.385838, cit. on pp. 29, 36, 105, 109, 113–119, 121.

[25] V. G. Dmitriev, G. G. Gurzadyan, and D. N. Nikogosyan: *Handbook of Nonlinear Optical Crystals*, 2nd edition, Springer (), 1997. ISBN 9783662141021, cit. on pp. 29, 35.

[26] G. Cerullo and S. De Silvestri: *Ultrafast optical parametric amplifiers*. Review of Scientific Instruments **74**, 1–18 (2003). DOI 10.1063/1.1523642, cit. on pp. 32, 33.

[27] V. Petrov: *Frequency down-conversion of solid-state laser sources to the mid-infrared spectral range using non-oxide nonlinear crystals*. Progress in Quantum Electronics **42**, 1–106 (2015). DOI 10.1016/j.pquantelec.2015.04.001, cit. on pp. 34, 36.

[28] G. D. Boyd and D. A. Kleinman: *Parametric interaction of focused Gaussian light beams*. Journal of Applied Physics **39**, 3597–3639 (1968). DOI 10.1063/1.1656831, cit. on p. 35.

[29] T. Steinle: *Ultrafast near- and mid-infrared laser sources for linear and nonlinear spectroscopy*. PhD thesis, University of Stuttgart, 2016. Cit. on pp. 37, 69, 75.

[30] F. Mörz, T. Steinle, A. Steinmann, and H. Giessen: *Multi-Watt femtosecond optical parametric master oscillator power amplifier at* 43 MHz. Optics Express **23**, 23960–23967 (2015).
DOI 10.1364/oe.23.023960, cit. on pp. 38, 69.

[31] J. Krauth, T. Schumacher, J. Defrance, B. Metzger, M. Lippitz, T. Weiss, H. Giessen, and M. Hentschel: *Nonlinear Spectroscopy on the Plasmonic Analog of Electromagnetically Induced Absorption: Revealing Minute Structural Asymmetries.* ACS Photonics **6**, 2850–2859 (2019).
DOI 10.1021/acsphotonics.9b00938, cit. on p. 38.

[32] J. Krauth, H. Giessen, and M. Hentschel: *Wavelength-Dependent Third-Harmonic Generation in Plasmonic Gold Nanoantennas: Quantitative Determination of the d-Band Influence.* ACS Photonics **5**, 1863–1870 (2018).
DOI 10.1021/acsphotonics.8b00079, cit. on pp. 38, 42, 91, 93, 96.

[33] J. Karst, F. Sterl, H. Linnenbank, T. Weiss, M. Hentschel, and H. Giessen: *Watching In-Situ the Hydrogen Diffusion Dynamics in Magnesium on the Nanoscale.* Science Advances **6** (2020).
Cit. on p. 38.

[34] F. E. Robles, H. Linnenbank, F. Mörz, P. Ledwig, T. Steinle, and H. Giessen: *Coherently broadened, high-repetition-rate laser for stimulated Raman scattering–spectroscopic optical coherence tomography.* Optics Letters **44**, 291–294 (2019).
DOI 10.1364/ol.44.000291, cit. on p. 38.

[35] F. Sterl, H. Linnenbank, T. Steinle, F. Mörz, N. Strohfeldt, and H. Giessen: *Nanoscale Hydrogenography on Single Magnesium Nanoparticles.* Nano Letters **18**, 4293–4302 (2018).
DOI 10.1021/acs.nanolett.8b01277, cit. on pp. 38, 73, 106.

[36] T. Steinle, J. N. Greiner, J. Wrachtrup, H. Giessen, and I. Gerhardt: *Unbiased all-optical random-number generator*. Physical Review X **7**, 041050 (2017).
DOI 10.1103/PhysRevX.7.041050, cit. on p. 38.

[37] T. Steinle, V. Kumar, M. Floess, A. Steinmann, M. Marangoni, C. Koch, C. Wege, G. Cerullo, and H. Giessen: *Synchronization-free all-solid-state laser system for stimulated Raman scattering microscopy*. Light Sci Appl. **5**, e16149 (2016).
Cit. on p. 38.

[38] T. Steinle, F. Neubrech, A. Steinmann, X. Yin, and H. Giessen: *Mid-infrared Fourier-transform spectroscopy with a high-brilliance tunable laser source: investigating sample areas down to* 5 µm *diameter*. Optics Express **23**, 11105 (2015).
DOI 10.1364/oe.23.011105, cit. on pp. 38, 42, 66, 89.

[39] M. C. Martin, U. Schade, P. Lerch, and P. Dumas: *Recent applications and current trends in analytical chemistry using synchrotron-based Fourier-transform infrared microspectroscopy*. Trends in Analytical Chemistry **29**, 453–463 (2010).
DOI 10.1016/j.trac.2010.03.002, cit. on p. 42.

[40] H. Timmers, A. Kowligy, A. Lind, F. C. Cruz, N. Nader, M. Silfies, G. Ycas, T. K. Allison, P. G. Schunemann, S. B. Papp, and S. A. Diddams: *Molecular fingerprinting with bright, broadband infrared frequency combs*. Optica **5**, 727–732 (2018).
DOI 10.1364/OPTICA.5.000727, cit. on pp. 42, 87, 106.

[41] F. Neubrech, C. Huck, K. Weber, A. Pucci, and H. Giessen: *Surface-enhanced infrared spectroscopy using resonant nanoantennas*. Chemical Reviews **117**, 5110–5145 (2017).
DOI 10.1021/acs.chemrev.6b00743, cit. on pp. 44, 45, 87.

[42] P. Alonso-González, P Albella, F Neubrech, C Huck, J Chen, F Golmar, F. Casanova, L. E. Hueso, A. Pucci, J. Aizpurua, and R. Hillenbrand: *Experimental Verification of the Spectral Shift between Near- and Far-Field Peak Intensities of Plasmonic Infrared Nanoantennas*. Physical Review Letters **110**, 203902 (2013).
DOI 10.1103/PhysRevLett.110.203902, cit. on p. 45.

[43] T. Neuman, C. Huck, J. Vogt, F. Neubrech, R. Hillenbrand, J. Aizpurua, and A. Pucci: *Importance of Plasmonic Scattering for an Optimal Enhancement of Vibrational Absorption in SEIRA with Linear Metallic Antennas*. Journal of Physical Chemistry C **119**, 26652–26662 (2015).
DOI 10.1021/acs.jpcc.5b08344, cit. on p. 45.

[44] R. Adato, S. Aksu, and H. Altug: *Engineering mid-infrared nanoantennas for surface enhanced infrared absorption spectroscopy*. Materials Today **18**, 436–446 (2015).
DOI 10.1016/j.mattod.2015.03.001, cit. on p. 45.

[45] J. Vogt, C. Huck, F. Neubrech, A. Toma, D. Gerbert, and A. Pucci: *Impact of the plasmonic near- and far-field resonance-energy shift on the enhancement of infrared vibrational signals*. Physical Chemistry Chemical Physics **17**, 21169–21175 (2014).
DOI 10.1039/c4cp04851b, cit. on pp. 45, 100.

[46] J. Zuloaga, E. Prodan, and P. Nordlander: *Quantum Plasmonics : Optical Properties and Tunability of Metallic Nanorods*. ACS Nano **4**, 5269–5276 (2010).
DOI 10.1021/nn101589n, cit. on p. 45.

[47] U. Morgner, F. Kärtner, S. Cho, Y. Chen, H. Haus, J. Fujimoto, and E. P. Ippen: *Sub-two-cycle pulses from a Kerr-lens mode-locked Ti:sapphire laser*. Optics Letters **24**, 411–413 (1999).
Cit. on p. 47.

[48] D. H. Sutter, G. Steinmeyer, L. Gallmann, N. Matuschek, F. Morier-Genoud, U. Keller, V. Scheuer, G. Angelow, and T. Tschudi: *Semiconductor saturable-absorber mirror–assisted Kerr-lens mode-locked Ti:sapphire laser producing pulses in the two-cycle regime*. Optics Letters **24**, 631–633 (1999). DOI 10.1364/ol.24.000631, cit. on p. 47.

[49] G. Machinet, P. Sevillano, F. Guichard, R. Dubrasquet, P. Camy, J. Doualan, and R. Moncorgé: *Kerr-lens mode-locked Yb : CaF_2 oscillator*. Optics Letters **38**, 4008–4010 (2013). Cit. on p. 47.

[50] P. P. Sorokin and M. J. Stevenson: *Solid-State Optical Maser Using Divalent Samarium in Calcium Fluoride*. IBM Journal of Research and Development **5**, 56–58 (1961). DOI 10.1147/rd.51.0056, cit. on p. 48.

[51] M. Siebold, S. Bock, U. Schramm, B. Xu, J. L. Doualan, P. Camy, and R. Moncorgé: *Yb:CaF_2-a new old laser crystal*. Applied Physics B: Lasers and Optics **97**, 327–338 (2009). DOI 10.1007/s00340-009-3701-y, cit. on pp. 48, 58, 60.

[52] V. Petit, P. Camy, J.-L. Doualan, X. Portier, and R. Moncorgé: *Spectroscopy of Yb^{3+}:CaF_2 : From isolated centers to clusters*. Physical Review B **78**, 085131 (2008). DOI 10.1103/PhysRevB.78.085131, cit. on p. 48.

[53] Electro-Optics-Technology-Inc.: *Yb:CALGO - Ytterbium-doped Calcium Aluminum Gadolinium Oxide*, https://www.eotech.com/cart/146/laser-crystals/yb:calgo---ytterbium-doped-calcium-aluminum-gadolinium-oxide (visited on Apr. 23, 2020). Cit. on pp. 48, 49.

[54] Laser-Crylink: *Yb: $CaGdAlO_4$ (Yb: CALGO) – Yb-dotierte Kristalle für Hochleistungs- und ultrakurze (Femtosekunden-) Laser*, https://www.laser-crylink.com/de/laserprodukte/laserkristall/ybcalgo/ (visited on Apr. 23, 2020). Cit. on pp. 48, 49.

[55] A. Lucca, G. Debourg, M. Jacquemet, F. Druon, F. Balembois, P. Georges, P. Camy, J. L. Doualan, and R. Moncorgé: *High-power diode-pumped Yb^{3+}:CaF_2 femtosecond laser*. Optics Letters **29**, 2767–2769 (2004). DOI 10.1364/ol.29.002767, cit. on p. 49.

[56] F. Friebel, F. Druon, J. Boudeile, D. N. Papadopoulos, M. Hanna, P. Georges, P. Camy, J. L. Doualan, A. Benayad, R. Moncorgé, C. Cassagne, and G. Boudebs: *Diode-pumped 99 fs Yb:CaF_2 oscillator*. Optics Letters **34**, 1474–1476 (2009). DOI 10.1364/ol.34.001474, cit. on p. 49.

[57] F. Lücking: *Ursache der Pulsdauerbegrenzung in solitär modengekoppelten Festkörperlasern*. PhD thesis, Leibniz-Universität Hannover, 2009. Cit. on p. 54.

[58] G. Machinet, G. Andriukaitis, P. Sévillano, J. Lhermite, D. Descamps, A. Pugžlys, A. Baltuška, and E. Cormier: *High-gain amplification in Yb:CaF_2 crystals pumped by a high-brightness Yb-doped 976 nm fiber laser*. Applied Physics B: Lasers and Optics **111**, 495–500 (2013). DOI 10.1007/s00340-013-5363-z, cit. on p. 62.

[59] P. Sevillano, P. Camy, J. Doualan, R. Moncorgé, D. Descamps, and E. Cormier: 130 fs – *Multiwatt Yb:CaF_2 regenerative amplifier pumped by a fiber laser*, ATh4A.5 (2016). DOI 10.1364/assl.2016.ath4a.5, cit. on p. 62.

[60] M. Siebold, M. Hornung, R. Boedefeld, S. Podleska, S. Klingebiel, C. Wandt, F. Krausz, S. Karsch, R. Uecker, A. Jochmann, J. Hein, and M. C. Kaluza: *Terawatt diode-pumped Yb:CaF_2 laser*. Optics Letters **33**, 2770–2772 (2008). Cit. on p. 62.

[61] M. Siebold, M. Hornung, S. Bock, J. Hein, M. C. Kaluza, J. Wemans, and R. Uecker: *Broad-band regenerative laser amplification in ytterbium-doped calcium fluoride (Yb:CaF_2)*. Applied Physics B: Lasers and Optics **89**, 543–547 (2007). DOI 10.1007/s00340-007-2834-0, cit. on p. 62.

[62] K. S. Wentsch, B. Weichelt, S. Günster, F. Druon, P. Georges, M. A. Ahmed, and T. Graf: *Yb:CaF_2 thin-disk laser*. Optics Express **22**, 1524 (2014). DOI 10.1364/oe.22.001524, cit. on p. 62.

[63] B. Dannecker, X. Délen, K. S. Wentsch, B. Weichelt, C. Hönninger, A. Voss, M. A. Ahmed, and T. Graf: *Passively mode-locked Yb:CaF_2 thin-disk laser*. Optics Express **22**, 22278 (2014). DOI 10.1364/OE.22.022278, cit. on p. 62.

[64] F. Mörz, R. Semenyshyn, T. Steinle, F. Neubrech, U. Zschieschang, H. Klauk, A. Steinmann, and H. Giessen: *Nearly diffraction limited FTIR mapping using an ultrastable broadband femtosecond laser tunable from* 1.33 *to* 8 µm. Optics Express **25**, 32355–32363 (2017). DOI 10.1364/oe.25.032355, cit. on pp. 65, 68, 72, 74, 76–79, 81, 105, 106.

[65] P. R. Griffiths and J. A. de Haseth: *Fourier Transform Infrared Spectrometry*, 2nd edition, Wiley Interscience (), 2007. ISBN 978-0-471-19404-0, cit. on p. 66.

[66] M. Jäckle: *Efficient frequency conversion in the near- and mid-IR for large bandwidths and short pulse durations*, University of Stuttgart, 2019. Cit. on p. 71.

[67] R. V. Semenyshyn: *Mid-infrared resonant nanostructures for in-vitro monitoring of polypeptides*. PhD thesis, University of Stuttgart, 2019. Cit. on pp. 86, 91.

[68] R. Semenyshyn, F. Mörz, T. Steinle, M. Ubl, M. Hentschel, F. Neubrech, and H. Giessen: *Pushing down the Limit: In Vitro Detection of a Polypeptide Monolayer on a Single Infrared Resonant Nanoantenna.* ACS Photonics **6**, 2636–2642 (2019).
DOI 10.1021/acsphotonics.9b01125, cit. on pp. 86, 88, 90–92, 94, 95, 98, 100–102, 105, 106.

[69] T. P. Knowles, M. Vendruscolo, and C. M. Dobson: *The amyloid state and its association with protein misfolding diseases.* Nature Reviews Molecular Cell Biology **15**, 384–396 (2014).
DOI 10.1038/nrm3810, cit. on p. 86.

[70] D. Etezadi, J. B. Warner, H. A. Lashuel, and H. Altug: *Real-time in situ secondary structure analysis of protein monolayer with mid-infrared plasmonic nanoantennas.* ACS Sensors **3**, 1109–1117 (2018).
DOI 10.1021/acssensors.8b00115, cit. on pp. 86, 87, 89, 95.

[71] R. Semenyshyn, M. Hentschel, C. Stanglmair, T. Teutsch, C. Tarin, C. Pacholski, H. Giessen, and F. Neubrech: *In-Vitro Monitoring Conformational Changes of Polypeptide Monolayers Using Infrared Plasmonic Nanoantennas.* Nano Letters **19**, 1–7 (2019).
DOI 10.1021/acs.nanolett.8b02372, cit. on pp. 86, 87, 89, 91, 95.

[72] I. Amenabar, S. Poly, W. Nuansing, E. H. Hubrich, A. A. Govyadinov, F. Huth, R. Krutokhvostov, L. Zhang, M. Knez, J. Heberle, A. M. Bittner, and R. Hillenbrand: *Structural analysis and mapping of individual protein complexes by infrared nanospectroscopy.* Nature Communications **4** (2013).
DOI 10.1038/ncomms3890, cit. on pp. 86, 106.

[73] S. Amarie, T. Ganz, and F. Keilmann: *Mid-infrared near-field spectroscopy.* Optics Express **17**, 21794–21801 (2009).
Cit. on p. 86.

[74] A. V. Zayats and D. Richards: *Nano-Optics and Near-Field Optical Microscopy*, 1st edition, Artech House (), 2008. ISBN 9781596932838, cit. on p. 86.

[75] F. Huth: *Nano-FTIR - Nanoscale Infrared Near-Field Spectroscopy*. PhD thesis, CIC NanoGUNE, San Sebastian, 2015.
Cit. on p. 86.

[76] F. Huth, M. Schnell, J. Wittborn, N. Ocelic, and R. Hillenbrand: *Infrared-spectroscopic nanoimaging with a thermal source*. Nature Materials **10**, 352–356 (2011). DOI 10.1038/nmat3006, cit. on p. 86.

[77] F. Huth, A. Govyadinov, S. Amarie, W. Nuansing, F. Keilmann, and R. Hillenbrand: *Nano-FTIR absorption spectroscopy of molecular fingerprints at 20 nm spatial resolution*. Nano Letters **12**, 3973–3978 (2012). DOI 10.1021/nl301159v, cit. on p. 86.

[78] X. G. Xu, M. Rang, I. M. Craig, and M. B. Raschke: *Pushing the sample-size limit of infrared vibrational nanospectroscopy: From monolayer toward single molecule sensitivity*. Journal of Physical Chemistry Letters **3**, 1836–1841 (2012). DOI 10.1021/jz300463d, cit. on p. 86.

[79] C. Petibois, G. Déléris, M. Piccinini, M. Cestelli-Guidi, and A. Marcelli: *A bright future for synchrotron imaging*. Nature Photonics **3**, 179–179 (2009). DOI 10.1038/nphoton.2009.31, cit. on pp. 87, 89.

[80] P. Dumas, F. Polack, B. Lagarde, O. Chubar, J. L. Giorgetta, and S. Lefrançois: *Synchrotron infrared microscopy at the French Synchrotron Facility SOLEIL*. Infrared Physics and Technology **49**, 152–160 (2006). DOI 10.1016/j.infrared.2006.01.030, cit. on pp. 87, 89.

[81] P. Lerch, L. Quaroni, J. Wambach, J. Schneider, D. B. Armstrong, D. Rossetti, F. L. Mueller, P. Peier, V. Schlott, L. Carroll, P. Friedli, H. Sigg, S. Stutz, and M. Tran: *IR beamline at the Swiss Light Source*. Journal of Physics: Conference Series **359**, 012003 (2012). DOI 10.1088/1742-6596/359/1/012003, cit. on p. 88.

[82] D. Etezadi, J. B. Warner, F. S. Ruggeri, G. Dietler, H. A. Lashuel, and H. Altug: *Nanoplasmonic mid-infrared biosensor for in vitro protein secondary structure detection.* Light: Science and Applications **6**, e17029–10 (2017). DOI 10.1038/lsa.2017.29, cit. on p. 89.

[83] M. A. Fallah, C. Stanglmair, C. Pacholski, and K. Hauser: *Devising Self-Assembled-Monolayers for Surface-Enhanced Infrared Spectroscopy of pH-Driven Poly-l-lysine Conformational Changes*. Langmuir **32**, 7356–7364 (2016). DOI 10.1021/acs.langmuir.6b01742, cit. on p. 91.

[84] R. Semenyshyn, M. Hentschel, C. Huck, J. Vogt, F. Weiher, H. Giessen, and F. Neubrech: *Resonant Plasmonic Nanoslits Enable in Vitro Observation of Single-Monolayer Collagen-Peptide Dynamics*. ACS Sensors **4**, 1966–1972 (2019). DOI 10.1021/acssensors.9b00377, cit. on p. 91.

[85] Y. Wang and Y. C. Chang: *Synthesis and conformational transition of surface-tethered polypeptide: Poly(L-lysine).* Macromolecules **36**, 6511–6518 (2003). DOI 10.1021/ma034093r, cit. on p. 90.

[86] Q. Xu and T. A. Keiderling: *Effect of sodium dodecyl sulfate on folding and thermal stability of acid-denatured cytochrome c: A spectroscopic approach*. Protein Science **13**, 2949–2959 (2004). DOI 10.1110/ps.04827604, cit. on p. 90.

[87] R. Gopal, J. S. Park, C. H. Seo, and Y. Park: *Applications of circular dichroism for structural analysis of gelatin and antimicrobial peptides*. International Journal of Molecular Sciences **13**, 3229–3244 (2012).
DOI 10.3390/ijms13033229, cit. on p. 90.

[88] *Progress in Nonlinear Nano-Optics*, 1st edition, Springer International Publishing (), 2015.
ISBN 978-3-319-12216-8, cit. on p. 93.

[89] R. A. Martinez, G. Plant, K. Guo, B. Janiszewski, M. J. Freeman, R. L. Maynard, M. N. Islam, F. L. Terry, O. Alvarez, F. Chenard, R. Bedford, R. Gibson, and A. I. Ifarraguerri: *Mid-infrared supercontinuum generation from* 1.6 *to* >11 µm *using concatenated step-index fluoride and chalcogenide fibers*. Optics Letters **43**, 296–299 (2018).
DOI 10.1364/ol.43.000296, cit. on p. 106.

[90] L. Maidment, P. G. Schunemann, and D. T. Reid: *Molecular fingerprint-region spectroscopy from* 5 *to* 12 µm *using an orientation-patterned gallium phosphide optical parametric oscillator*. Optics Letters **41**, 4261–4264 (2016).
DOI 10.1364/ol.41.004261, cit. on p. 107.

[91] N. Leindecker, A. Marandi, R. L. Byer, K. L. Vodopyanov, I. Hartl, M. Fermann, and P. G. Schunemann: *Octave-spanning ultrafast OPO with* 2.6 *to* 6.1 µm *instantaneous bandwidth pumped by femtosecond Tm-fiber laser*. Optics Express **20**, 7046–7053 (2012).
Cit. on p. 107.

[92] K. L. Vodopyanov, E. Sorokin, I. T. Sorokina, and P. G. Schunemann: *Mid-IR frequency comb source spanning* 4.4 *to* 5.4 µm *based on a subharmonic GaAs optical parametric oscillator*. Optics Letters **36**, 2275–2277 (2011).
DOI 10.1364/ol.36.002275, cit. on p. 107.

[93] K. L. Vodopyanov, O. Levi, P. S. Kuo, T. J. Pinguet, J. S. Harris, M. M. Fejer, B. Gerard, L. Becouara, and E. Lallier: *Optical parametric oscillation in quasi-phasematched GaAs*. Optics Letters **29**, 1912 –1914 (2004).
DOI 10.1364/ol.29.001912, cit. on p. 107.

[94] T. Skauli, K. L. Vodopyanov, T. J. Pinguet, A. Schober, O. Levi, L. A. Eyres, M. M. Fejer, J. S. Harris, B. Gerard, L. Becouarn, E. Lallier, and G. Arisholm: *Measurement of the nonlinear coefficient of orientation-patterned GaAs and demonstration of highly efficient second-harmonic generation.* Optics Letters **27**, 628–630 (2002).
DOI 10.1364/ol.27.000628, cit. on p. 107.

[95] L. Kühner, R. Semenyshyn, M. Hentschel, F. Neubrech, C. Tarín, and H. Giessen: *Vibrational Sensing Using Infrared Nanoantennas: Toward the Noninvasive Quantitation of Physiological Levels of Glucose and Fructose.* ACS Sensors **4**, 1973–1979 (2019).
DOI 10.1021/acssensors.9b00488, cit. on p. 133.

[96] N. Y. Kostyukova, A. A. Boyko, V. Badikov, D. Badikov, G. Shevyrdyaeva, V. Panyutin, G. M. Marchev, D. B. Kolker, and V. Petrov: *Widely tunable in the mid-IR $BaGa_4Se_7$ optical parametric oscillator pumped at* 1064 nm. Optics Letters **41**, 3667–3670 (2016).
DOI 10.1364/OL.41.003667, cit. on p. 133.

[97] V. Petrov: *New applications of chalcopyrite crystals in nonlinear optics.* Physica Status Solidi (C) Current Topics in Solid State Physics **14**, 1600161 (2017).
DOI 10.1002/pssc.201600161, cit. on p. 133.

PUBLICATIONS

JOURNAL PUBLICATIONS

Parts of this thesis have been published in peer-reviewed scientific journals as a corresponding author. A detailed list is given below.

P1 **F. Mörz**, T. Steinle, A. Steinmann, and H. Giessen,
"Multi-Watt femtosecond optical parametric master oscillator power amplifier at 43 MHz,"
Optics Express **23**, 23960-23967 (2015).

P2 **F. Mörz**, R. Semenyshyn, T. Steinle, F. Neubrech, U. Zschieschang, A. Steinmann, and H. Giessen,
"Nearly diffraction limited FTIR mapping using an ultrastable broadband femtosecond laser tunable from 1.33 to 8 µm,"
Optics Express **25**, 32355-32363 (2017).

P3 R. Semenyshyn, **F. Mörz**, T. Steinle, M. Ubl, M. Hentschel, F. Neubrech, and H. Giessen,
"Pushing down the limit: In-vitro detection of a polypeptide monolayer on a single infrared resonant Nanoantenna,"
ACS Photonics **6**, 2636-2642 (2019).

P4 **F. Mörz**, T. Steinle, H. Linnenbank, A. Steinmann, and H. Giessen,
"Alignment-free difference frequency light source tunable from 5 to 20 µm by mixing two independently tunable OPOs,"
Optics Express, **28**, 11883-11891 (2020).

Peer-reviewed publications that are not directly part of this thesis are listed below. * marks the corresponding author.

P5 S. Kedenburg*, T. Steinle, F. Mörz, A. Steinmann, and H. Giessen, "High-power midinfrared high repetition-rate supercontinuum source based on a chalcogenide step-index fiber," Optics Letters **40**, 2668-2671 (2015).

P6 S. Kedenburg*, T. Steinle, F. Mörz, A. Steinmann, D. Nguyen, D. Rhonehouse, J. Zong, A. Chavez-Pirson, and H. Giessen, "Solitonic supercontinuum of femtosecond mid-IR pulses in W-type index tellurite fibers and their applicaiton to absorption spectroscopy," APL Photonics **1**, 086101 (2016).

P7 S. Kedenburg*, C. Strutynski, B. Kibler, P. Froidevaux, F. Désévédavy, G. Gadret, J.-C. Jules, T. Steinle, F. Mörz, A. Steinmann, H. Giessen, and F. Smektala, ""High-repetition-rate midinfrared supercontinuum generation from 1.3 – 5.3 µm in robust step-index tellurite fibers," Journal of the Optical Society of America B, **34** 601-607 (2017).

P8 F. Sterl*, H. Linnenbank, T. Steinle, F. Mörz, N. Strohfeldt, and H. Giessen, "Nanoscale Hydrogenography on Single Magnesium Nanoparticles," Nano Letters **18**, 4293-4302 (2018).

P9 F. Robles*, H. Linnenbank, F. Mörz, P. Ledwig, T. Steinle, and H. Giessen, "Coherently broadened, high repetition rate laser for stimulated Raman scattering-spectroscopic optical coherence tomography

(SRS-OCT),"
Optics Letters **44**, 291-294 (2019).

P10 H. Linnenbank*, T. Steinle, F. Mörz, M. Flöss, H. Cui, A. Glidle, and H. Giessen,
"Robust and rapidly tunable light source for SRS/CARS microscopy with low-intensity noise,"
Advanced Photonics **1**, 055001 (2019).

P11 M. Nägele*, T. Steinle, F. Mörz, A. Steinmann, H. Linnenbank, and H. Giessen,
"Compact Harmonic Cavity Optical Parametric Oscillator for Optical Parametric Amplifier Seeding,"
Optics Express, **28**, 25000-25006 (2019).

CONFERENCE CONTRIBUTIONS

Conference presentations as presenting author:

C1 **F. Mörz**, T. Steinle, A. Steinmann, and H. Giessen,
"MID-IR generation at high repetitionrate using a green-pumped soliton-seeded optical parametric amplifier,"
Spring Meeting of the German Physical Society (DPG), Heidelberg, Germany (2015).

C2 **F. Mörz**, T. Steinle, A. Steinmann, and H. Giessen,
"Oscillator-pumped femtosecond laser source with nearly gap-free tuning range from 1.4 to 12 µm,"
Spring Meeting of the German Physical Society (DPG), Hannover, Germany (2016).

C3 **F. Mörz**, R. Semenyshyn, T. Steinle, F. Neubrech, A. Steinmann, and H. Giessen,
"Mid-IR laser-based FTIR mapping using a broadband fs laser source at 73 MHz repetition rate,"
Spring Meeting of the German Physical Society (DPG), Mainz, Germany (2017).

C4 **F. Mörz**, R. Semenyshyn, T. Steinle, F. Neubrech, A. Steinmann, and H. Giessen,
"Rapid mid-IR mapping using laser-based FTIR spectroscopy near the diffraction limit,"
Focus on Microscopy (FOM), Bordeaux, France (2017).

C5 **F. Mörz**, R. Semenyshyn, F. Neubrech, T. Steinle, A. Steinmann, and H. Giessen,
"Towards protein sensing using micro-FTIR spectroscopy by employing a parametric light source in the mid-IR,"
SPIE Photonics West, San Francisco, USA (2018).

Proceedings Volume 10522, Frontiers in Ultrafast Optics: Biomedical, Scientific, and Industrial Applications XVIII; 1052202, https://doi.org/10.1117/12.2287176

C6 **F. Mörz**, R. Semenyshyn, F. Neubrech, T. Steinle, A. Steinmann, and H. Giessen,
"Towards protein sensing using micro-FTIR spectroscopy by employing a parametric light source in the mid-IR,"
Spring Meeting of the German Physical Society (DPG), Erlangen, Germany (2018).

C7 **F. Mörz**, T. Steinle, H. Linnenbank, A. Steinmann, and H. Giessen,
"Robust difference frequency generation scheme tunable from 6 to 16 µm circumventing spatial beam offset from angular phase-matching,"
Spring Meeting of the German Physical Society (DPG), Munich, Germany (2019).

C8 **F. Mörz**, R. Semenyshyn, T. Steinle, M. Ubl, M. Hentschel, F. Neubrech, and H. Giessen,
"In-vitro detection of polypeptide conformations at attomolar concentration using an ultrafast laser and surface-enhanced infrared absorption spectroscopy on a single nanoantenna,"
SPIE Photonics West, San Francisco, USA (2020).
Proceedings Volume 11257, Plasmonics in Biology and Medicine XVII; 112570J, https://doi.org/10.1117/12.2545928

Selected oral conference presentations as co-author:

C9 S. Kedenburg*, T. Steinle, F. Mörz, A. Steinmann, D. Nguyen, D. Rhonehouse, J. Zong, A. Chavez-Pirson, and H. Giessen, "Solitonic supercontinuum of fs mid-IR pulses in W-type index tellurite fibers with two zero dispersion wavelengths," Nonlinear Photonics, Sidney, Australia (2016).
Conference Proceedings: Photonics and Fiber Technology 2016 (ACOFT, BGPP, NP), https://doi.org/10.1364/NP.2016.NW4A.2

C10 S. Kedenburg*, T. Steinle, **F. Mörz**, A. Steinmann, and H. Giessen,
"High-power mid-infrared high repetition-rate supercontinuum source based on a chalcogenide step-index fiber,"
Spring Meeting of the German Physical Society (DPG), Hannover, Germany (2016).

C11 H.Linnenbank*, F.Sterl, T.Steinle, F.Mörz, and H.Giessen,
"Near-Field optical microscopy of hydrogen absorption and desorption in magnesium-based plasmonic nanostructures,"
Focus on Microscopy (FOM), Bordeaux, France(2017).

C12 H. Linnenbank*, F. Sterl, T. Steinle, F. Mörz, and H. Giessen,
"Nanoscale hydrogenography of magnesium nanostructures with near-field optical microscopy,"
SPIE Photonics West, San Francisco, USA (2018).
Proceedings Volume 10539, Photonic Instrumentation Engineering V, 105390V, https://doi.org/10.1117/12.2289567

C13 H. Linnenbank*, T. Steinle, F. Mörz, M. Flöss, F. Robles, S. Kedenburg, and H. Giessen,
"Ultra-broad tunable low noise multi-color light source for

multi-photon imaging and spectroscopy," SPIE Photonics West, San Francisco, USA (2019).
Proceedings Volume 10882, Multiphoton Microscopy in the Biomedical Sciences XIX, 108820V, https://doi.org/10.1117/12.2510197

C14 F.Sterl*, H.Linnenbank, T.Steinle, F.Mörz, N.Strohfeldt, and H.Giessen,
"Nanoscale Hydrogenography of Individual Magnesium Nanoparticles,"
Materials Research Society (MRS) Fall Meeting, Boston, USA (2017).

C15 F.Sterl*, H.Linnenbank, T.Steinle, F.Mörz, N.Strohfeldt, and H.Giessen,
"Nanoscale Hydrogenography of Individual Magnesium Nanoparticles," Spring Meeting of the German Physical Society (DPG), Berlin, Germany (2018).

C16 M. Flöss*, T. Steinle, F. Mörz, H. Linnenbank, A. Steinmann, and H. Giessen,
"Build-up dynamics in an optical parametric oscillator with synchronized pump modulation,"
Spring Meeting of the German Physical Society (DPG), Munich, Germany (2019).

C17 M. Jäckle*, H. Linnenbank, T. Steinle, F. Mörz, A. Steinmann, and H. Giessen "Dispersion management in a fs Fiber-Feedback Optical Parametric Oscillator,"
Spring Meeting of the German Physical Society (DPG), Munich, Germany (2019).

C18 R. Semenyshyn*, F. Mörz, F. Neubrech, and H. Giessen,
"Surface-enhanced infrared absorption spectroscopy for in-vitro detection of the polypeptide monolayer conformation on a single gold nanoantenna,"
Spring Meeting of the German Physical Society (DPG), Regensburg, Germany (2019).

ACKNOWLEDGMENTS

After nearly eight years at the 4th Physics Institute at the University of Stuttgart, starting as a HiWi, then doing my Bachelor thesis, Master thesis and finally my PhD, I would like to thank all those who made that time something very special. I was able to learn a lot, was kept motivated and supported. I am very grateful for all these experiences and possibilities, as they should never be taken for granted.

Especially, I would like to thank:

- Prof. Dr. Harald Giessen for giving me the opportunity to work in his group and for supporting me for such a long time, which was something very special. I can not thank him enough for all the opportunities he provided. I would not be at this point without him.
- Prof. Dr. Peter Michler for agreeing to be my second adviser on such a short notice and for taking the time and effort to examine my thesis.
- Prof. Dr. Christian Holm for kindly agreeing to review my thesis and being head of the examination board.
- Dr. Christine von Rekowski for being great help with all administrative matters and being the place to go for everything else concerning university.
- Dr. Andy Steinmann for his great knowledge on nearly everything regarding lasers and nonlinear optics. For his great

support in the lab, office and administrative matters and many friendly conversations.

- Dr. Mario Hentschel for his great support in the last 7 years, always having time to help and his empathy and care.
- Dr. Joachim Krauth for the atmosphere in the last 4 years being my office colleague and for sharing a lot of sports and spare time activities.
- Dr. Florian Sterl for many helpful discussions, Matlab solutions, advice in the lab, and of course some MTB sessions.
- Dr. Tobias Steinle for his great advice and support within the last 7 years as an adviser, colleague, co-founder and sharing his passion for lasers.
- Dr. Heiko Linnenbank for his support as an adviser, colleague, co-founder, and many conversations on business trips, festivals, or concerts.
- Moritz Flöß, Dr. Rostyslav Semenyshyn, Dr. Stefan Kedenburg, and Josselin deFrance for the collaboration in the lab, IT help, bike riding, climbing and more.
- Mario Hentschel, Monika Ubl, Michael Kube, and Philipp Flad for all their help regarding sample preparation in the clean room and other technical support.
- All my colleagues and former colleagues at the 4th Physics Institute for keeping my studies and work interesting and motivating me. I would like to thank them for the fun time that I was able to enjoy at the institute and spare time activities.

Finally, I would like to thank my family for helping and supporting me during the last years, and especially the last three years. Without their support I would not have managed to write this thesis. Above all, I would like to thank my girlfriend Lena for her empathy, patience, and advise. She definitely needed to get through many tough discussions ;)

CURRICULUM VITÆ

NAME	Florian Mörz
BORN	1990/11/26 in Schwäbisch Hall
CITIZENSHIP	German
ADDRESS	Bietigheimer Straße 21, 70435 Stuttgart, Germany
E-MAIL	fmoerz26@googlemail.com

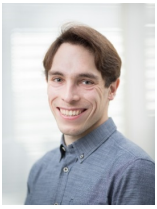

2001–2010	Hohenlohe Gymnasium Öhringen, Germany, Allgemeine Hochschulreife, Grade: 1.5
2010–2011	Civilian service at AWO (Arbeiterwohlfahrt) Öhringen, Germany
2010–2011	Guitar teaching at Volkshochschule Heilbronn, Germany
2011–2011	3-month R&D internship at *ebm-papst Mulfingen GmbH & Co. KG*, Germany
2011–2012	Training and further education in *Home&Studio Recording* at SAE Institute, Stuttgart, Germany
2011–2014	Studies of physics: University of Stuttgart, Germany, *Degree: B. Sc. Phys., Grade:* 2.3
2012	Bachelor's thesis: *Mid-IR Generation at high repetition rates by a green-pumped soliton OPA*, University of Stuttgart, Germany, Grade: 1.0 Advisor: Prof. Dr. Harald Giessen

2014–2017	Studies of physics: University of Stuttgart, Germany, *Degree: M. Sc., Grade:* 1.1 *with honors*
2017	Master's thesis: *Laser sources for cw SRS* , University of Stuttgart, Germany, Grade: 1.0, Advisor: Prof. Dr. Harald Giessen
2017–2020	Ph.D. thesis: *'Ultrafast laser sources – Tunable, ultrafast laser sources for near- and mid-ir spectroscopy'*, University of Stuttgart, Germany, Advisor: Prof. Dr. Harald Giessen

DECLARATION

I hereby certify that this dissertation is entirely my own work except where otherwise indicated. Passages and ideas from other sources have been clearly indicated.

Stuttgart,

Florian Mörz